FUNDAMENTAL STUDY OF A SUBMERGED AND NON-SUBMERGED THREE DIMENSIONAL JET IMPINGING UPON A NORMAL PLANE

Final Report to National Science Foundation
Under Grant NSF G-9434
PART I - Ph.D. Dissertation
"Axisymmetric Boundary-Layer of a Jet
Impinging on a Smooth Plate,"
by Yeong-ging Tsuei.
PART II - APPENDIX A
"An Analysis of the Momentum Equation
for the Turbulent Wall Jet,"
by Junn-Ling Chao and Lionel V. Baldwin.

Colorado State University
Engineering Research Center
Fort Collins, Colorado

June 1963

CER63GLS1

ABSTRACT OF DISSERTATION

AXISYMMETRIC BOUNDARY-LAYER OF A JET

IMPINGING ON A SMOOTH PLATE

The flow characteristics of a radial wall jet formed by the normal impingement of an air jet on a smooth flat plate have been studied. The mean velocity and the turbulence statistics for different orifice velocities and diameters were measured with a pitot tube and a hot-wire anemometer. Most of the measurements were made at ten vertical stations spaced at 6 in. intervals along a radius. The first station was twelve inches from the stagnation point.

A particular form for the turbulent shear stress is proposed. Using the incompressible boundary-layer approximations and a similarity assumption, the momentum and continuity equations were used to derive expressions in the form of an exponential decay for the peak radial velocity and a linear growth for the boundary-layer thickness with respect to the radial distance from the center. The measured profiles of velocity and turbulent intensities were found to be approximately similar; thus, approximate universal functions were obtained by expressing $\frac{u}{u_m}$, $\frac{\sqrt{\overline{u'^2}}}{u_m}$, $\frac{\sqrt{\overline{v'^2}}}{u_m}$ and $\frac{\sqrt{\overline{w'^2}}}{u_m}$ (the relative velocity and turbulent intensities respectively) in terms of a non-dimensional vertical coordinate $\zeta = \frac{z}{\delta_{0.5}}$. The characteristic length $\delta_{0.5}$ was chosen as the height where $\frac{u}{u_m} = 0.5$.

The mean velocity profile of the inner boundary-layer does not follow the pipe wall law and only a limited region can be approximated by the logrithmic form. This is attributed to the effects of the highly turbulent flow within the outer layer of the wall jet which produces disturbances penetrating deeply into the inner boundary-layer. Consequently, a higher wall shear stress results in this wall jet flow than in ordinary two-dimensional boundary-layer flow. The wall shear stress was found to be approximately proportional to the inverse square of the radial distance.

Yeong-ging Tsuei
Civil Engineering Department
Colorado State University
August, 1962

ACKNOWLEDGEMENT

The writer wishes to express his deep appreciation to his Major Professor, Prof. J. E. Cermak, who gave guidance and advice to the writer in every phase of the work.

Assistance and advice tendered by Prof. M. E. Bender, Mr. G. L. Smith, and members of the Committee on Graduate Work are gratefully acknowledged.

The writer wishes to thank Dr. L. V. Baldwin for his valuable suggestions and criticism, Asst. Prof. E. J. Plate for his design of the equipment, Assoc. Prof. A. Budak and Mr. R. J. Morgan for their help in the design of the shear-meter, and Mr. J. L. Chao for his general assistance. The writer also gratefully acknowledges the unlimited help given by Dr. L. V. Baldwin and Dr. R. C. Malhotra in the preparation of the final manuscript. The advice and criticism of co-workers in the Aeromechanics Laboratory as well as the technical assistance of many others is greatly appreciated.

The investigation presented in this dissertation has been sponsored by the National Science Foundation.

TABLE OF CONTENTS

TABLE OF CONTENTS.---(Cont'd.)

LIST OF FIGURES

LIST OF FIGURES.--(Cont'd.)

LIST OF FIGURES.--(Cont'd.)

Coordinate System and Notation

A right handed cylindrical coordinate system is used. The origin is located at the stagnation point on the plate center with positive z-axis vertically upward as shown in Fig. 1, r is the radial coordinate and ϕ is the circumferential coordinate. Thus, (u, v, w) are the velocity components in the radial, circumferential and vertical directions respectively. Notice that for the associated free circular jet, the velocity parallel to its axis is $-w_j$.

The following notations are used:

Notation	Definition	Dimension*
A	Proportionality constant for the decay of the peak radial velocity u_m	--
B	Proportionality constant for the growth of the boundary-layer thickness	--
$\mathcal{D}$	Shear proportionality constant	--
D	Diameter of jet orifice	L
H	Height of jet orifice above the plate	L
k	Constant for the evaluation of turbulent shear stress	--
P	Instantaneous pressure	FL^{-2}
p	Mean static pressure	FL^{-2}
p_w	Mean pressure at wall	FL^{-2}
r, λ	Radial coordinate	L

* F - force, L - length, T - time.

Notation	Definition	Dimension
Re	Reynolds number $\frac{w_{j_o} D}{\nu}$	--
$\mathcal{U}$	Non-dimensional velocity parameter	--
u_m	Peak radial velocity in the wall jet	LT^{-1}
u_*	Shear velocity	LT^{-1}
U, V, W	Instantaneous velocity components in the radial, circumferential and vertical directions respectively	LT^{-1}
u, v, w	Time mean velocity components in the radial, circumferential and vertical directions respectively	LT^{-1}
u', v', w'	Fluctuating velocity components in the radial, circumferential and vertical directions respectively	LT^{-1}
$\sqrt{\overline{u'^2}}, \sqrt{\overline{v'^2}}, \sqrt{\overline{w'^2}}$	RMS turbulent velocity intensities in the radial, circumferential and vertical directions respectively	LT^{-1}
$\overline{u'w'}$	Correlation of turbulent velocities	L^2T^{-2}
$-w_{j_o}$	Downward mean velocity at the jet orifice	LT^{-1}
$-w_j$	Local downward mean velocity for the free circular jet	LT^{-1}
$-w_{jm}$	Downward mean velocity at the axis of the free circular jet	LT^{-1}
z , ζ	Vertical coordinate	L
δ	Boundary-layer thickness	L
$\delta_{0.5}$	Boundary-layer thickness at half peak radial velocity 1/2 u_m	L
ε	Kinematic eddy viscosity	L^2T^{-1}
μ	Dynamic viscosity	$FL^{-2}T$
ν	Kinematic viscosity	L^2T^{-1}
ρ	Mass density	$FL^{-4}T^2$

Notation	Definition	Dimension
ϕ	Circumferential coordinate	—
τ_o	Wall shear stress	FL^{-2}
τ_t	Turbulent shear stress	FL^{-2}
ζ	Non-dimensional height $\frac{z}{\delta_{0.5}}$	—

All other notations and symbols which are not used frequently in the dissertation will be defined wherever they first appear.

Chapter I

INTRODUCTION

The flow formed by the impingement of a jet on a surface is of considerable interest to fluid dynamists for at least two reasons. First, there are many practical problems which require a knowledge of such flow fields for an adequate solution. Some of these problems are erosion by falling jets of water, jet blasts, paint sprays and the operation of vertical-take-off aircraft and helicopters on unprepared sites. Second, the study of wall jets serves as a basic study on the effects on the flow of the interaction between the free boundary and the solid boundary.

The characteristics of the jet depends on many factors: the type of fluid mixing; the temperature in the surrounding fluid and the jet itself; the magnitude of the jet velocity (compressibility effect); the flow condition of the surrounding fluid; the angle of impingement of the jet; the roughness and the geometric shape of the surface. In order to attack such a complicated flow problem, it is advisable to study the simplest case such as that of a low speed, incompressible jet with uniform temperature impinging normally on a smooth flat plate. Such flows have been theoretically studied by Glauert (7), Poreh, et al. (16), and Vidal (23). Experimental work concerning plane wall jets have been carried out by Bradshaw, et al. (4), Eskinazi, et al. (6), Schwarz, et al. (19),

Myers, et al. (14), and Sigalla (20), (21). Bakke (2), Bradshaw, et al. (3), and Poreh, et al. (16) have experimentally studied the radial wall jet. Little work has been attempted to study the turbulent characteristics and the wall-friction distribution in a radial wall jet. The present work is a study of an axisymmetrical jet impinging normally on a flat plate. The mean velocity, the turbulent intensities and the turbulent shear stress were measured by means of a hot-wire anemometer in order to study the decay of the mean velocity, the growth of the boundary-layer thickness and the turbulent structure. A sensitive floating-element type shear-meter was designed. Data on skin friction obtained by direct shear measurements may be used to predict the distribution of the skin friction in similar wall jets.

Chapter II

REVIEW OF LITERATURE

The review of previous work which is pertinent to this study is presented in this chapter. For a turbulent wall jet the review is developed in two sections: (1) analytical approaches; (2) experimental studies.

Analytical Approaches

Theoretically the wall jet was first studied, using a similarity-type solution, by Glauert (7). Using the concept of an eddy viscosity ε which is very large compared with ν, the appropriate boundary-layer equation becomes

$$u \frac{\partial u}{\partial x} + w \frac{\partial u}{\partial y} = \frac{\partial}{\partial y}\left(\varepsilon \frac{\partial u}{\partial y}\right), \qquad (2\text{-}1)$$

where u and w denote the components of the mean velocity. The boundary conditions and the continuity equation for such flows are:

$$u = w = 0 \quad \text{at} \quad z = 0, \text{ and } u = 0 \text{ as } z \to \infty, \qquad (2\text{-}2)$$

and

$$\frac{\partial (x u)}{\partial x} + \frac{\partial (x w)}{\partial y} = 0 \quad . \qquad (2\text{-}3)$$

Glauert divides the boundary-layer into two parts, the inner and the outer. In order to determine the form of ε for the inner part of the boundary layer, he makes use of the empirical formula, due to Blasius, for turbulent pipe flow. Since τ_o is governed by the conditions near the wall, he replaces the maximum velocity by u and the radius of pipe by z, and assumes the

Blasius solution to hold near the wall in any turbulent boundary layer flow, outside the viscous layer. Then, Blasius' empirical formula becomes

$$\tau_o = 0.0225 \rho u^2 \left(\frac{\nu}{u y}\right)^{1/4} . \qquad (2\text{-}4)$$

Equation (2-4) implies that, near the wall, $u \propto y^{1/7}$.

The shear stress $\tau_x = \varepsilon \frac{\partial u}{\partial y}$ has a finite non-zero value at the wall and hence, for a fixed r ,

$$\varepsilon \propto y^{6/7} \propto u^6 .$$

Thus $\varepsilon = f(x)\, u^6$.

Glauert considers a similarity solution by assuming $u \propto x^a$ and $\delta \propto x^b$. This requires that $\tau_o \propto u^{7/4} \delta^{-1/4}$, and hence $\varepsilon \propto u^{3/4} \delta^{3/4} \propto x^{3(a+b)/4}$. For the outer boundary, following Prandtl's hypothesis ε = constant over the cross section, and by matching the two parts at the peak velocity, he obtains a solution of Eq. (2-1). This solution contains one arbitrary constant which must be determined by experiments. The solution indicates that no exact similarity is possible if one assumes independent inner and outer boundary-layers. Experimental mean velocity profiles indicate good agreement with Glauert's analysis, except in regions very close to the wall and far-out at the boundary of the circular free jet. From this definition of an eddy viscosity, the turbulent shear stress at the peak velocity, where the gradient is zero, must also be zero. This prediction does not agree with experimental results as will be explained in Chapter V. Further, Glauert's prediction of wall shear stress is lower than the experimental results of Bradshaw, et al. (3), Myers, et al. (14) and Sigalla (20), (21).

In their study of a circular submerged water jet impinging normally on a smooth boundary, Poreh, et al. (16), utilize the Reynolds equations

$$V_r \frac{\partial V_r}{\partial r} + V_z \frac{\partial V_r}{\partial z} = -\frac{1}{\rho}\frac{\partial P}{\partial r} + \frac{1}{\rho r}\left[\frac{\partial}{\partial r}(r T_{rr}) + \frac{\partial}{\partial z}(r T_{zr}) - T_{\phi\phi}\right],$$

and $$V_r \frac{\partial V_z}{\partial r} + V_z \frac{\partial V_z}{\partial z} = -\frac{1}{\rho}\frac{\partial P}{\partial z} + \frac{1}{\rho r}\left[\frac{\partial}{\partial r}(r T_{rz}) + \frac{\partial}{\partial z}(r T_{zz})\right],$$

and the continuity equation for the mean and the fluctuating component of the velocity

$$\nabla \cdot \vec{V} = 0 \qquad \text{and} \qquad \nabla \cdot \vec{v'} = 0 ,$$

for their analysis. Here V_i is the component of the mean velocity in the i direction, v_i' is the component of the fluctuating velocity in the i direction, and T_{ij} is the ij-component of the stress tensor including the Reynolds stress component $-\rho\overline{v_i' v_j'}$ and the ij-component of the stress due to viscosity. They integrate the equation by assuming that the velocity profile is the same as that for a free radial jet except near the wall where the velocity is retarded by the presence of the boundary as shown in Fig. 2. Using the condition for a free circular jet that $\int_0^\beta V_R^2 r\, dz =$ constant and further assuming that P = constant with $V_r \to 0$ at $z \to \beta$, Poreh, et al., obtain the following expression for evaluating the wall shear stress:

$$\frac{\tau_0}{\rho V_{RB}^2} = r \frac{\partial}{\partial r}\frac{1}{r}\int_0^\delta \frac{V_R^2 - V_r^2}{V_{RB}^2} dz + C_1 + C_2 + C_3 + C_4 . \qquad (2\text{-}5)$$

In Eq. (2-5)

$$C_1 = -\frac{1}{V_{RB}^2}\int_0^\beta \left[\frac{\partial}{\partial r}(\overline{u'u'} - \overline{w'w'}) + \frac{1}{r}(\overline{u'u'} - \overline{v'v'})\right] dz$$

is due to the anisotropy of the turbulent normal stress,

$$C_2 = \frac{2\nu}{V_{RB}^2}\int_0^\beta \left[\frac{1}{r}\frac{\partial}{\partial r}\left(r\frac{\partial V_r}{\partial r}\right) - \frac{\partial}{\partial r}\frac{\partial V_z}{\partial z} - \frac{V_r}{r}\right] dz$$

is due to the effect of viscosity,

$$C_3 = \frac{1}{V_{RB}^2}\int_0^\beta \int_0^z \frac{\partial}{\partial r}\frac{1}{r}\frac{\partial}{\partial r} r\left[\nu\left(\frac{\partial V_r}{\partial z} + \frac{\partial V_z}{\partial z}\right) - r\overline{u'w'}\right] dz\, dz$$

is due to the second derivatives of shear stresses, and

$$C_4 = \frac{1}{V_{RB}^2}\int_0^\beta \int_0^z \frac{\partial}{\partial r}\left[V_r\frac{\partial V_z}{\partial r} - \frac{V_z}{r}\frac{\partial}{\partial r}(rV_r)\right] dz\, dz$$

is due to the terms usually neglected by the boundary-layer approximation.

If we neglect the contribution of turbulence as a first approximation, Eq. (2-5) reduces to

$$\frac{\tau_0}{\rho V_{RB}^2} \approx r\frac{\partial}{\partial r}\frac{1}{r}\int_0^\delta \frac{V_R^2 - V_r^2}{V_{RB}^2} dz \quad . \tag{2-6}$$

The above expression shows that turbulent quantities are required for a more accurate evaluation of the wall shear stress.

For engineering purposes, Vidal (23) studies the condition for particle entrainment in the region close to the stagnation point of an impinging jet. He estimates that in the central region the transition from laminar to turbulent flow occurs at

$$\frac{r}{D} = \frac{7.11\times 10^3}{\sqrt{Re_D}} \quad ,$$

where

$$Re_D = \frac{U_j D}{\nu} \quad .$$

Therefore, for most practical configurations the stagnation zone is laminar up to $\frac{r}{D} \approx 1$, where the maximum radial velocity occurs. Based on the laminar condition, Vidal establishes criteria for initially entraining ground particles from downwash impingement in terms of the jet diameter, the jet velocity, the particle size and the boundary-layer thickness in the stagnation region $\frac{r}{D} < 1$. He also demonstrates the influence of the configuration scale and shows that for particle sizes, such that $\frac{d}{\delta} < 0.6$, where d is the diameter of the particle, lift will predominate. For larger particle sizes, drag should produce the entrainment. Entrainment occurs only in a finite annular region under an impinging jet. The size of this annulus and the size of the particles entrained are determined by the initial velocity in the jet and the jet diameter.

The potential flow for a jet normally impinging on a plate is summarized by Schlichting (17) as follows:

$$u = cr,$$

$$w = -2cz,$$

and $$p_0 - p = \frac{\rho}{2}(u^2 + w^2) = \frac{\rho}{2} c^2 (r^2 + 4z^2).$$

On the boundary for $z = 0$, we have

$$p_0 - p = \frac{\rho}{2} c^2 r^2,$$

where c is a constant and p_0 is the stagnation pressure at the center.

One sees that very close to the stagnation point, the pressure distribution is parabolic. Since Vidal's analysis shows that the flow is laminar near the stagnation point, one may use

the exact solution of the laminar viscous stagnation flow by K. Hiemenz to evaluate the wall shear stress in this region. From Schlichting (18), one obtains

$$\tau_o = \frac{\nu}{\rho}\left(\frac{\partial u}{\partial z} + \frac{\partial w}{\partial r}\right)\Big|_{z=0} = 1.312\sqrt{\rho^2 \nu c^3}\, r \ .$$

One sees that the wall shear stress is predicted as being linearly proportional to r in the stagnation region. This theoretical result has been verified experimentally by Bradshaw, et al. (3); although these authors did not point out that the region is laminar and thus made no comparison with the theoretical results for laminar viscous stagnation flow.

Experimental Studies of Radial Wall Jets

Although there are several experimental studies on the plane wall jet, such as Bradshaw, et al. (4), Eskinazi, et al. (6), Myers, et al. (14), Schwarz, et al. (19), Sigalla (20), the only experimental studies of a radial wall jet known to the writer are by Bakke (2), Bradshaw, et al. (3) and Poreh, et al. (16).

Bakke studied a radial wall jet of ambient air eminating from a flanged pipe placed at right angles to a smooth bakelite plate with the exit 15.0 mm above the plate. The mean velocity distributions were measured at nine stations at distances of 143 to 303 mm from the origin; the peak radial velocity, u_m, varied from 2.60 m/sec to 6.10 m/sec. Bakke reported that the non-dimensional mean velocity plots were similar with respect to the parameters $\frac{u}{u_m}$ and $\frac{z}{\delta_{0.5}}$, within the accuracy of the measurements. The data points agree fairly well with Glauert's theoretical prediction except

very close to the wall where the measured values of $\frac{u}{u_m}$ were too small, and at the outer boundary where Grauert's prediction are too large. The measured simple power relationship between the characteristic thickness $\delta_{0.5}$ and the distance r from the stagnation point gives $b = 0.94 < 1$ which is different from Glauert's prediction of $b \geq 1$.

Bradshaw, et al. (3) studied a circular turbulent jet, having an inside diameter of 1" and a velocity of 350 ft/sec, impinging normally on a 50" square flat surface located 18 in. from the jet nozzle in ambient air. The speed and the radius of the jet just before impingement was 135 ft/sec. and 2.5 in. respectively. They measured the magnitude and direction of the mean velocity, the static pressure and the skin friction by means of a flat pitot tube. Bradshaw's experimental results are summarized as follows:

1. The structure of the radial wall jet changes quickly from the deflected flow created by the impingement of the free jet; the region of deflection is mainly restricted to the stagnation zone. This rapid recovery is followed by a flow with characteristics similar to the case of jet impingement just as was the case for a jet emerging from a central source.

2. In the stagnation region, the static pressure increases. The contours of the pressure parameter $\frac{p - p_a}{p_o - p_a}$ are roughly in the shape of a hemisphere, where p, p_a and p_o are the static, atmospheric and stagnation pressures respectively. The contour of $\frac{p - p_a}{p_o - p_a} = 0.018$ is roughly of 3" radius. This is slightly

larger than that of the free jet just before impingement. The virtual origin of a best-straight-line fit to $\frac{1}{u_m}$ is at about $r = 1.7$ in. and that of a best-straight-line fit to the values of $\delta_{0.5}$ is at $r = 0.6$ in.

3. The maximum wall shear stress occurs at $r = 2.5$ in. which is roughly the radius of the free jet just impinging the plate and more particularly of the static pressure field, indicating that, as might be expected, the peak radial velocity reaches a maximum under the influence of the pressure gradient and then falls off because of radial dispersion and viscous dissipation. The magnitude of the maximum skin friction is about 0.006 of the maximum dynamic pressure of the jet at the test Reynolds number. The skin friction coefficient based on local peak radial velocity u_m falls as:

r in.	C_f
3.25	0.0089
8.45	0.0082
12.0	0.0072

although the Reynolds number based on peak velocity and peak height is approximately constant at a value of 4000.

4. All these values of skin friction are about 25 percent higher than those predicted by Glauert's analysis.

5. According to the skin friction distribution, very little erosion should occur at the jet axis, and the rate of erosion should decrease very rapidly after reaching a maximum at about one jet radius from the center.

Chapter III

ANALYTICAL CONSIDERATION

In this chapter the basic equations governing the flow of an imcompressible, viscous fluid are expressed in a cylindrical coordinate system. The equations are written for a turbulent flow by expressing each of the dependent flow characteristics as a time mean plus a fluctuation and then taking a time mean of the resulting equations. The basic equations are expressed in dimensionless form under the similarity assumption. To assist in applying the equations, the order of magnitude of terms appearing in the equations is estimated. Also, by physical reasoning, a particular form for the turbulent shear stress is proposed.

Basic Equations

Throughout the entirety of the analytical discussion, the flow field is considered to be incompressible and at constant temperature. Under these restrictions, the basic equations governing the flow field are the equations expressing the conservation of mass and the conservation of momentum. The mass conservation equation is

$$\frac{\partial U}{\partial r} + \frac{U}{r} + \frac{1}{r}\frac{\partial V}{\partial \phi} + \frac{\partial W}{\partial z} = 0. \qquad (3\text{-}1)$$

In absence of body forces, the momentum equations in the radial, the circumferential and the vertical directions (9) are

$$\rho\left(\frac{DU}{Dt}-\frac{V^2}{r}\right)=-\frac{\partial P}{\partial r}+\mu\left(\nabla^2 U-\frac{U}{r^2}-\frac{2}{r^2}\frac{\partial V}{\partial \phi}\right), \qquad (3\text{-}2)$$

$$\rho\left(\frac{DV}{Dt}+\frac{UV}{r}\right)=-\frac{1}{r}\frac{\partial P}{\partial \phi}+\mu\left(\nabla^2 V-\frac{V}{r^2}+\frac{2}{r^2}\frac{\partial U}{\partial \phi}\right), \qquad (3\text{-}3)$$

and $$\rho\frac{DW}{Dt}=-\frac{\partial P}{\partial z}+\mu\nabla^2 W, \qquad (3\text{-}4)$$

where $$\frac{D}{Dt}=\frac{\partial}{\partial t}+U\frac{\partial}{\partial r}+\frac{V}{r}\frac{\partial}{\partial \phi}+W\frac{\partial}{\partial z},$$

$$\nabla^2=\frac{\partial^2}{\partial r^2}+\frac{1}{r}\frac{\partial}{\partial r}+\frac{1}{r^2}\frac{\partial^2}{\partial \phi^2}+\frac{\partial^2}{\partial z^2},$$

and all the instantaneous dependent variables can be expressed as the sum of a time mean and a fluctuation about the mean for a steady flow system, that is,

$$P = p - p',$$

$$U = u - u',$$

$$V = v - v',$$

$$W = w - w'.$$

These basic equations can be reduced to forms applicable to this study, of the turbulent boundary-layer, by taking a temporal average of the equations. The averaging process will be accomplished by using Reynolds' rules of averaging (18) as follows:

$$\overline{M} = m \quad \text{and} \quad \overline{N} = n,$$

$$\overline{M + N} = m + n,$$

$$\overline{MN} = mn,$$

$$\overline{cM} = cm,$$

$$\frac{\overline{\partial M}}{\partial x_i} = \frac{\partial m}{\partial x_i} \quad ,$$

where M and N are functions of time and c is a constant.

In the study of the turbulent boundary-layer of a radial wall jet, one has, due to axisymmetry and quasi-steady flow,

$$\frac{\partial \bar{}}{\partial t} = 0, \quad \frac{\partial \bar{}}{\partial \phi} = 0, \quad v = 0 \ , \quad v' \neq 0$$

and $$\overline{u'v'} = \overline{v'w'} = 0.$$

Upon averaging the mass conservation equation and using the above condition, Eq. (3-1) becomes

$$\frac{\partial u}{\partial r} + \frac{u}{r} + \frac{\partial w}{\partial z} = 0 \tag{3-5}$$

for the temporal velocity, and from Eqs. (3-1) and (3-5)

$$\frac{\partial u'}{\partial r} + \frac{u'}{r} + \frac{1}{r}\frac{\partial v'}{\partial \phi} + \frac{\partial w'}{\partial z} = 0 \tag{3-6}$$

for the fluctuating velocity about the mean.

The circumferential momentum equation (3-3) becomes identically zero after introducing Eq. (3-6) and the axi-symmetric property into it and averaging the resulting equation. Under the same operations Eqs. (3-2) and (3-4) become:

$$u\frac{\partial u}{\partial r} + w\frac{\partial u}{\partial z} + \frac{\partial \overline{u'^2}}{\partial r} + \frac{1}{r}\left(\overline{u'^2} - \overline{v'^2}\right) + \frac{\partial \overline{u'w'}}{\partial z}$$

$$= -\frac{1}{\rho}\frac{\partial p}{\partial r} + \nu\left\{\frac{\partial^2 u}{\partial r^2} + \frac{1}{r}\frac{\partial u}{\partial r} - \frac{u}{r} + \frac{\partial^2 u}{\partial z^2}\right\} \quad , \tag{3-7}$$

and $$u\frac{\partial w}{\partial r} + w\frac{\partial w}{\partial z} + \frac{\partial \overline{u'w'}}{\partial r} + \frac{\overline{u'w'}}{r} + \frac{\partial \overline{w'^2}}{\partial z}$$

$$= -\frac{1}{\rho}\frac{\partial p}{\partial z} + \nu\left\{\frac{\partial^2 w}{\partial r^2} + \frac{1}{r}\frac{\partial w}{\partial r} + \frac{\partial^2 w}{\partial z^2}\right\} \quad , \qquad (3\text{-}8)$$

with the following boundary conditions

$$u = w = u' = v' = w' = 0, \quad p = p_w \quad \text{at} \quad z = 0,$$

and $$u = 0 \quad \text{at} \quad z = \infty$$

where p_w is the static pressure at the wall.

Boundary Layer Approximation

Introducing a reference velocity $\tilde{U}$ and a reference length L, Eqs. (3-7) and (3-8) become

$$\underset{1}{\frac{u}{\tilde{U}}\frac{\partial \frac{u}{\tilde{U}}}{\partial \frac{r}{L}}} + \underset{1}{\frac{w}{\tilde{U}}\frac{\partial \frac{u}{\tilde{U}}}{\partial \frac{z}{L}}} + \underset{\delta}{\frac{\partial \frac{\overline{u'^2}}{\tilde{U}^2}}{\partial \frac{r}{L}}} + \underset{\delta}{\frac{1}{\frac{r}{L}}\left(\frac{\overline{u'^2}}{\tilde{U}^2} - \frac{\overline{v'^2}}{\tilde{U}^2}\right)} + \underset{1}{\frac{\partial \frac{\overline{u'w'}}{\tilde{U}^2}}{\partial \frac{z}{L}}}$$

$$= \underset{\delta^2}{-\frac{\partial \frac{p}{\rho \tilde{U}^2}}{\partial \frac{r}{L}}} + \frac{\nu}{\tilde{U}L}\left\{\underset{\delta^2}{\frac{\partial^2 \frac{u}{\tilde{U}}}{\partial (\frac{r}{L})^2}} + \underset{\delta^2}{\frac{1}{\frac{r}{L}}\frac{\partial \frac{u}{\tilde{U}}}{\partial \frac{r}{L}}} - \underset{\delta^2}{\frac{\frac{u}{\tilde{U}}}{(\frac{r}{L})^2}} + \underset{1}{\frac{\partial^2 \frac{u}{\tilde{U}}}{\partial (\frac{z}{L})^2}}\right\} \qquad (3\text{-}9)$$

and

$$\underset{\delta}{\frac{u}{\tilde{U}}\frac{\partial \frac{w}{\tilde{U}}}{\partial \frac{r}{L}}} + \underset{\delta}{\frac{w}{\tilde{U}}\frac{\partial \frac{w}{\tilde{U}}}{\partial \frac{z}{L}}} + \underset{\delta}{\frac{\partial \frac{\overline{u'w'}}{\tilde{U}^2}}{\partial \frac{r}{L}}} + \underset{\delta}{\frac{\frac{\overline{u'w'}}{\tilde{U}^2}}{\frac{r}{L}}} + \underset{1}{\frac{\partial \frac{\overline{w'^2}}{\tilde{U}^2}}{\partial \frac{z}{L}}}$$

$$= \underset{\delta^3}{-\frac{\partial \frac{p}{\rho \tilde{U}^2}}{\partial \frac{z}{L}}} + \frac{\nu}{\tilde{U}L}\left\{\underset{\delta^3}{\frac{\partial^2 \frac{w}{\tilde{U}}}{\partial (\frac{r}{L})^2}} + \underset{\delta^3}{\frac{1}{\frac{r}{L}}\frac{\partial \frac{w}{\tilde{U}}}{\partial \frac{r}{L}}} + \underset{\delta}{\frac{\partial^2 \frac{w}{\tilde{U}}}{\partial (\frac{z}{L})^2}}\right\} . \qquad (3\text{-}10)$$

The present experiments indicate a slow rate of growth of the boundary-layer in the vertical direction and high turbulent fluctuations. Based on these experimental findings the quantities

appearing in Eqs. (3-9) and (3-10) are taken to have the following order of magnitude:

$$\frac{u}{\tilde{U}} ; \frac{r}{L} = O(1) \quad ,$$

$$\frac{z}{L} ; \frac{\overline{u'^2}}{\tilde{U}^2} ; \frac{\overline{v'^2}}{\tilde{U}^2} ; \frac{\overline{w'^2}}{\tilde{U}^2} ; \frac{\overline{u'w'}}{\tilde{U}^2} ; \frac{w}{\tilde{U}} = O(\delta) \quad .$$

Thus $\frac{\partial}{\partial \frac{r}{L}} = O(1)$ and $\frac{\partial}{\partial \frac{z}{L}} = O(\delta)$, and each term in Eqs. (3-9) and (3-10) will be of the order of magnitude indicated below the terms.

In the ordinary laminar boundary-layer flow, the boundary-layer thickness δ is proportional to the square root of the kinematic viscosity, i.e., $\delta \propto \sqrt{\nu}$.
The turbulent boundary-layer thickness for the same viscosity is smaller than that for laminar flow; thus the reciprocal of the Reynolds number $\frac{\tilde{U}L}{\nu}$ is at least of the order of δ^2.

Hence by neglecting all terms except first order ones Eqs. (3-9) and (3-10) become

$$u \frac{\partial u}{\partial r} + w \frac{\partial u}{\partial z} + \frac{\partial \overline{u'w'}}{\partial z}$$

$$= -\frac{1}{\rho} \frac{\partial p}{\partial r} + \nu \frac{\partial^2 u}{\partial z^2} \quad , \qquad (3\text{-}11)$$

and $$\frac{\partial \overline{w'^2}}{\partial z} = -\frac{1}{\rho} \frac{\partial p}{\partial z} \quad . \qquad (3\text{-}12)$$

On assuming that the pressure gradient in the radial direction is neglegible the radial and vertical components of the momentum equations (3-11) and (3-12) become uncoupled. Thus, we have the following momentum equation:

$$u\frac{\partial u}{\partial x} + w\frac{\partial u}{\partial z} + \frac{\partial \overline{u'w'}}{\partial z} = \nu\frac{\partial^2 u}{\partial z^2} \quad . \tag{3-13}$$

The relevant mass conservation is Eq. (3-5).

Discussion of Turbulent Shear Stress

In order to attack these equations which contain more unknowns than there are equations, certain assumptions concerning the form of the turbulent shear stress have to be made. In analogy with the coefficient of viscosity in Stokes' law for laminar flow

$$\tau_l = \mu\frac{\partial u}{\partial z} \quad ,$$

T. V. Boussinesq introduced a mixing coefficient, $\mathcal{A}$ for the turbulent shear stress by putting

$$\tau_t = \mathcal{A}\frac{\partial u}{\partial z} = \rho\varepsilon\frac{\partial u}{\partial z} \quad .$$

Here u denotes the time-mean of velocity. The turbulent mixing coefficient $\mathcal{A}$ corresponds to the viscosity μ in laminar flow, and $\varepsilon = \frac{\mathcal{A}}{\rho}$ corresponding to $\nu = \frac{\mu}{\rho}$ is called the apparent kinematic viscosity or eddy viscosity.

Later L. Prandtl developed his hypothesis on the mixing length l for two-dimensional parallel flow. By making the assumption u' $\propto$ w', and u' $\propto l\frac{\partial u}{\partial z}$, as shown in Fig. 3(a), he obtained

$$\tau_t = -\rho\overline{u'w'} = \rho\varepsilon\frac{\partial u}{\partial z} = \text{const. } \rho l^2\left|\frac{\partial u}{\partial z}\right|\frac{\partial u}{\partial z} \quad .$$

Thus he found the expression

$$\varepsilon = \text{const. } l^2\left|\frac{\partial u}{\partial z}\right| \quad .$$

This concept of eddy viscosity shows that the eddy viscosity depends on the flow field; also τ_t must be zero if the velocity gradient $\frac{\partial u}{\partial y}$ is zero, thus implying zero turbulent shear stress. However, Prandtl's hypothesis does not agree with experiments in which asymmetric velocity profiles have been measured. In his wake study, Townsend (22) pointed out the invalidity of the eddy viscosity concept by stating that ϵ is not necessarily a property of the local velocity field but is dependent on the history of the traveling fluid elements. The following reasoning results in a formulation which avoids this difficulty. Since ρuw represents the rate of convection of radial momentum across a unit area of the surface of the spatial element by the mean (steady) component of the velocity w; the term $\rho\overline{u'w'}$, the correlation function or co-variance of the fluctuating components, represents the convection of the radial momentum across the elemental surface resulting from a lack of homogeneity in the field. In this case the lack of homogeniety is due to the mean gradients of velocity. If one considers $\frac{\partial u}{\partial r}$ as very small, as is the case for two-dimensional uniform flow over a flat plate, it is seen that two adjacent velocity profiles almost plot on each other. If now we imagine a small element of fluid as in Fig. 3(a) moving from layer A to A', then, by assuming the conservation of momentum during the motion of the lump, an upward moving fluctuation $+w'$ in layer A will be mostly associated with $-u'$ in layer A'; a downward moving fluctuation $-w'$ in layer A will mostly be associated with $+u'$ in layer A". This phenomenon of momentum transfer gives the turbulent shear stress

$\tau_t = -\rho\overline{u'w'}$. However, if the longitudinal mean velocity gradient is not small as in the case of a wall jet, then the exaggerated sketch of two adjacent velocity profiles will not plot on each other as in case (a) but will be as shown in case (b). Again let us imagine a small fluid element moving from layer A to A'. The fluctuation $+w'$ will be mostly associated with $-u'$, but if $+w'$ is not too large, it will be associated with small $+u'$ in the layer A'. This results in a decrease of the turbulent shear stress. A downward-moving fluctuation $-w'$ in layer A will be mostly associated with a larger $+u'$ in the layer A". As a consequence of this phenomenon the magnitude of $\overline{u'w'}$, in the region very close to the wall, will be larger when $\frac{\partial u}{\partial r} < 0$ than when $\frac{\partial u}{\partial r} \approx 0$. Therefore, if the local mean velocity gradient is assumed to be associated with the turbulent shear stress, then τ_t must not be a function of $\frac{\partial u}{\partial z}$ only, but must include the velocity gradient $\frac{\partial u}{\partial r}$ also. This leads to the adoption of the following simple relation

$$\tau_t \propto \frac{\partial u}{\partial z} + const.\ \frac{\partial u}{\partial r}$$

The turbulent shear stress must increase as the velocity increases; thus by dimensional reasoning one can assume that the simple form of the turbulent shear stress τ_t is

$$\tau_t \approx k\rho z u\left(\frac{\partial u}{\partial z} + \frac{1}{B}\frac{\partial u}{\partial r}\right) \qquad (3\text{-}14)$$

where B corresponds to the constant expressing the influence of the longitudinal velocity gradient $\frac{\partial u}{\partial r}$ on the turbulent shear stress.

Similarity Consideration

Since the turbulent shear stress is much larger than the laminar shear stress except very close to the wall, we neglect the viscous term and introduce the approximate form (3-14); the momentum equation (3-13) can then be written as

$$u\frac{\partial u}{\partial r} + w\frac{\partial u}{\partial z} = \frac{\partial}{\partial z}\left\{k z u\left(\frac{\partial u}{\partial z} + \frac{1}{B}\frac{\partial u}{\partial r}\right)\right\} . \qquad (3\text{-}15)$$

If a similarity solution with velocity $u \propto r^a$ and the boundary-layer thickness $\delta \propto r^b$ is attempted, then we must have the same power of r in Eq. (3-15). Since

$$u\frac{\partial u}{\partial r} + w\frac{\partial u}{\partial z} : \quad r^{2a-1} ,$$

$$\frac{\partial}{\partial z}\left(k z u\frac{\partial u}{\partial z}\right) : \quad r^{2a-b} ,$$

and

$$\frac{\partial}{\partial z}\left(\frac{k}{B} z u\frac{\partial u}{\partial z}\right) : \quad r^{2a-1} ,$$

we must have $b = 1$. Therefore, we can write

$$u \propto r^a \quad \text{and} \quad \delta \propto r. \qquad (3\text{-}16)$$

The relationship expressed in Eq. (3-16) can be derived from the following more general consideration by assuming that the flow is similar. On neglecting the viscous term and by assuming negligible radial pressure gradients, Eq. (3-7) the radial momentum equation becomes:

$$u\frac{\partial u}{\partial r} + w\frac{\partial u}{\partial z} + \frac{\partial \overline{u'^2}}{\partial r} + \frac{1}{r}\left(\overline{u'^2} - \overline{v'^2}\right) + \frac{\partial \overline{u'w'}}{\partial z} = 0 .$$

We introduce

$$\frac{u}{u_m} = \mathcal{U}(\zeta) \quad ,$$

$$\frac{\overline{u'^2}}{u_m^2} = k(\zeta), \quad \frac{\overline{v'^2}}{u_m^2} = s(\zeta), \quad \frac{\overline{w'^2}}{u_m^2} = t(\zeta) \quad ,$$

$$\frac{\overline{u'w'}}{u_m^2} = g(\zeta).$$

and $$\zeta = \frac{z}{\delta}$$

where both δ and u_m are functions of r only.

After simplification the momentum equation becomes

$$-\frac{r}{\delta}\frac{d\delta}{dr}\zeta\mathcal{U}\frac{d\mathcal{U}}{d\zeta} + \frac{r}{u_m}\frac{du_m}{dr}\mathcal{U}^2 + \frac{r}{\delta}\frac{d\delta}{dr}\frac{d\mathcal{U}}{d\zeta}\int_0^\zeta \zeta\frac{d\mathcal{U}}{d\zeta}d\zeta$$

$$-\frac{r}{u_m}\frac{du_m}{dr}\frac{d\mathcal{U}}{d\zeta}\int_0^\zeta \mathcal{U}d\zeta + \frac{d\mathcal{U}}{d\zeta}\int_0^\zeta \mathcal{U}d\zeta - \frac{r}{\delta}\frac{d\delta}{dr}\zeta\frac{dk}{d\zeta}$$

$$+ 2\frac{r}{u_m}\frac{du_m}{dr}k + (k - s) + \frac{r}{\delta}\frac{dg}{d\zeta} = 0 \quad .$$

If the flow is similar this equation represents a relationship between non-dimensional universal functions and should hold true for all values of δ and r . Thus it is necessary that the coefficients of the individual terms should either be zero or be proportional to each other. Since the coefficient of $(k - s)$ is unity, all the other coefficients must be zero or constant. For non-trivial solution the non-repetitive coefficients are

$$\frac{r}{\delta}\frac{d\delta}{dr} \quad , \qquad (3\text{-}17)$$

$$\frac{r}{u_m}\frac{du_m}{dr} \quad , \qquad (3\text{-}18)$$

and $\frac{r}{\delta}$. (3-19)

From condition (3-19) we have

$$\delta \propto r, \text{ i.e. } b = 1, \tag{3-20}$$

and from condition (3-18) we have $u \propto r^a$. (3-21)

Condition (3-17) is satisfied by Eq. (3-20).

Very close to the wall we assume that a transition exists such that the variation of velocity deviated slightly from $u \propto r^a$ say to $u \propto r^{a+\Delta a}$, then the wall shear stress becomes

$$\tau_0 = \mu \left.\frac{\partial u}{\partial y}\right|_0 \propto r^{a+\Delta a-b} .$$

Let us consider a small area on the plate composed of two radial lines and two circular arcs. If the contribution of the turbulent fluctuations is neglected, the change of radial momentum flux across the cylindrical arc surfaces plus that across an upper surface at a great distance from the plate must be equal to the friction force acting on the small area, i.e., we have

$$d\int_0^\infty \rho u^2 r\, d\theta\, dy - u_\infty d\int_0^\infty \rho u r\, d\theta\, dy = -\tau_0 r\, d\theta\, dr$$

where u_∞, the radial velocity at infinity, is zero in this case. If we introduce the parameters $\mathcal{U} = \frac{u}{u_m}$ and $\zeta = \frac{y}{\delta}$ into the above equation, it becomes

$$\rho \frac{d r u_m^2 \delta}{dr} \int_0^\infty \mathcal{U}\, d\zeta = -\tau_0 r .$$

Using the relationships (3-20) and (3-21), it becomes

$$2(1+a) r^{2a+1} \propto - r^{a+\Delta a} .$$

On equating the exponents we find that

$$a - \Delta a = -1.$$

But $2(1 - a) < 0$, i.e., $a < -1$.

Hence $\tau_o \propto r^{-2+2\Delta a}$,

therefore we should have the wall shear stress approximately inversely proportional to the square of the radius.

Notice that in the above derivation, it was assumed that the deviation Δa is small, i.e., the transition in the region near the wall is not large. Thus, in addition to the condition

$$b = 1, \tag{3-22}$$

we must have the following inequalities

$$|\Delta a| \ll a, \qquad a < -1 \quad \text{and} \quad \Delta a < 0. \tag{3-23}$$

Since the transition depends on the velocity and the viscosity, it is expected that the wall shear stress will be a function of the Reynolds number. Thus we have

$$\tau_o \propto \mathcal{D}(Re)\, r^{-2+2\Delta a}. \tag{3-24}$$

Since Δa is not equal to zero, Eq. (3-24) implies that there is a thin transition layer very close to the wall and that no complete similarity exists across the whole boundary-layer. Further, the deviation of the velocity should become larger and larger as r increases, such that, if r becomes large enough, the inner boundary-layer velocity profiles will no longer be similar. Since Δa must be negative, one would expect that the velocity near the wall would be smaller as r increases for a sufficiently large r. Thus, if an approximate similarity exists,

one would expect it to be valid only for limited values of r.

Introducing $\delta = \delta_{0.5} = B\xi$ and $u_m = C\xi^a$, the momentum equations (3-9) and (3-10) approximated to the second order of magnitude are respectively reduced to

$$\underbrace{\left\{a\mathcal{U}^2 - (2+a)\frac{d\mathcal{U}}{d\zeta}\int_0^\zeta \mathcal{U}\,d\zeta\right\}}_{\text{convective term}} + \underbrace{\left\{(2a+1)h - \zeta\frac{dh}{d\zeta} - s\right\}}_{\text{turbulent intensity}}$$

$$+\underbrace{\frac{1}{B}\frac{dg}{d\zeta}}_{\substack{\text{turbulent}\\ \text{shear stress}}} = \underbrace{-\frac{\zeta}{\rho u_m^2}\frac{dp}{d\zeta}}_{\text{pressure term}} + \underbrace{\frac{\nu}{B^2 r u_m}\frac{d^2\mathcal{U}}{d\zeta^2}}_{\text{viscous term}}, \qquad (3\text{-}25)$$

and $$\underbrace{B\left\{(6+a)\mathcal{U}\int_0^\zeta \mathcal{U}\,d\zeta + (a-4)\zeta\mathcal{U}^2 + 2\zeta^2\mathcal{U}\frac{d\mathcal{U}}{d\zeta} - (2+a)\zeta\frac{d\mathcal{U}}{d\zeta}\int_0^\zeta \mathcal{U}\,d\zeta\right\}}_{\text{convective terms}}$$

$$\underbrace{-\zeta\frac{dg}{d\zeta} + (2a+1)g}_{\substack{\text{turbulent}\\ \text{shear stress}}} + \underbrace{\frac{1}{B}\frac{dt}{d\zeta}}_{\substack{\text{vertical turbulent}\\ \text{intensity}}}$$

$$= \underbrace{-\frac{1}{B\rho u_m^2}\frac{dp}{d\zeta}}_{\text{pressure term}} + \underbrace{\frac{\nu}{B r u_m}\left\{a\frac{d\mathcal{U}}{d\zeta} + \zeta\frac{d^2\mathcal{U}}{d\zeta^2}\right\}}_{\text{viscous terms}}. \qquad (3\text{-}26)$$

Comparing the terms in Eqs. (3-25) and (3-26), we notice that not too close to the wall the magnitude of all the terms, except the vertical intensity term $\frac{1}{B}\frac{dt}{d\zeta}$ and the pressure term $-\frac{1}{B\rho u_m^2}\frac{dp}{d\zeta}$, in the vertical component equation (3-26) are less than the terms in the radial component equation (3-25). This is because the boundary growth factor B is much less than one. On examining the viscous term, we further notice that its contribution depends on the velocity. This indicates that no complete similarity exists in the whole boundary-layer.

Chapter IV

EXPERIMENTAL EQUIPMENT AND PROCEDURE

The experimental work was conducted in the Aeromechanics Laboratory of Colorado State University. The equipment and the technique utilized to obtain the desired data are briefly described.

Experimental System

The equipment can be divided into four sections:

1. General experimental arrangement,
2. Instrumentation to measure mean velocity,
3. Instrumentation to measure turbulent quantities,
4. Shear-meter.

General Experimental Arrangement

The experimental system is shown in Figs. 4 and 5. Six runs were made with the following jet orifice diameters and velocities:

Run	Orifice diameter (inch)	Jet orifice velocity (ft/sec)
1	1	370
2	1	223
3	2	340
4	2	279
5	2	174
6	3	333

A 5 HP centrifugal pump driven by a GE induction motor supplied the air to a chamber through a 5-inch pipe. Two layers of screen were placed in the chamber to assist in attaining uniform mixing before the air was ejected through the sharp-edged orifice at the bottom of the chamber. The speed of the jet could be varied from 100 ft/sec to 400 ft/sec and was controlled by a butterfly valve; an auxiliary exhaust pipe outlet was used for making fine adjustments. The jet velocity was measured by means of a Pitot tube mounted at the orifice located at the bottom of the chamber. The jet orifice was placed at a fixed distance of 2 ft. from the flat surface on which it impinged. The flat surface impinged was a 3/16 in. thick aluminum plate with a radius of 69 in.

A carriage, as shown in Fig. 6, was used for mounting the probes. The height of the probes could be adjusted by turning a single threaded screw which was driven by a small DC motor; the speed of the DC motor was changed by adjusting a rheostat. A Vernier scale and a counter were geared to the screwshaft; elevation changes as small as one-thousandth of an inch could be read using the counter and scales. At one sector of the plate, ten circular arcs, 6 in. apart, were marked on the plate surface starting with a distance of 12 in. from the center (stagnation point). These ten stations were used as the primary locations for the measurements. At the start the jet center line was aligned; subsequently a check was made on the symmetry of the flow field by taking four velocity profiles 48 in. from the plate center and 90 degrees apart from each other. These profiles are plotted in Fig. 7 which shows a slight difference between profiles.

Instrumentation to Measure Mean Velocity

The mean velocities were measured using a constant-temperature hot-wire anemometer, the circuit diagram of which is shown in Fig. 8. The sensing element consists of a 0.4 in. length of 0.001 in. diameter platinum wire mounted on the tips of two piano wire prongs, the other ends of which were embedded in a plastic shaft. Calibration of the hot-wire was performed in a circular tank by mounting the hot-wire probe at the end of a rotating arm. The relative velocity of the arm with respect to the swirl induced by the rotation had earlier been obtained using the calibration technique of Cowdry (5).

A pitot tube in conjunction with a water manometer was used to measure the jet velocity which ranged from 100 to 400 ft/sec. Since the calibration tank of the mean velocity hot-wire probe is limited to max. velocity of 21.5 ft/sec. the extrapolation of the calibration curve for higher velocity measurement is not so reliable, and a pitot tube has been used to measure the higher and the over-lapping velocities. However, the result shows some difference between the hot-wire and the pitot tube measurement, as shown in Figs. 23, 24, and 25. This probably attributes to the high turbulent intensities. However, the velocity of the hot-wire measurement according to the correction in Hinze (9) should be about two percent higher close to the wall. And the correction of pitot tube due to high turbulent fluctuation is not certain yet. Therefore, no correction of the measurements has been made for the analysis. The effect of turbulent fluctuation on measurement of

pitot tube deserves further investigation. For velocity less than 5 ft/sec with very large fluctuation, particularly at the outer boundary of the jet, the measurement is rather difficult, higher reading than actual is expected due to the rather long time and large fluctuation.

Instrumentation to Measure Turbulent Quantities

The turbulent intensities $\overline{u'^2}$, $\overline{v'^2}$, $\overline{w'^2}$ and the correlation $\overline{u'w'}$ were measured with a hot-wire anemometer of the constant-temperature type. The circuit diagrams are described by Hubbard (10) and the general view of the anemometer is shown in Fig. 9. The instrument used was a modified form of Model IIHR, Type 3A, Twin-Channel Hot-wire Anemometer and was designed and built by Hubbard. A cross-wire probe, as shown in Fig. 10 was used for all the measurements. A single wire probe was used to compare the intensity in the radial direction $\overline{u'^2}$ with the data measured by the cross-wire probe; the data obtained by the two probes compared about 5 percent of each other.

Tungsten wires were used for the measurement of the turbulent quantities since tungsten has a higher tensile strength than platinum. First tungsten wires, obtained from Sigmund Cohn Company, of approximately 0.000 14 in. diameter with a resistance of approximately 2800 ohms per foot were flash plated with platinum to increase the weight by about 10 percent. This procedure resulted in a platinum covered wire with a final resistance of approximately 2200 ohms per foot. Then the platinum-tungsten wire was copper

plated. This served a double purpose. The copper-plated wire can be handled more easily without breaking; also the copper coating permits one to etch out a piece of the tungsten wire of precise dimensions as required for the use of the hot-wire anemometer.

The plating solution can be made with copper-sulfate crystals as follows:

94 grams $CuSO_4$ + 5 H_2O,

16 cc concentrated H_2SO_4,

500 cc distilled water.

Plating was accomplished by immersing the wire in this solution and passing a current of approximately 100 microamperes per inch from the wire to the solution for 5 hours. A copper wire was used for the positive electrode in this process, and the current limited by an external resistor. The portion of the wire to be plated was not touched at all in order to avoid contamination and, if necessary, the wire was cleaned in sulfuric acid just before plating. At the end of the plating procedure, the wire was cleaned by reversing the current direction for a short time. After carefully soldering the wire on the tips of the prongs, the central part of the copper plating was removed by etching the wire with nitric acid. A brush was made by drawing out a small (4mm) glass tube to a nozzle form in a flame and inserting a cotton thread (No. 50) in this nozzle. This brush was dipped in concentrated nitric acid which was held by capillary action and fed out as needed.

The etching process was inspected under a binocular microscope to be certain that the wires were straight, perpendicular to

each other and etched on both sides. With patience and practice, matched wires with the same resistance could be made.

Shear-Meter

In order to measure the wall shear stress, a shear-meter was designed. Several types of shear-meters such as those operating on heat transfer principles, floating element, pressure relationship (Preston tube, etc.) were considered. The device finally used was of the floating element type. Due to the relatively low speeds, highly sensitive measurements of very small forces were required. After a few attempts, a simple device made from a 100 ma. DC milliam-meter was used. Thus, the precision fabrication of this meter and the extremely small friction on the bearing of the pointer were incorporated into the design. A thin magnesium disk 1 1/2 in. in diameter was mounted on the tip of the pointer and perpendicular to it as shown in Fig. 11 and 12. A DC power supply, Model AB-128 Scintillonics Inc., with 100 milliampere full scale was connected in series with the shear-meter. A variable resistor was inserted in the circuit to limit the current. Then the shear-meter was mounted in a 4 5/8 in. diameter predrilled hole on the plate surface and adjusted flush with the smooth surface. The small friction force created by the flow over the disk tended to move the floating element downstream. The flow friction moment was then balanced by the increase in magnetic torque due to an increase in current which could be read from the DC power supply. The flow friction moment was considered balanced when the disk was not touching either side

of the gap of about 0.006 in. The friction force was then read from the static calibrated current-force curve as shown in Fig. 13. Since the calibration of the shear-meter is assumed to be independent of the tilting of the meter, it was more convenient and easier to calibrate it by turning it 90° in order to hang various small weights on the arm of the pointer. The corresponding current was then read. This gives a static calibration with a sensitivity of 2 micropounds per square in. The repeatibility of the calibration ensures the reliability of the measurement in principle. However, the turbulent flow causes the disk to flutter, thus making the observations of the neutral position difficult; it is estimated that by averaging several meter readings one can duplicate the data to within 15 percent. A dynamic check was made on a flat plate with a sharp leading edge placed in a 6 x 6 ft. wind tunnel. The results are shown in Fig. 14.

Chapter V

ANALYSIS AND DISCUSSION OF DATA

The diffusion of a circular air jet impinging normally on a smooth flat plate is characterized by the spreading of the jet radially along the plate. It is convenient to divide the space into four zones following Poreh et al. (16); each zone is characterized by a distinct pattern of flow as shown in Fig. 15. The four zones are:

I. Zone of flow establishment,

II. Zone of established free circular jet,

III. Zone of stagnation and deflection,

IV. Zone of fully developed radial wall jet.

I. Zone of Flow Establishment

The characteristics of this transition zone were not investigated in the study. According to existing experimental data, Albertson et al. (1) and Poreh et al. (16), it extends up to $\frac{H-\delta}{D} \approx 9$, where H is the height of the jet orifice from the plate.

II. Zone of Established Free Circular Jet

This zone is well known as free-jet flow. Theoretically this zone has been studied by Goertler (8) who adopted the assumption of Prandtl that the eddy viscosity ε is constant across the transverse section and is proportional to the maximum velocity

and the width of the jet. The similarity solution concludes that the velocities are inversely proportional to the distance from the origin.

In this study a few profiles of velocity, turbulent intensities and turbulent shear stress were measured for two purposes. First, it indicates the flow conditions of the free jet so that other investigators might use this for comparison. Secondly, by roughly comparing with the existing extensive studies of the free jet, by Corrsin as in Hinze (9) and by Laurence (13), it gives some indication of the reliability of the turbulence measurements. However, due to different jet conditions it is difficult to compare the results exactly. Typical profiles are shown in Figs. 16 and 17.

III. Zone of Deflection and Stagnation

Vidal (23) has pointed out that for $\frac{x}{D} \approx 1$ the region is primarily laminar. Static pressure measurement on the wall indicate that the pressure follows the law for irrotational flow very close to the center; but from $r \approx 3$ in. from the stagnation point, the pressure decreases exponentially as shown in Figs. 18 and 19. By comparing the slope in Fig. 19, we notice that the pressure drops so fast that it ensures a quick approach to the condition of constant wall static pressure. According to the pressure measurements, the total pressure on the plate is about 30 percent larger than the momentum flux at the jet orifice. Murray et al. (15) and Poreh et al. (16) obtained similar results. This effect is probably due to the downward vertical component of velocity produced by the entrainment process which exerts momentum

flux in addition to that at the jet orifice. The vertical component of velocity calculated from the mass conservation equation (3-5) is shown in Fig. 20. In this region the maximum peak velocity u_m occurs due to the static pressure gradient. Bradshaw, et al. (3) point out that the maximum wall shear stress also occurs at this location.

IV. Zone of Fully Developed Radial Wall Jet

Mean Velocity

A typical set of velocity profiles close to the central portion is shown in Fig. 21. At this region, as r increases, a change of the velocity profile toward approximate similarity curves, for the chosen parameters $\zeta = \frac{z}{\delta_{0.5}}$ and $\mathcal{U} = \frac{u}{u_m}$, is indicated. Compared with Figs. 23 and 24, it shows in this case that the flow is apparently fully developed for r = 12 in. As in Table I ten stations each 6 in. apart along a radius were marked on the plate with the first station 12 in. from the stagnation point. Typical velocity profiles are shown in Figs. 22, 23, and 24 in dimensional and non-dimensional form respectively. It is seen that within the accuracy of the measurements an approximate similarity has been found with such simple parameters as $\zeta = \frac{z}{\delta_{0.5}}$ and $\mathcal{U} = \frac{u}{u_m}$. As compared in Fig. 26, the data using the parameters $\frac{u}{u_*}$ and $\frac{z u_*}{\nu}$ do not follow the curve for smooth pipe flow. An average value of 2×10^{-4} ft^2/sec was used for ν in this calculation for a temperature range of 70° F to 85° F. However, the semi-log relationship still seems to hold but for a rather small region. Close to the wall the shifting of the

points seems to indicate a decrease in the laminar sublayer thickness due to the influence of the high turbulent intensities.

The assumption of similarity yields the relations (3-20) and (3-21), i.e.

$$u \propto r^a \quad \text{and} \quad \delta \propto r.$$

Introducing a reference velocity u_m and a reference boundary-layer thickness $\delta_{0.5}$, we let

$$\frac{u_m}{-w_{j_o}} = A\left(\frac{D}{r}\right)^{-a} \quad \text{and} \quad \delta_{0.5} = B\,r. \tag{5-1}$$

These relationships have been plotted in Figs. 27 and 28. It is noticed that the growth rate of the boundary-layer thickness is practically independent of the jet-orifice velocity and diameter. It is also seen that the results agree with the analysis fairly well, except that for the growth of the boundary-layer thickness a shifting of the virtual origin from the stagnation point is observed at about 3.3 in. The constants are determined as $a = -1.10$, $A = 1.18$ and $B = 0.084$. Since a is close to -1, in analogy of the free circular jet, this indicates that the radial wall jet is predominately controlled by the mixing of the free jet and the presence of the wall has no large effects on the whole flow. This phenomenon shows that large scale eddies are penetrating into the boundary-layer by the free jet mixing. This also is one of the reasons why the zero turbulent shear stress does not occur at the peak velocity as will be discussed later.

A comparison of Glauert's curve with the measured mean velocity data is made in Figs. 23, 24 and 25. There is an

apparent difference between the hot-wire and the pitot tube measurements. Since the correction for the hot-wire measurements is small and that for the pitot tube measurements is uncertain, the analysis and calculations are based on the hot-wire measurements.

The same non-dimensional velocity profile curve is observed in the outer boundary-layer for all runs; however, in the inner boundary-layer, the non-dimensional velocity shows to be larger for larger Reynolds number as shown in Fig. 24a.

Turbulent Intensities

The turbulent intensities in three perpendicular directions radial $\overline{u'^2}$, circumferential $\overline{v'^2}$ and vertical $\overline{w'^2}$ were measured. All the plots show an approximate similarity as seen from the typical profiles presented in Figs. 29-34. In comparing these results with Klebanoff's results (11) on two-dimensional uniform flow over a smooth plate, it is seen that close to the wall the turbulent intensities $\frac{\sqrt{\overline{u'^2}}}{U_m}$, $\frac{\sqrt{\overline{v'^2}}}{U_m}$ and $\frac{\sqrt{\overline{w'^2}}}{U_m}$ in the wall jet are much larger, and in fact they are about four times as much as the corresponding intensities measured by Klebanoff. This again indicates the strong penetration of eddies from the free jet into the inner boundary layer; however, the order of magnitude $\sqrt{\overline{u'^2}} > \sqrt{\overline{v'^2}} > \sqrt{\overline{w'^2}}$ remains the same. This demonstrates that the influence of the free jet dominates most portions of the boundary-layer and that the influence of the wall is limited to a very small region close to the wall. It is noticed that the absolute magnitudes of $\sqrt{\overline{u'^2}}$ and $\sqrt{\overline{v'^2}}$ remain fairly constant and then gradually drop off near the outer boundary, and that the magnitude $\sqrt{\overline{w'^2}}$

first increases as z increases, reaches its maximum value at about $\zeta \approx 0.4$ and then gradually decreases at the outer boundary. The ratios of the intensities $\frac{\sqrt{\overline{v'^2}}}{\sqrt{\overline{u'^2}}}$ and $\frac{\sqrt{\overline{w'^2}}}{\sqrt{\overline{u'^2}}}$ are shown in Fig. 35. We observe that the ratio $\frac{\sqrt{\overline{w'^2}}}{\sqrt{\overline{u'^2}}}$ is by no means constant. This implies that Prandtl's assumption of $u' \propto w'$, for the turbulent shear stress, cannot be applied in this region of the wall jet. Further we observe that the ratio $\frac{\sqrt{\overline{w'^2}}}{\sqrt{\overline{u'^2}}}$ in the outer boundary-layer is larger than that in a free circular jet as shown by Hinze (9).

Turbulent Shear Stress

The measurements of the turbulent correlation were scattered in the wall jet probably due to the effect of the low velocity, the large turbulence scale and the high turbulence intensity on the hot wire technique. It is difficult to recognize whether any approximate similarity exists for the turbulent shear stress. The non-dimensional form of $\frac{\overline{u'w'}}{u_m^2}$ has been plotted against the parameter $\frac{y}{\delta_{0.5}}$ as shown in Fig. 36. It is observed that the turbulent shear stress τ_t is about twice as large as that in a free circular jet. Of course, this is closely related to the turbulent intensities which indicate the same phenomena. Particularly we notice that the turbulent shear stress does not become zero at the point where the velocity gradient in the vertical direction is zero. This does not agree with the concept of eddy viscosity. However, the argument in Chapter III indicates that we should not expect to have the characteristic location of the zero

turbulent shear stress if the velocity gradient in the radial direction is taken into consideration. This shifts the location of the zero turbulent shear stress away from the location of the zero velocity gradient in the vertical direction.

In the radial wall jet case, by using the parameters

$$\mathcal{U} = \frac{u}{u_m} \qquad \text{and} \qquad \zeta = \frac{z}{\delta_{0.5}}$$

and the established relations

$$\frac{u_m}{-w_{j_0}} = A\left(\frac{D}{r}\right)^{-a}, \qquad \delta_{0.5} = B r \quad ,$$

the form

$$\tau_t = -\rho \overline{u'w'}$$

$$\doteq \rho k_2 z u \left(\frac{\partial u}{\partial z} + \frac{1}{B}\frac{\partial u}{\partial r}\right) \tag{5-2}$$

becomes

$$\frac{\overline{u'w'}}{u_m} \approx -k\zeta\mathcal{U}\left[(1-\zeta)\frac{d\mathcal{U}}{d\zeta} + a\mathcal{U}\right]. \tag{5-3}$$

This indicates that the plot of $\frac{\overline{u'w'}}{u_m}$ has a similar form and that the constant k is to be determined experimentally. By taking values from the measured velocity profile to evaluate $\mathcal{U}$ and $\frac{d\mathcal{U}}{d\zeta}$ the right-hand side of Eq. (5-3) may be evaluated. A plot of Eq. (5-3) is shown in Fig. 37 for comparison with the measured distribution of the turbulent shear stress. The general features agree fairly well and the constant k is estimated from the curve to be 0.050.

If the same approximate formulation as that of Eq. (5-3) is applied to the circular free jet, a comparison of the computed and measured curves show fairly good agreement with the choice of the constant $\alpha = 0.034$, see Fig. 38. By plotting the ratio as shown in Figs. 39 and 40 where $q^2 = \overline{u'^2} + \overline{v'^2} + \overline{w'^2}$ is the turbulent kinetic energy, it is noticed that the ratio is approximately constant in the outer boundary-layer. By comparing with Fig. 7-15 of Schlichting (18) it is seen that both in the two-dimensional uniform flow over a flat plate and in the wall jet flow the ratios are about constant in the outer boundary-layer. However, this does not justify the validity of Prandtl's assumption, since we have shown that the ratio $\frac{\sqrt{\overline{w'^2}}}{\sqrt{\overline{u'^2}}}$ does not approach a constant in that region.

Balance of Reynolds Equations

Since all the terms in the Reynolds equations except the pressure term were measured, a check of the balance of the momentum equations seems pertinent. If all terms except first order ones are neglected from the Reynolds equation for the vertical component (3-10), it is noticed that the only term which is large enough to balance the vertical intensity gradient is the pressure gradient in the vertical direction as shown in Fig. 41. By integration and the assumption of constant wall pressure, we obtain

$$\overline{w'^2} \approx p_w - p \qquad (5\text{-}4)$$

or

$$\frac{p_w - p}{\frac{1}{2}\rho u_m^2} \approx 2\,\frac{\overline{w'^2}}{u_m^2} \,. \qquad (5\text{-}5)$$

Thus, we notice that the static pressure is less than the wall static pressure. The maximum difference with respect to the dynamic pressure is about twice the magnitude of the square of the relative vertical intensity, i.e., about twelve percent of the dynamic pressure in this case. The second order terms of Eq. (3-10) were also numerically calculated as seen in Fig. 41. It is found that the contributions of the turbulent shear stress and the convective terms were negligible in the whole boundary-layer. Using the approximate relation (5-4), Eq. (3-25) becomes

$$\left\{2\bar{u}^2-(2+a)\frac{d\bar{u}}{d\zeta}\int_0^{\zeta}\bar{u}\,d\zeta\right\}+\left\{(2a+1)h-\zeta\frac{dh}{d\zeta}-s\right\}+\frac{1}{B}\frac{d\beta}{d\zeta}$$

convective term intensity term turbulent shear

$$=\quad -\zeta\frac{dh}{d\zeta}\quad+\quad\frac{\nu}{B\,r\,U_m}\frac{d^2\bar{u}}{d\zeta^2}\ .$$

pressure viscous term (5-6)

The numerical results have been plotted in Fig. 42. It is seen that the convective term is mainly counter-balanced by the turbulent shear stress, and that the radial pressure gradient term is small across the whole boundary-layer. However, the balance is quite poor. The discrepancy is probably due to the following four reasons:

1. Possible error in measurement may exist due to very high local turbulent intensities, especially in those regions close to the wall and at the outer boundary.
2. No corrections were made for the angle between the

mean velocity vector and the probe x-wires axis. However, it is estimated that the mean velocity vector is about four degree downward at the height of $\delta_{0.5}$. The inclination increases rapidly as the height increases.

3. The assumption of similarity for the momentum equation is only approximately valid.
4. The Reynolds equation may not be valid for divergent flows with high turbulent intensities.

It is of interest that the vertical intensity term in the Reynolds equation for the vertical component (3-26) is about twice as large as the largest term in the Reynolds equation for the radial component (3-25), in the inner boundary-layer. In their study of the momentum distribution of turbulent boundary layers in adverse pressure gradients, Sandborn, et al. (17) point out that the vertical intensity term in the Reynolds equation for the vertical component is much larger than the terms in the Reynolds equation for the longitudinal component; however, the effect of the vertical intensity is limited to a much thinner region close to the wall.

Momentum Integral Equation

According to the approximate similarity condition, the integration of Eq. (5-6) yields

$$g - \frac{\nu}{B r U_m}\frac{dU}{d\zeta} = B\left\{2(1+a)\int_{\zeta}^{\infty} U^2 d\zeta + (2+a)U\int_{0}^{\zeta} U d\zeta\right\}$$

viscous term convective term

$$+\left\{\zeta h + 2(1+a)\int_{\zeta}^{\infty} h\,d\zeta - \int_{\zeta}^{\infty} s\,d\zeta\right\} + \left\{\zeta t + \int_{\zeta}^{\infty} t\,d\zeta\right\} \qquad (5\text{-}7)$$

intensity term pressure term

The numerical calculation of Eq. (5-7) has been plotted in Fig. 36. The possible reasons for the discrepancy have been mentioned in the previous section. The approximate similarity seems to hold for the mean velocity and the turbulent intensities; however, the similarity of turbulent shear stress cannot be ascertained due to the scatter in the data. Since the turbulent shear stress does not enter into the evaluation of the wall shear stress as determined from Eq. (5-7) for $\zeta = o$, it seems very unlikely that the calculated value of wall shear stress is so much larger than the measured one as shown in Fig. 36, especially because the measured turbulent shear stresses extrapolate close to the measured wall shear stress. In addition the measured wall shear stresses are only slightly larger than the existing measured data for two-dimensional wall jets. Therefore, since it is known that the momentum integral equation does not predict the wall shear stress in adverse pressure gradient flows, probably due to secondary flow, the writer is inclined to suspect the validity of the momentum integral equation for the evaluation of the shear stress for the present case of divergent flow with high turbulent intensities.

The shift in the location of the zero turbulent shear stress from the location of zero velocity gradient $\frac{\partial u}{\partial \eta}$ towards the wall is a common feature of wall jet flows, Bradshaw, et al. (4). It is observed that the contribution of turbulent intensities,

which include the effect of the small pressure gradient in the radial direction, changes not only the magnitude of the turbulent shear stress but more important the wall shear stress. This can be attributed to the divergent effect of the flow. This difference is expected to be small for ordinary boundary-layers where the turbulent intensities are less than ten percent.

Wall Shear Stress

The distribution of wall shear stress as shown in Figs. 43 and 44 indicates that the wall shear stress varies approximately as the inverse square of the radius r. However, according to the analysis in Chapter III, the wall shear stress should vary as $r^{-2+2\Delta Q}$ where $\Delta Q = -0.10$. This deviation is probably due to the assumption of a central jet source at the stagnation point.

It is seen from Figs. 26 and 35 that the wall shear stress is larger for the wall jet than for the smooth pipe flow. This is consistent with the findings of Kline, et al. (12); they find that the increase of turbulent intensity in the mean stream greatly increases the velocity gradient near the wall, and consequently increases the wall shear stress.

Experimentally, for practical uses, we have the following relation

$$\frac{\tau_o}{\rho w_{jo}^2} = \alpha \cdot \left(\frac{D}{r}\right)^2$$

where the shear proportionality α is a function of the Reynolds number $R_e = \frac{w_{jo} D}{\nu}$ as shown in Fig. 45.

Chapter VI

CONCLUSIONS

As a result of this study of a radial wall jet produced by the normal impingement of a circular air jet, several conclusions may be drawn. The most important conclusions are:

1. The static pressure in the region close to the central portion decreases exponentially with respect to the radius r such that the pressure rapidly approaches a constant away from the central portion.

2. The decay of the peak velocity and the growth of the boundary-layer thickness can be approximated by the following simple functions of the radius r:

$$\frac{u_m}{-w_{j_o}} = A\left(\frac{D}{r}\right)^{-a} \quad \text{and} \quad \delta_{0.5} = B\,r,$$

with $A = 1.18$, $a = -1.10$ and $B = 0.084$.

The phenomena are approximately similar to that of a free circular jet.

3. The characteristics of the whole boundary-layer is dominated by the effect of the free jet, and the wall influences the flow only in a very limited region close to the wall. This results in much higher turbulent intensities and turbulent shear stress which increases the wall shear stress for this flow case

as compared to two-dimensional uniform flow over a flat plate and smooth pipe flow.

4. By physical reasoning and dimensional analysis, the following form for the turbulent shear stress is proposed

$$\tau_t \approx k \rho \beta u \left(\frac{\partial u}{\partial \beta} + \frac{1}{B} \frac{\partial u}{\partial r} \right)$$

with the constant k determined experimentally as 0.05. It is found that the distribution of turbulent shear stress in a free circular jet can also be approximately calculated from this formulation with $k = 0.034$.

5. The relative turbulent quantities plotted against the parameter ζ show approximate similarity, except that the data on turbulent shear stress is considerably scattered.

6. The ratio of turbulent intensities $\frac{\sqrt{\overline{w'^2}}}{\sqrt{\overline{u'^2}}}$ is in general not a constant across the boundary-layer which indicates non-applicability of Prandtl's assumption $u' \propto w'$ for this case.

7. The balance of the Reynolds equation and the evaluation of shear stresses from the integral momentum equation are quite poor. This is probably either due to some unknown systematic error in the data or due to the invalidity of the Reynolds equation for divergent flows with high turbulent intensities.

8. Experimentally the wall shear stress τ_0 is approximately proportional to the square of the inverse of the radial distance r; but according to the analysis τ_0 is proportional to $r^{-2.244}$. This deviation probably is due to the assumption of the central source at the stagnation point. The experimental

relation can be put in the following non-dimensional form for practical uses where the known quantities are usually the jet diameter D, orifice velocity $-w_{j_o}$ and the distance from the stagnation point r:

$$\frac{\tau_o}{\rho w_{j_o}^2} = \mathcal{A} \cdot \left(\frac{D}{r}\right)^2$$

where $\mathcal{A}$ the shear proportionality is a function of Reynolds number $R_e = \frac{w_{j_o} D}{\nu}$.

BIBLIOGRAPHY

1. Albertson, M. L., Dai, Y. B., Jenson, R. A. and Rouse, H. Diffusion of submerged jets. Trans. ASCE 115, 26, 1950.

2. Bakke, P. An experimental investigation of a wall jet. J. Fluid Mechanics 2, 467, 1957.

3. Bradshaw, P. and Love, E. M. The normal impingement of a circular air jet on a flat plate. Great Britain, Aeronautical Research Council A.R.C. 21, 268, Sept. 1959.

4. Bradshaw, P. and Gee, M. T. Turbulent wall jets with and without an external stream. Aeronautical Research Council R. and M. 3252, 1962.

5. Cowdrey, C. F. A note on the calibration and use of a shielded hot-wire anemometer for very low speeds. Journal of Scientific Instruments 27, 327, 1950.

6. Eskinazi, S. and Kruka, V. Mixing of a turbulent wall-jet into a free-stream. Proc. of ASCE 88, No. EM2, 125, April 1962.

7. Glauert, M. B. The wall jet. J. Fluid Mech. 1, 625, 1956.

8. Goertler, H. Berechnung von Aufgaben der freien Turbulenz auf Grund eines neuen Naherungsanstzes. ZAMM 22, 244, 1942.

9. Hinze, J. O. Turbulence. McGraw-Hill Book Co., New York, 1959.

10. Hubbard, P. G. Operating manual for the 11HR hot-wire and hot-film anemometers. State University of Iowa. Studies in Engr., Iowa City, Iowa, Bulletin 37, 1957.

11. Klebanoff, P. S. Characteristics of turbulence in a boundary layer with zero pressure gradient. NACA Report 1247, 1955.

12. Kline, S. J., Lisin, A. V. and Waitman, B. A. An experimental investigation of the effect of free stream turbulence on the turbulent boundary layer growth. NASA TN D368, 1960.

13. Laurence, J. C. Intensity, scale, and spectra of turbulence in mixing region of free subsonic jet. NACA Report 1292, 1956.

BIBLIOGRAPHY.—(Cont'd.)

14. Murray, R. L., Nelson, L. E. and Steven, J. R. Deflection of a jet by a normal wall. Proc. ASCE Hyd. Div. paper 1038, 82, 4, 1956.

15. Myers, G. E., Schauer, J. J. and Eustis, R. H. The plane turbulent wall jet. Part 1. Jet development and friction factor. Stanford University, Dept. of Mech. Engr., Stanford, Calif., NSF G9705 Tech. Rep. 1, June 1961.

16. Poreh, M. and Cermak, J. E. Flow characteristics of a circular submerged jet impinging normally on a smooth boundary. Proc. of the Sixth Midwest Conference on Fluid Mechanics, p. 198, Sept. 1959.

17. Sandborn, V. A. and Slogar, R. J. Study of the momentum distribution of turbulent boundary layers in adverse pressure gradients. NACA TN 3264, 1955.

18. Schlichting, H. Boundary Layer Theory. Pergamon Press, London, 1955.

19. Schwarz, W. H. and Cosart, W. P. The two-dimensional turbulent wall-jet. J. Fluid Mech. 10, Part 4, 481, 1961.

20. Sigalla, A. Experimental data on turbulent wall jets. Aircraft Engineering 30, 131, May 1958.

21. Sigalla, A. Measurements of skin friction in a plane turbulent wall jet. J. Royal Aero. Soc. 62, 873, Dec. 1958.

22. Townsend, A. A. The Structure of Turbulent Shear Flow. Cambridge University Press, London, 1956.

23. Vidal, R. J. Aerodynamic processes in the downwash impingement problem. Institute of the Aerospace Sciences, New York, No. 62-36, 1962.

TABLE I

Run	1			2			3			4			5			6		
D in	1			1			2			2			2			3		
$-W_{jo}$ ft/sec	370			223			340			279			174			333		
r in	U_m ft/sec	U_* ft/sec	$\delta_{0.5}$ in	U_m ft/sec	U_* ft/sec	$\delta_{0.5}$ in	U_m ft/sec	U_* ft/sec	$\delta_{0.5}$ in	U_m ft/sec	U_* ft/sec	$\delta_{0.5}$ in	U_m ft/sec	U_* ft/sec	$\delta_{0.5}$ in	U_m ft/sec	U_* ft/sec	$\delta_{0.5}$ in
12	30.0	2.07	1.27	18.7	1.36	1.19	49.4	3.63	1.28	44.4	2.84	1.20	30.0	1.93	1.16	—	—	—
18	19.7	1.32	1.85	12.0	0.900	1.83	35.5	2.36	1.89	28.7	1.85	1.86	18.7	1.27	1.82	52.9	—	1.38
24	14.2	0.975	2.40	8.6	0.664	2.33	26.8	1.71	2.47	21.0	1.37	2.39	13.5	0.938	2.36	39.2	—	1.90
30	10.8	0.771	2.92	6.3	0.527	2.75	21.1	1.38	2.99	16.8	1.10	2.89	11.1	0.745	2.78	31.2 30.0	—	2.36 2.90
36	8.4	0.636	3.54	5.1	0.435	3.40	16.7	1.14	3.43	13.2	0.900	3.34	9.0	0.615	3.21	25.2 24.6	1.44	2.82 3.41
42	7.31	0.545	3.89	4.2	0.364	3.82	14.3	0.971	3.85	10.9	0.765	3.85	7.5	0.524	3.80	20.8	1.22	4.20
48	6.52	0.478	4.26	3.7	0.322	4.25	12.8	0.843	4.26	9.1	0.664	4.35	6.2	0.456	4.23	18.8	1.07	4.59
54	5.80	0.419	4.90	3.1	0.286	5.00	10.6	0.749	4.81	8.5	0.500	5.00	5.1	0.404	4.84	16.2	0.943	5.00
60	5.24	0.374	5.27	2.6	0.256	5.60	9.6	0.669	5.23	7.5	0.526	5.00	4.6	0.360	5.00	14.6	0.845	5.90
66	4.60	0.338	5.78	—	—	—	8.5	0.602	5.60	—	—	—	—	—	—	—	—	—

NOTES: $\nu \simeq 2.0 \times 10^{-4}$ ft²/sec

FOR Run 6

r = 18 – 36 in. Measured by pitot tube

30 – 60 in measured by hot wire

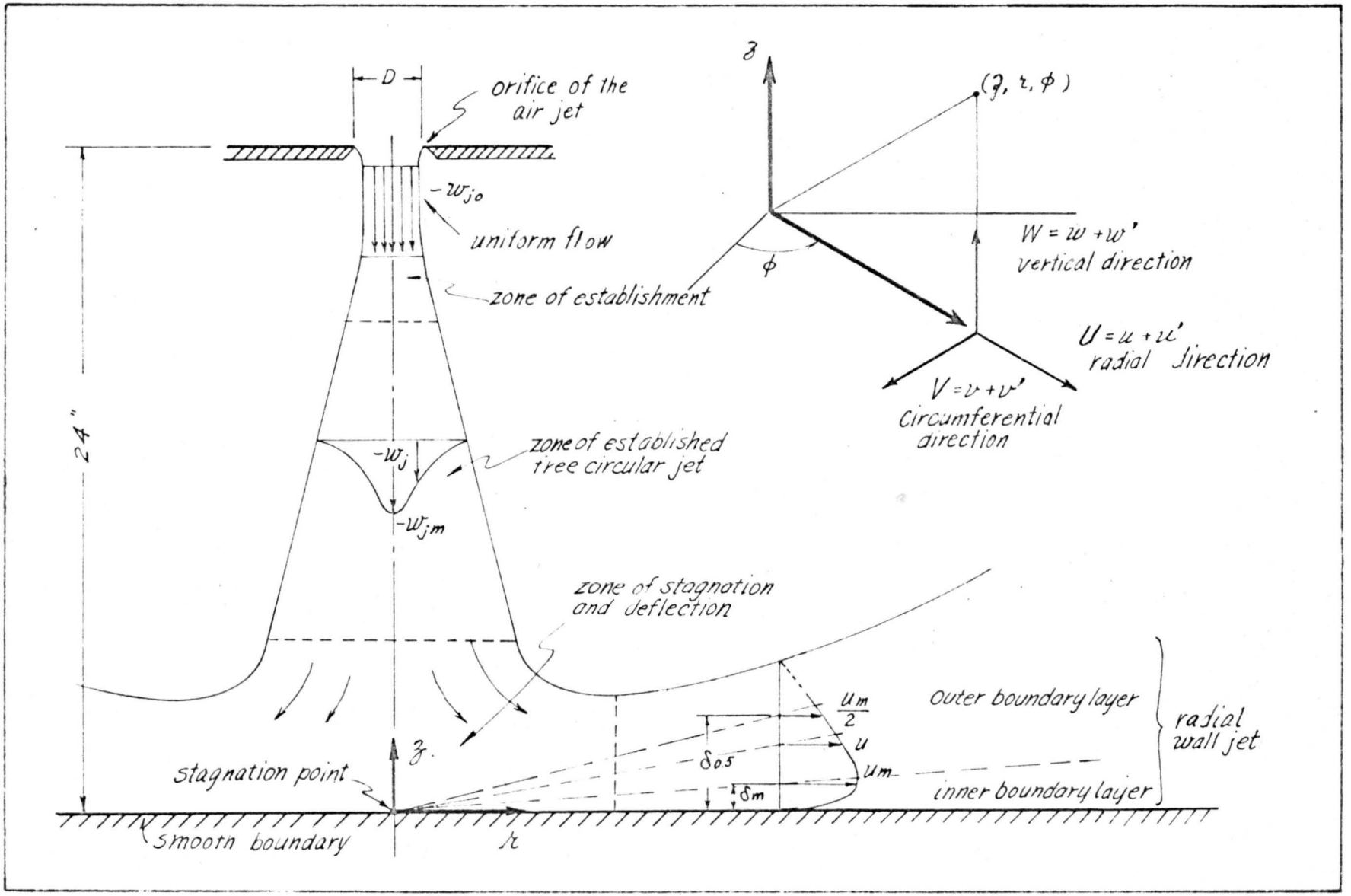

FIG. 1 COORDINATE SYSTEM AND NOTATION

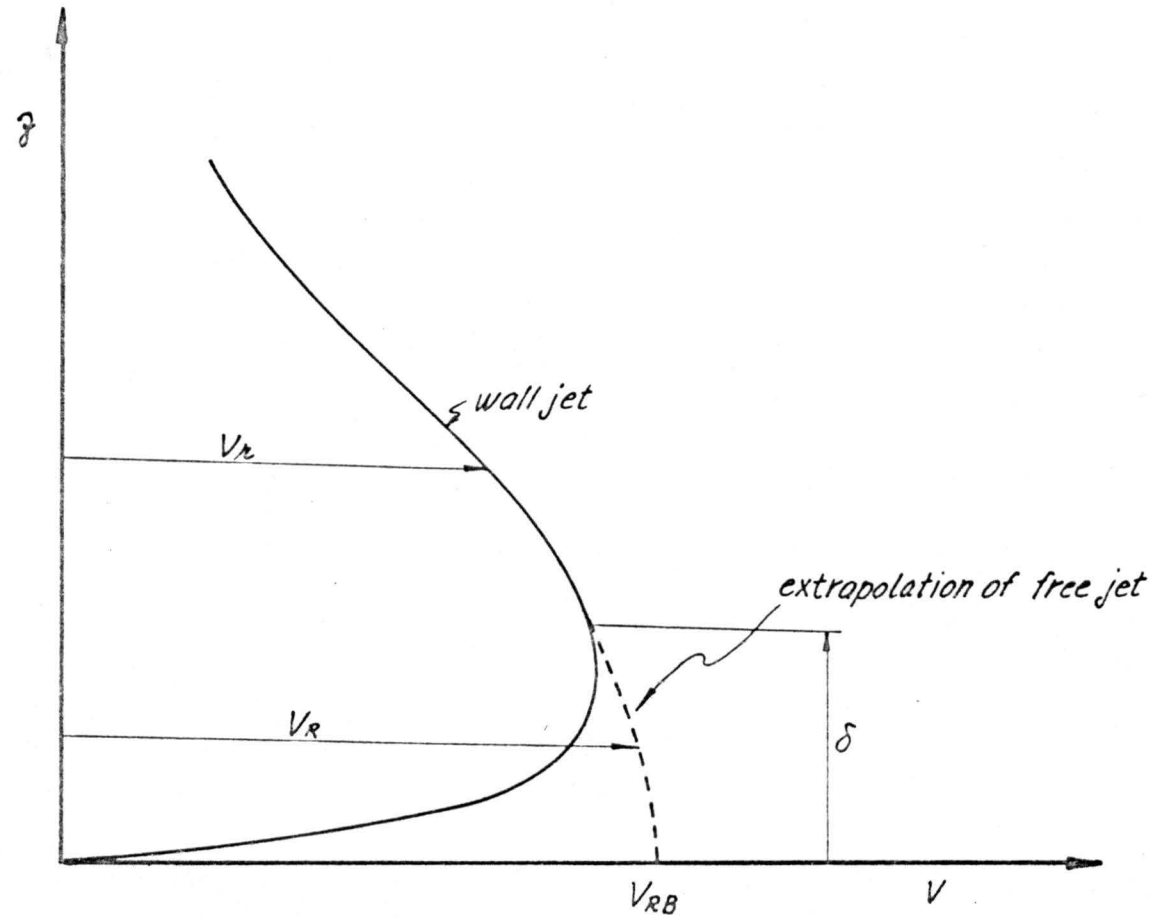

FIG. 2 NOTATION IN POREH'S ANALYSIS

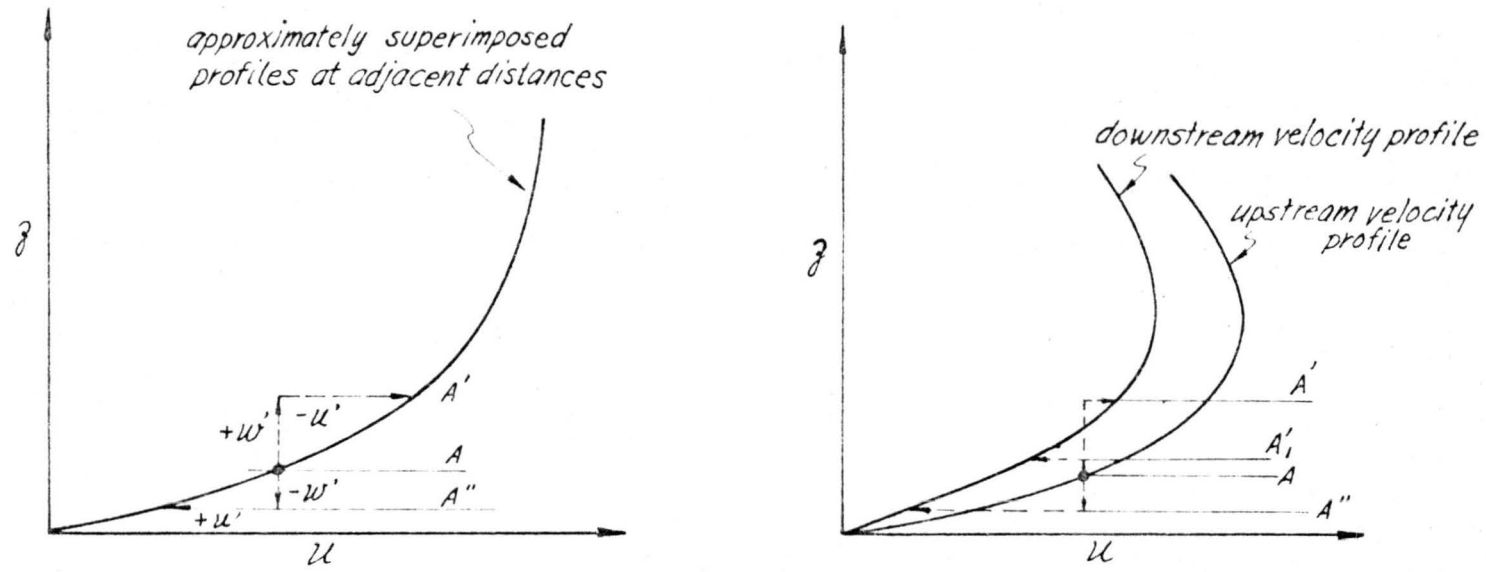

(a) $\frac{\partial u}{\partial z} \approx 0$ as in two-dimensional uniform flow over flat plate

(b) $\frac{\partial u}{\partial z} < 0$ as in wall jet

FIG. 3 TWO ADJACENT VELOCITY PROFILES FOR THE CASE $\frac{\partial u}{\partial z} \approx 0$ AND THE CASE $\frac{\partial u}{\partial z} < 0$

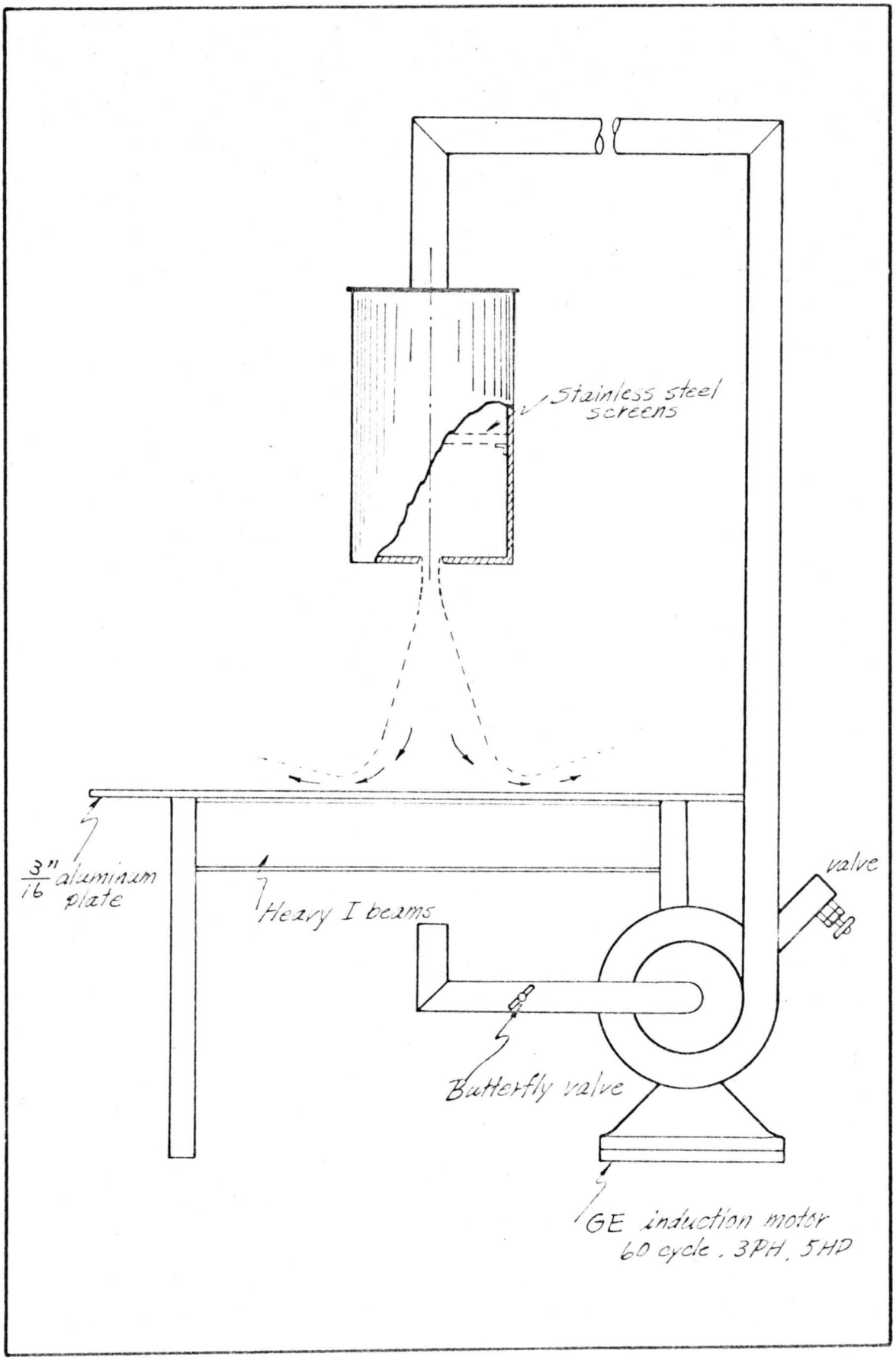

FIG. 4 SCHEMATICAL SET-UP OF EXPERIMENT

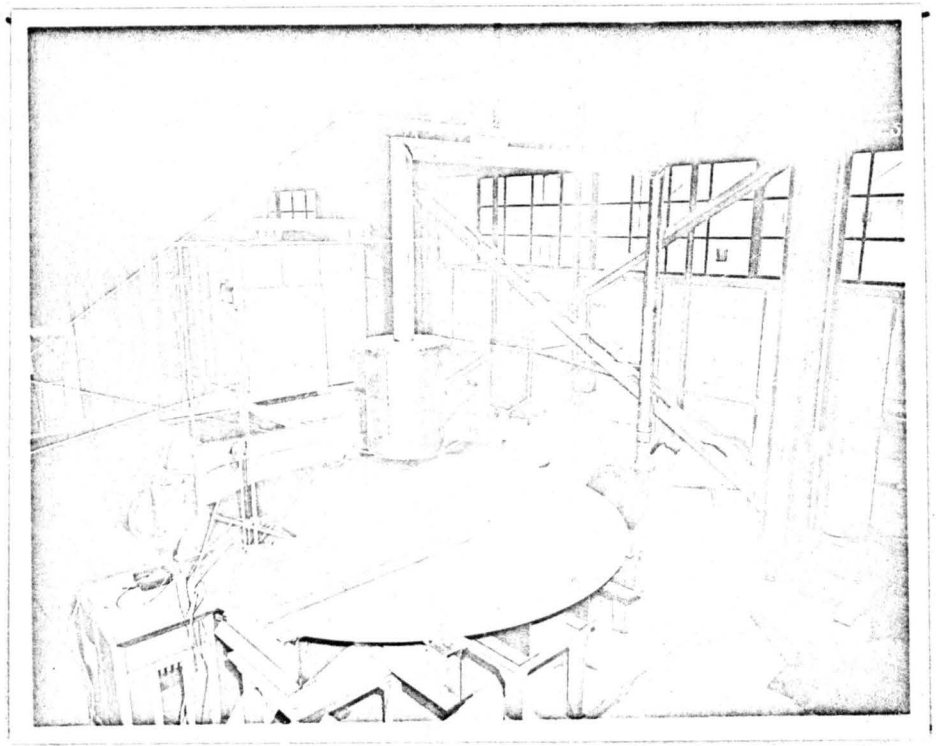

FIG. 5 VIEW OF THE GENERAL SET-UP

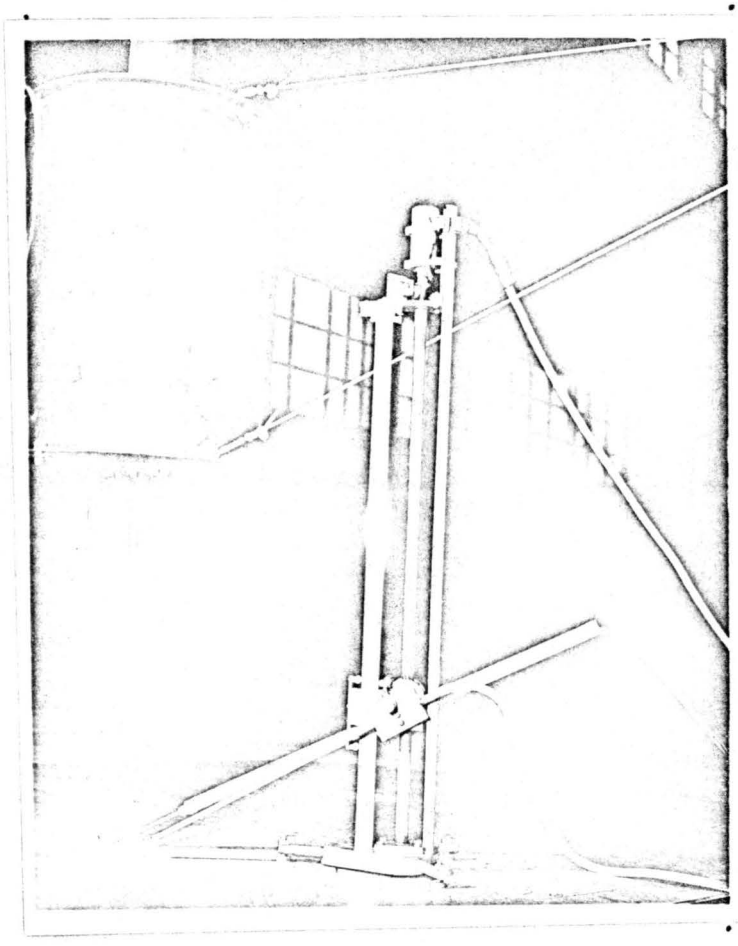

FIG. 6 CARRIAGE AND THE MOUNTING OF THE PROBES

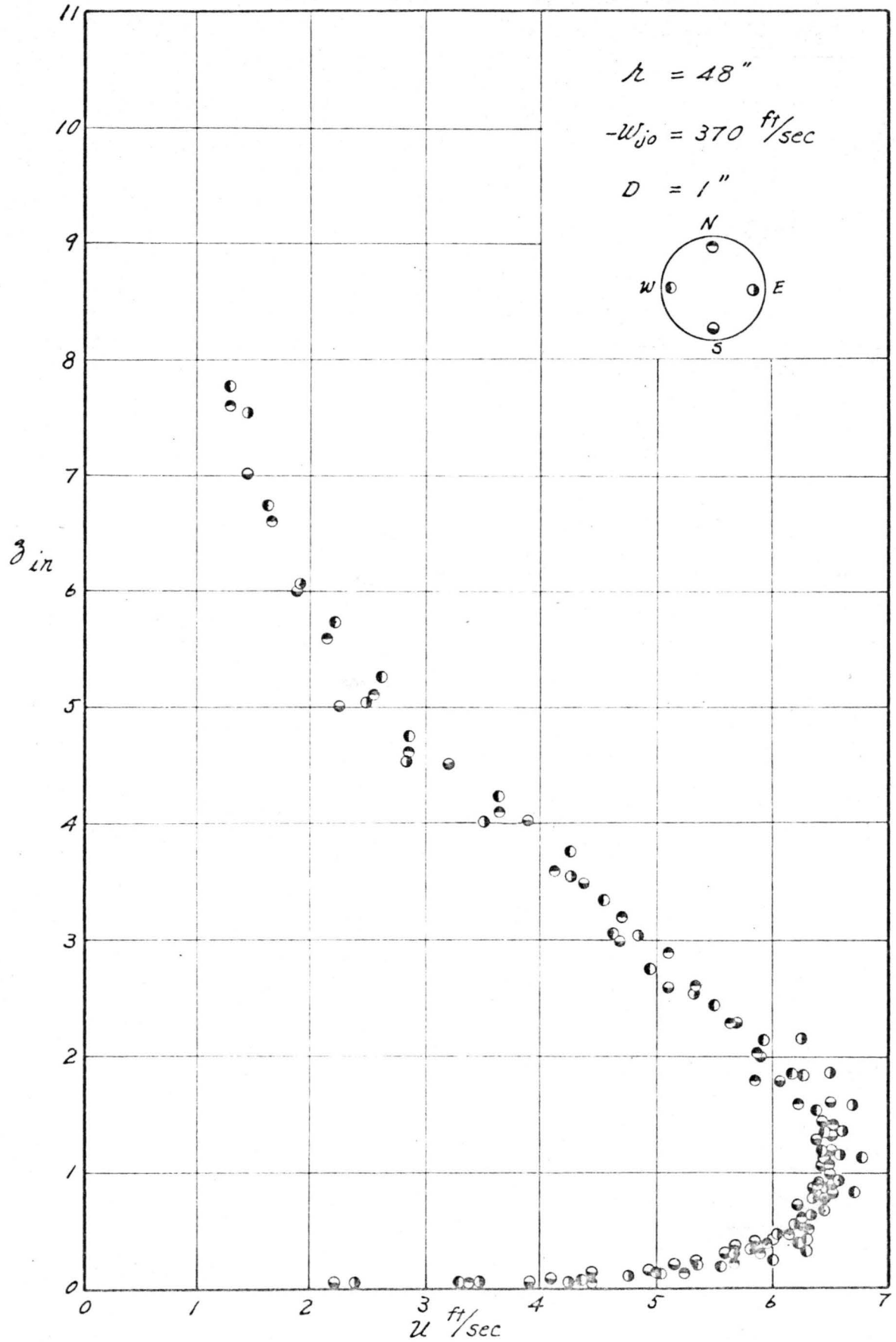

FIG. 7 CHECK ON SYMMETRY OF RADIAL WALL JET

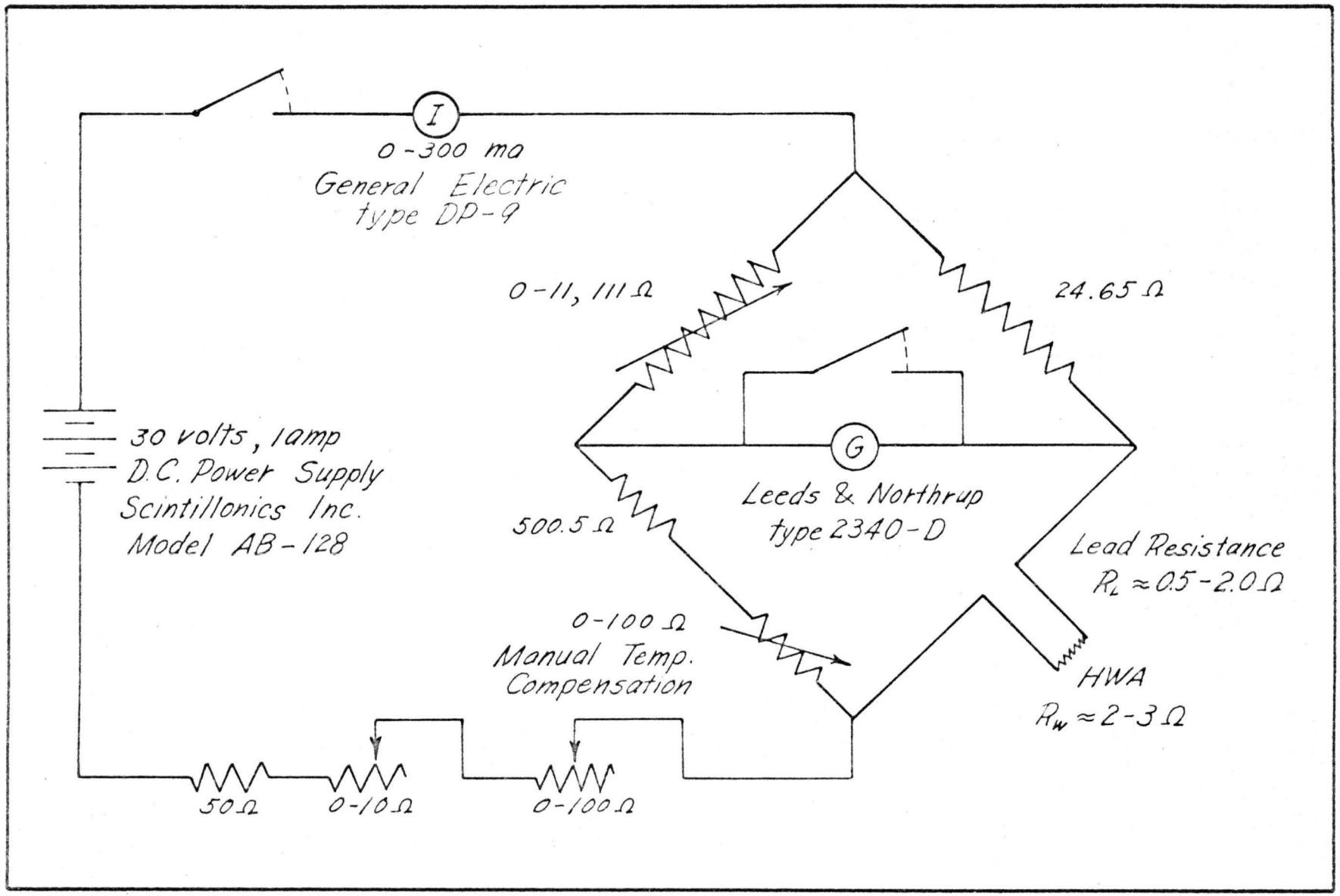

FIG. 8 CIRCUIT DIAGRAM FOR MEAN-VELOCITY HOT-WIRE BRIDGE

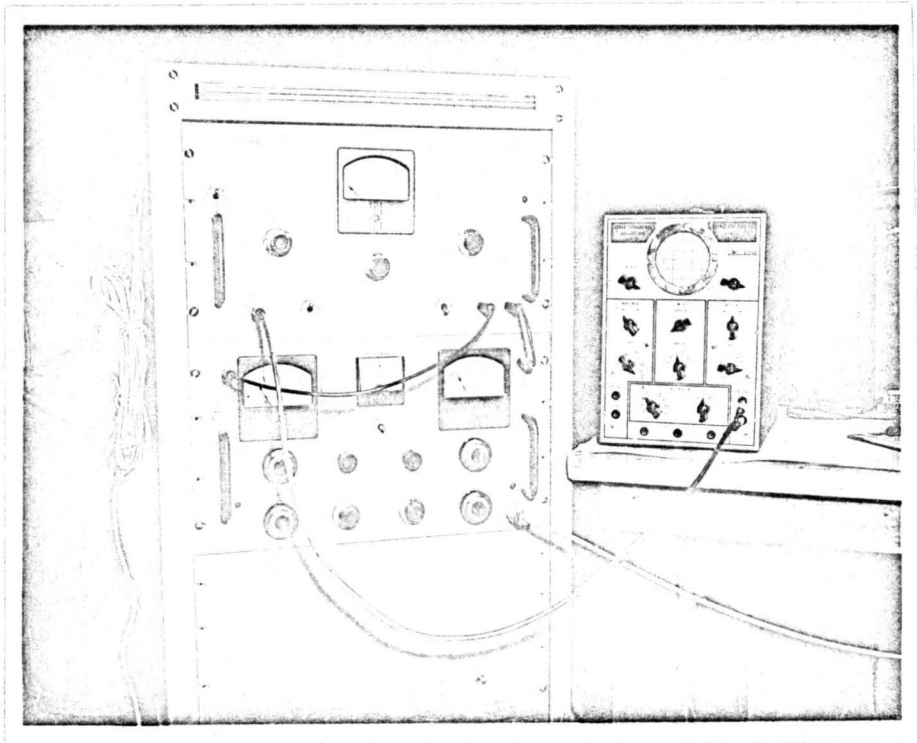

FIG. 9 INSTRUMENTS FOR MEASURING TURBULENT QUANTITIES

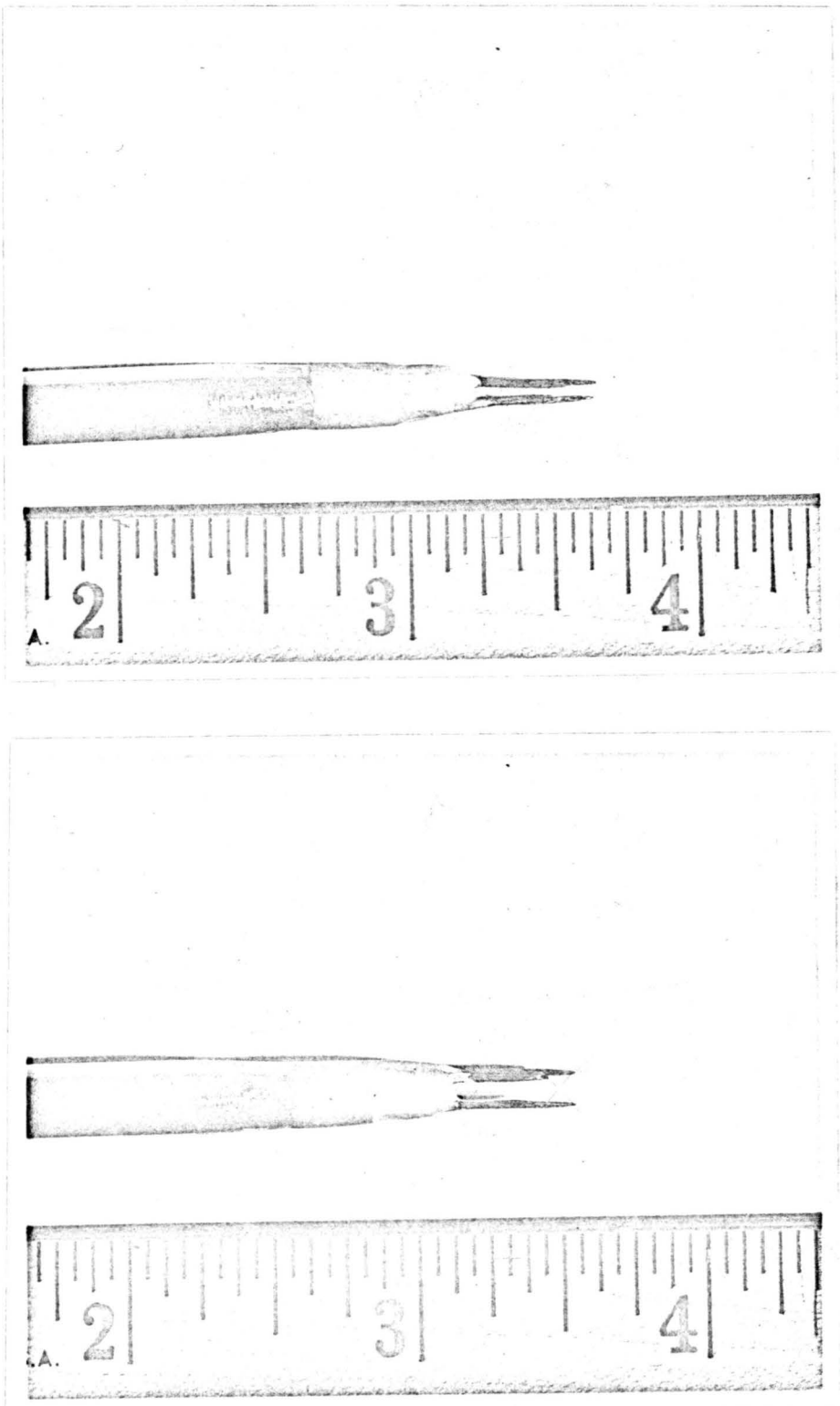

FIG. 10 VIEWS OF CROSS-WIRE PROBE

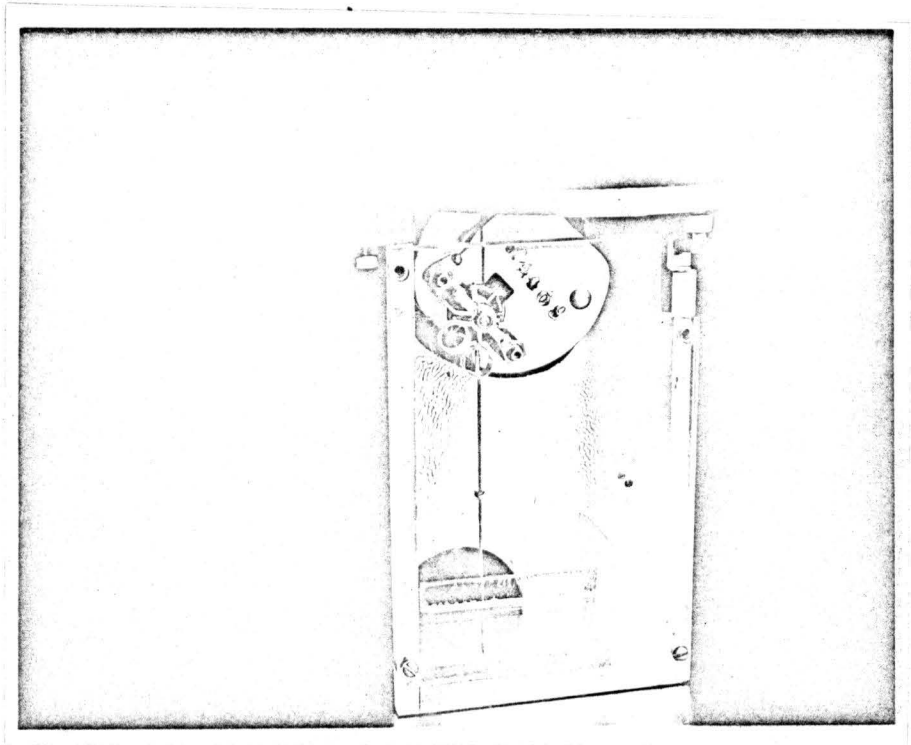

FIG. 11 SHEAR - METER : VIEW OF ASSEMBLY

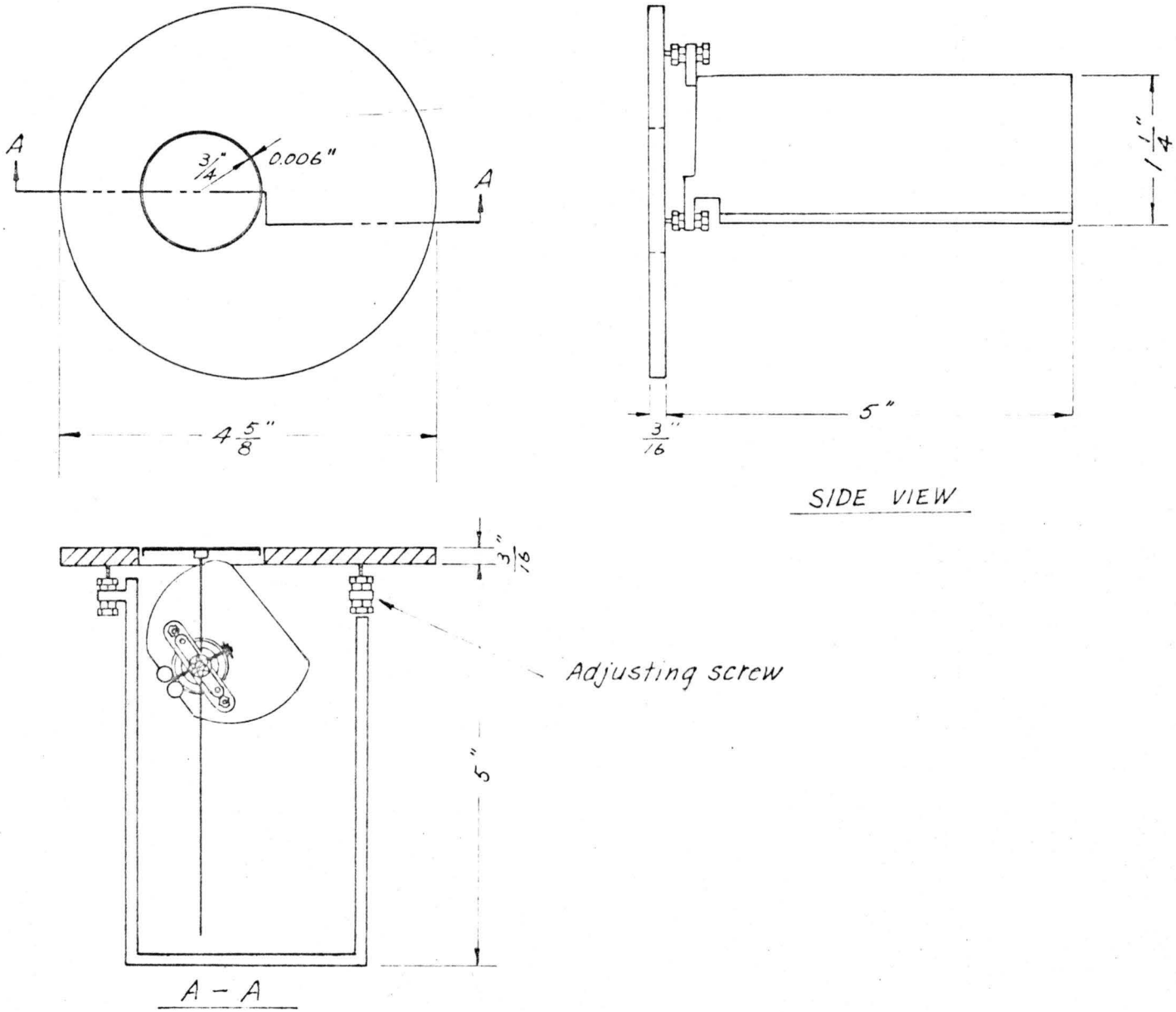

FIG. 12 SHEAR-METER : DETAILS

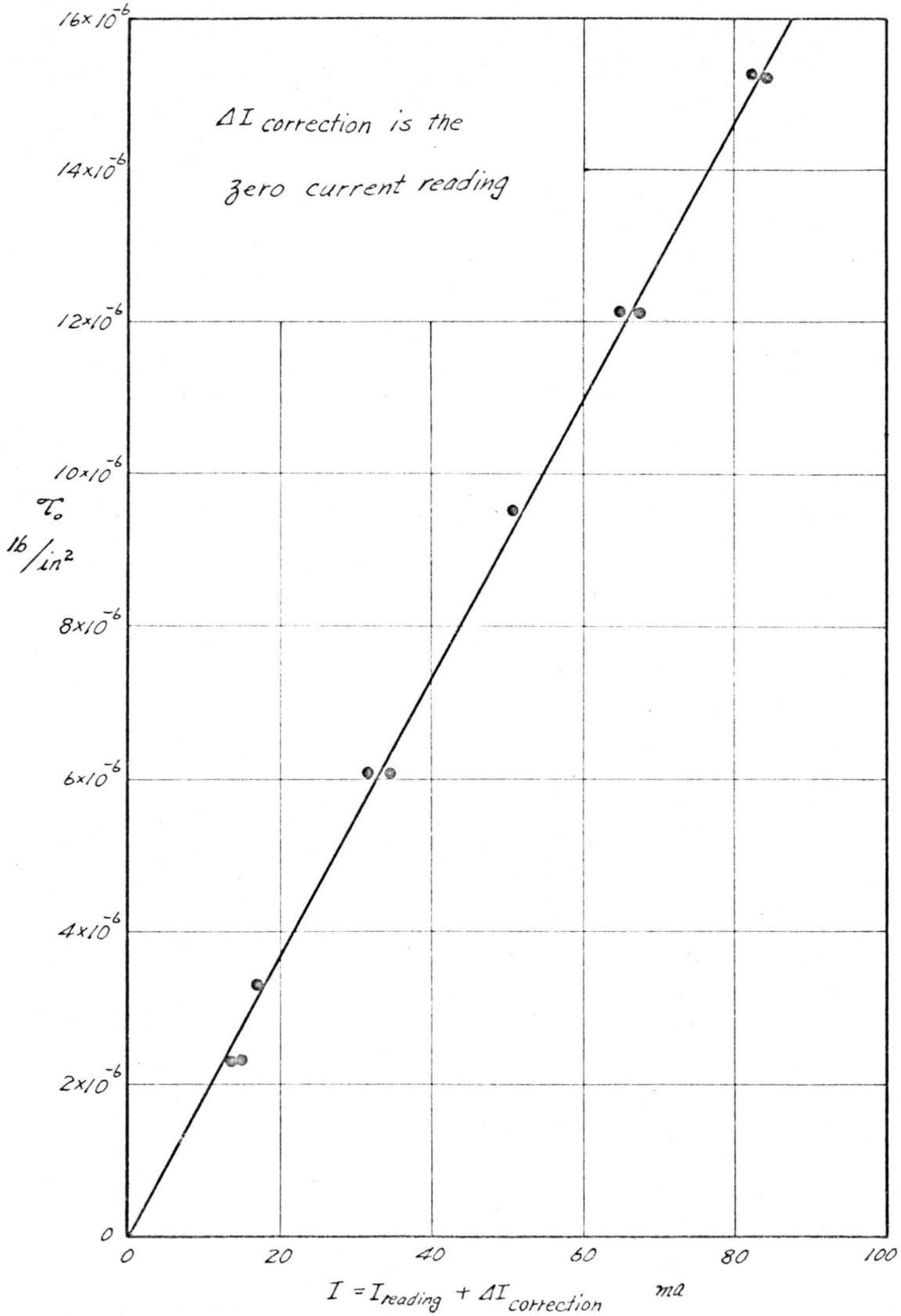

FIG. 13 STATIC CALIBRATION OF SHEAR-METER

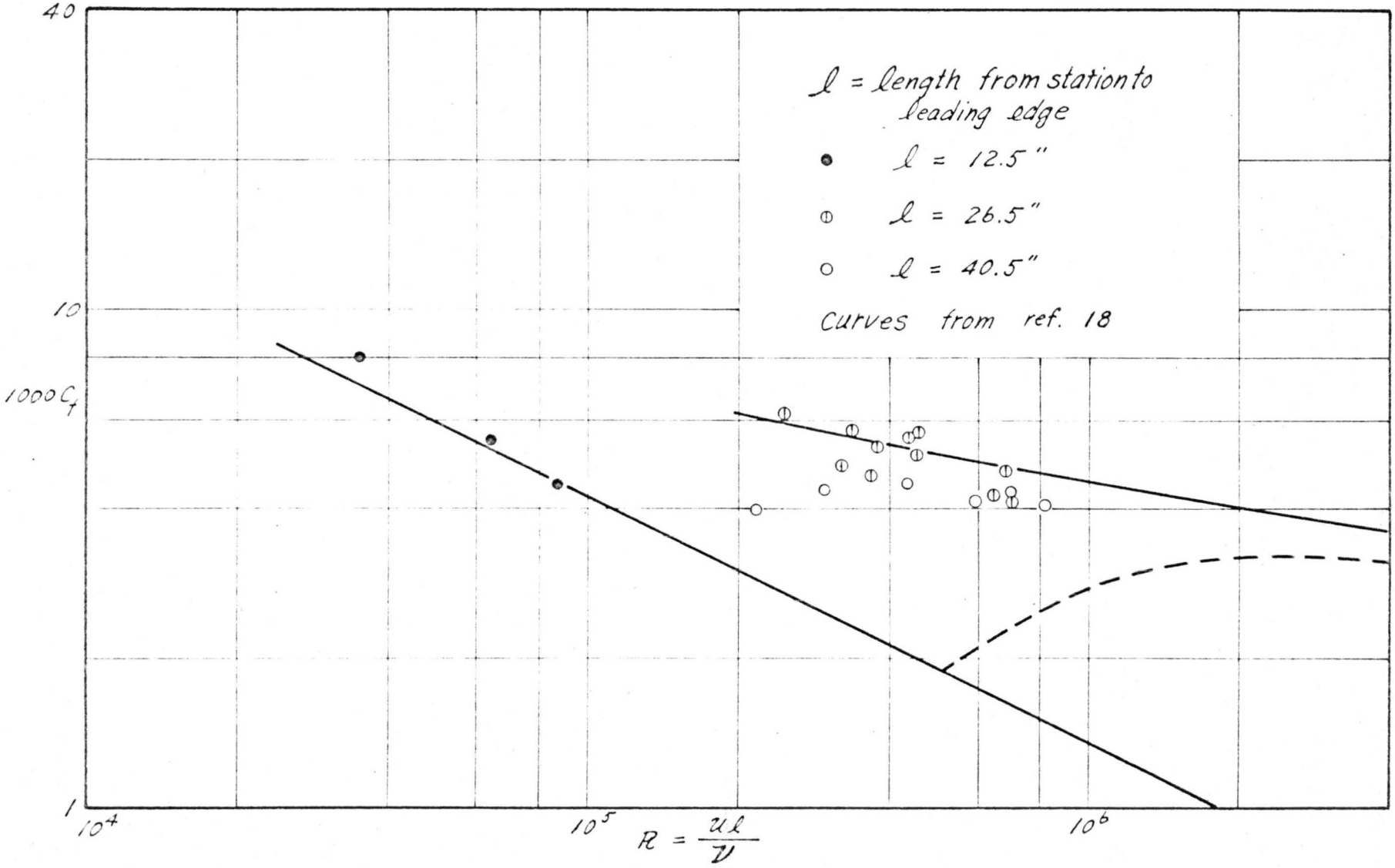

FIG. 14 DYNAMICAL CHECK OF SHEAR-METER ON SMOOTH FLAT PLATE

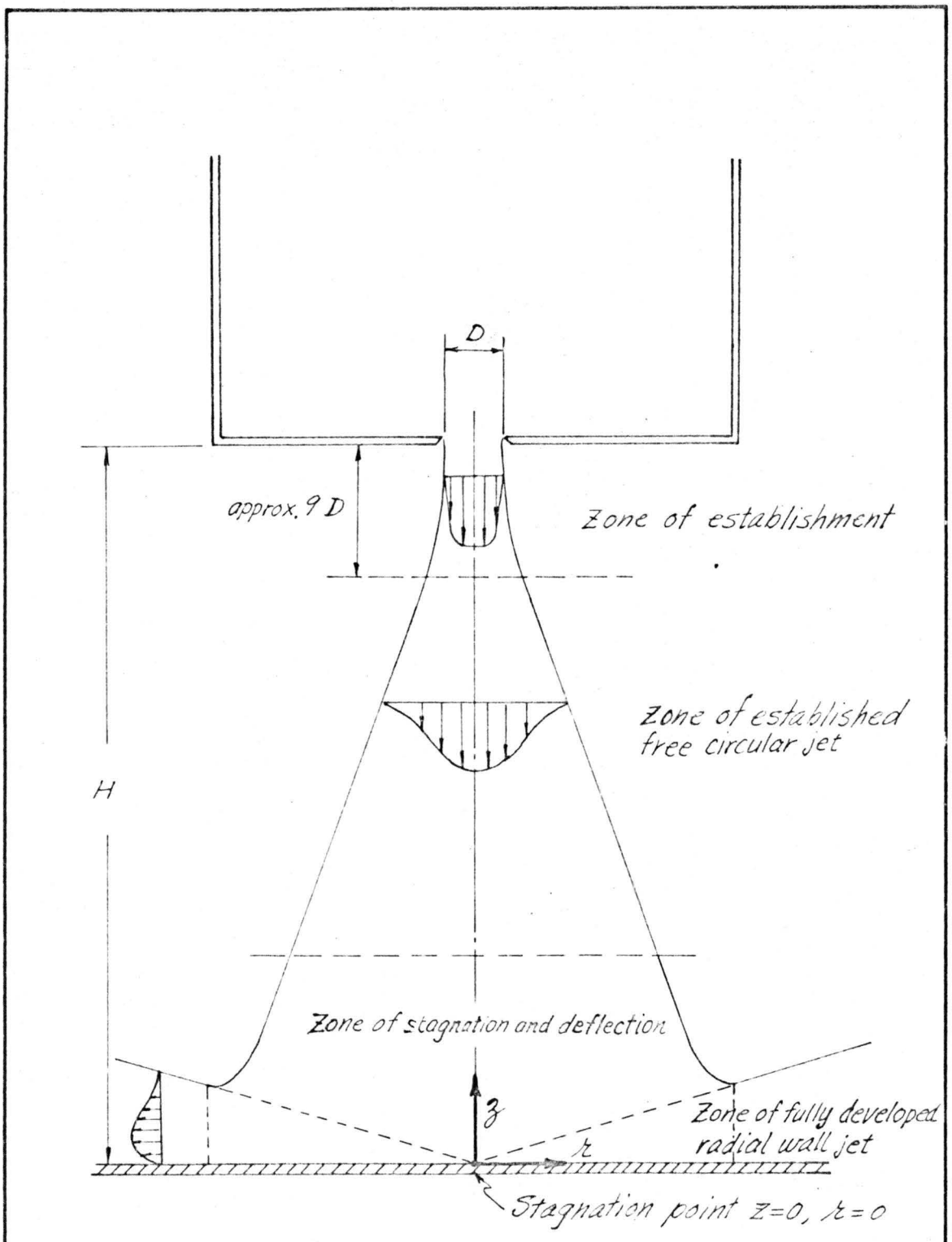

FIG. 15 ZONES OF DIFFUSION

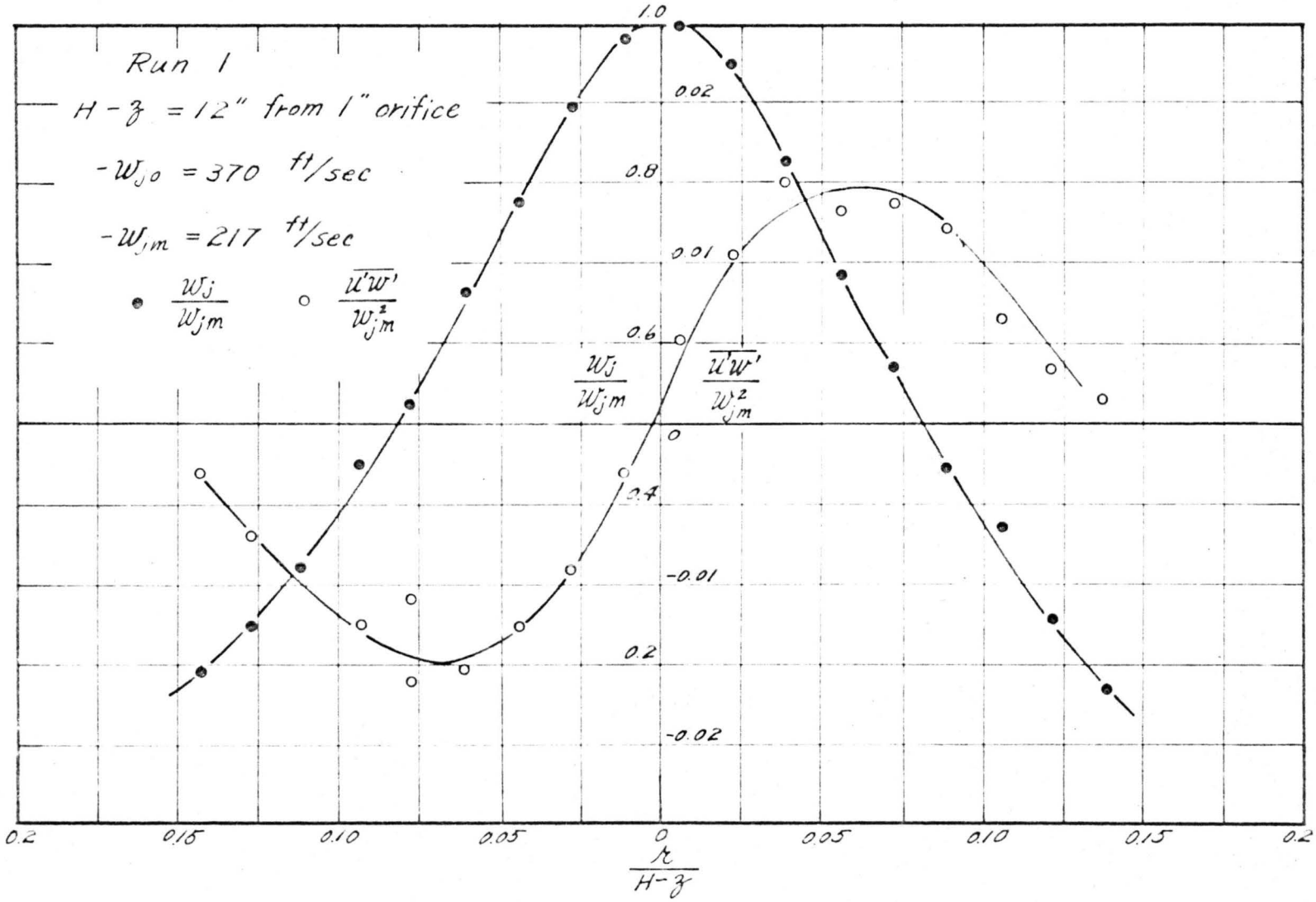

FIG. 16 MEAN VELOCITY PROFILE AND TURBULENT SHEAR STRESS DISTRIBUTION IN THE FREE CIRCULAR JET

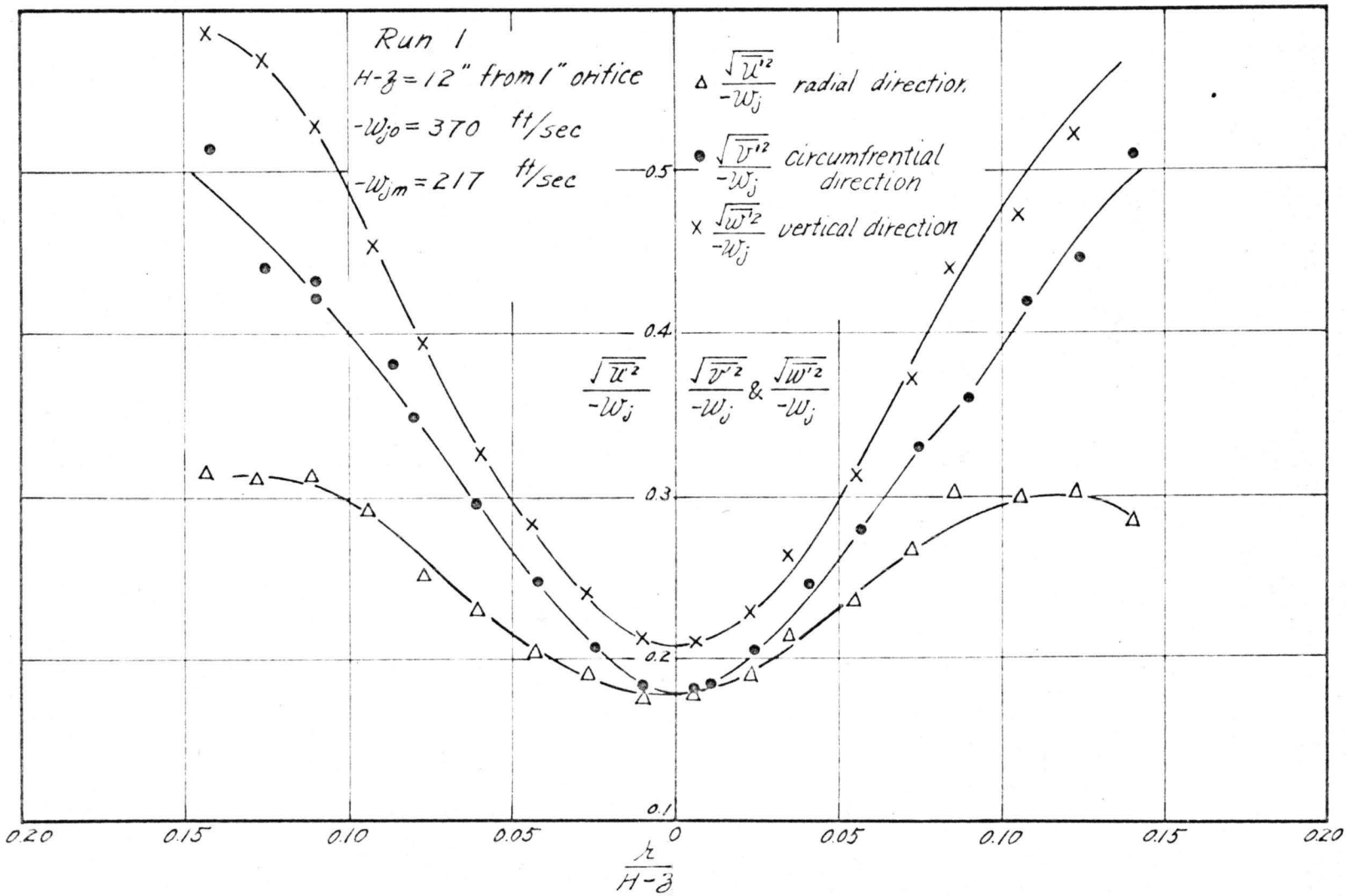

FIG. 17 DISTRIBUTION OF LOCAL RELATIVE TURBULENT INTENSITIES IN THE FREE CIRCULAR JET

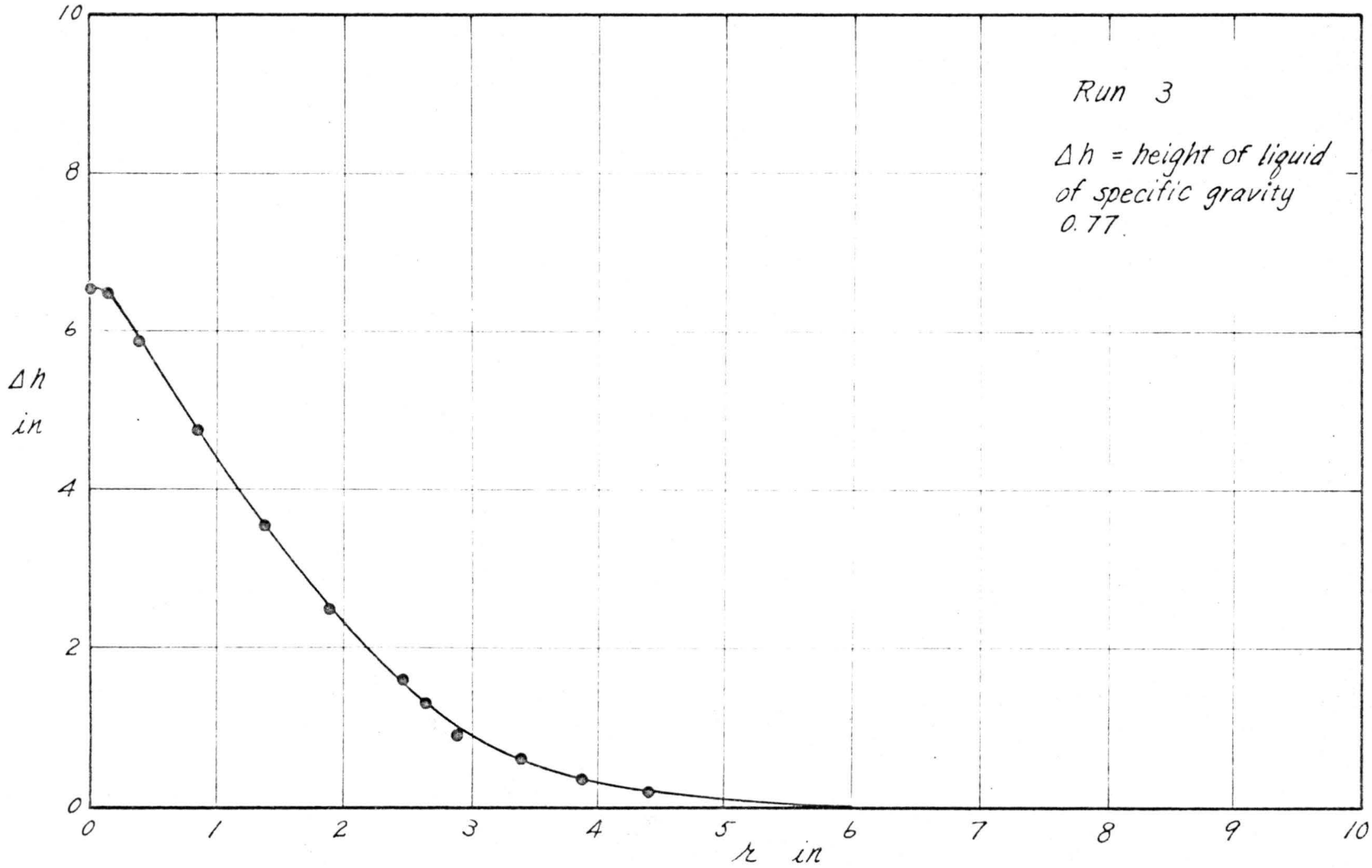

FIG. 18 STATIC WALL PRESSURE DISTRIBUTION IN THE STAGNATION REGION

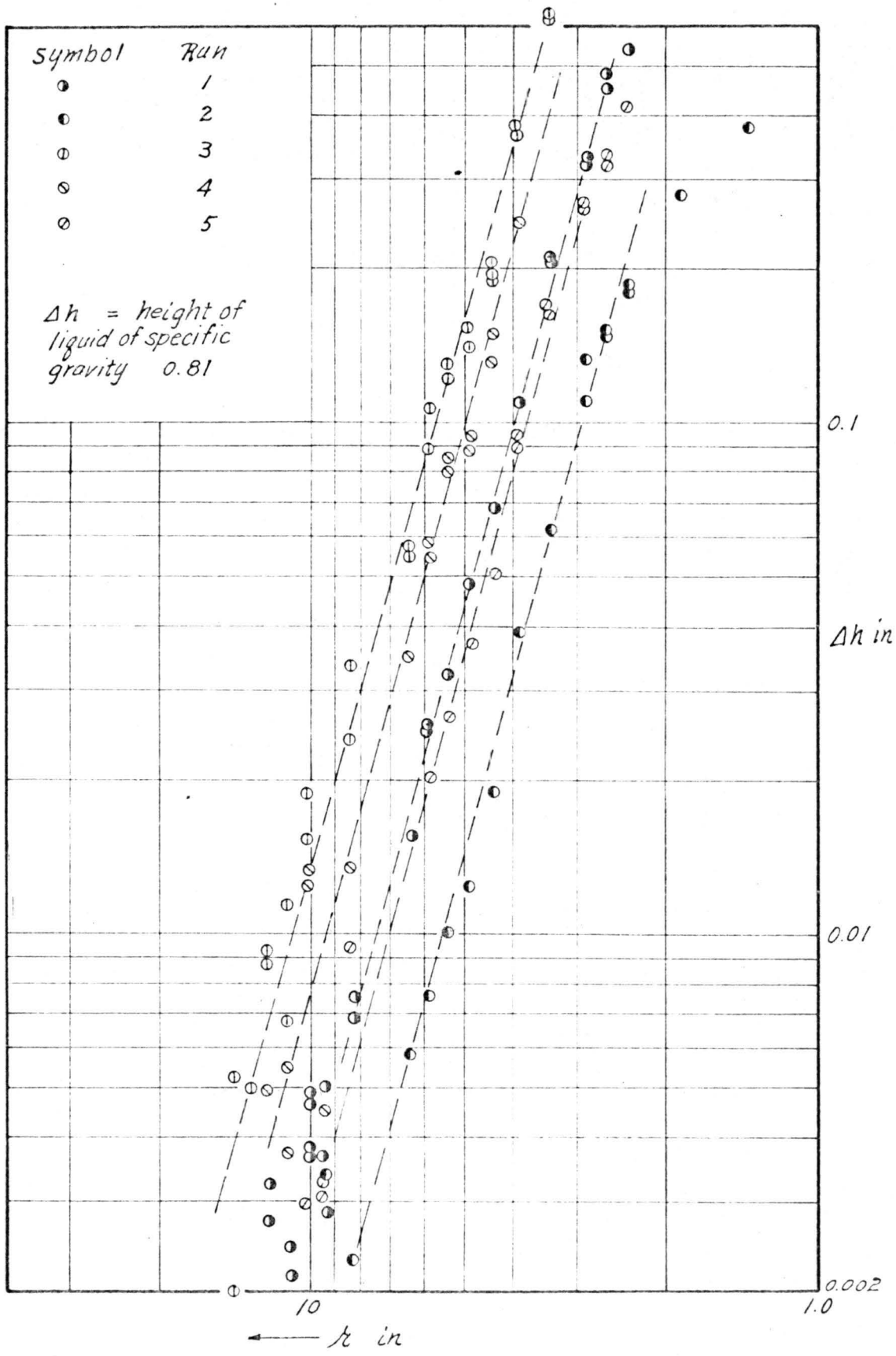

FIG. 19 PRESSURE DISTRIBUTION NEAR THE CENTRAL PORTION

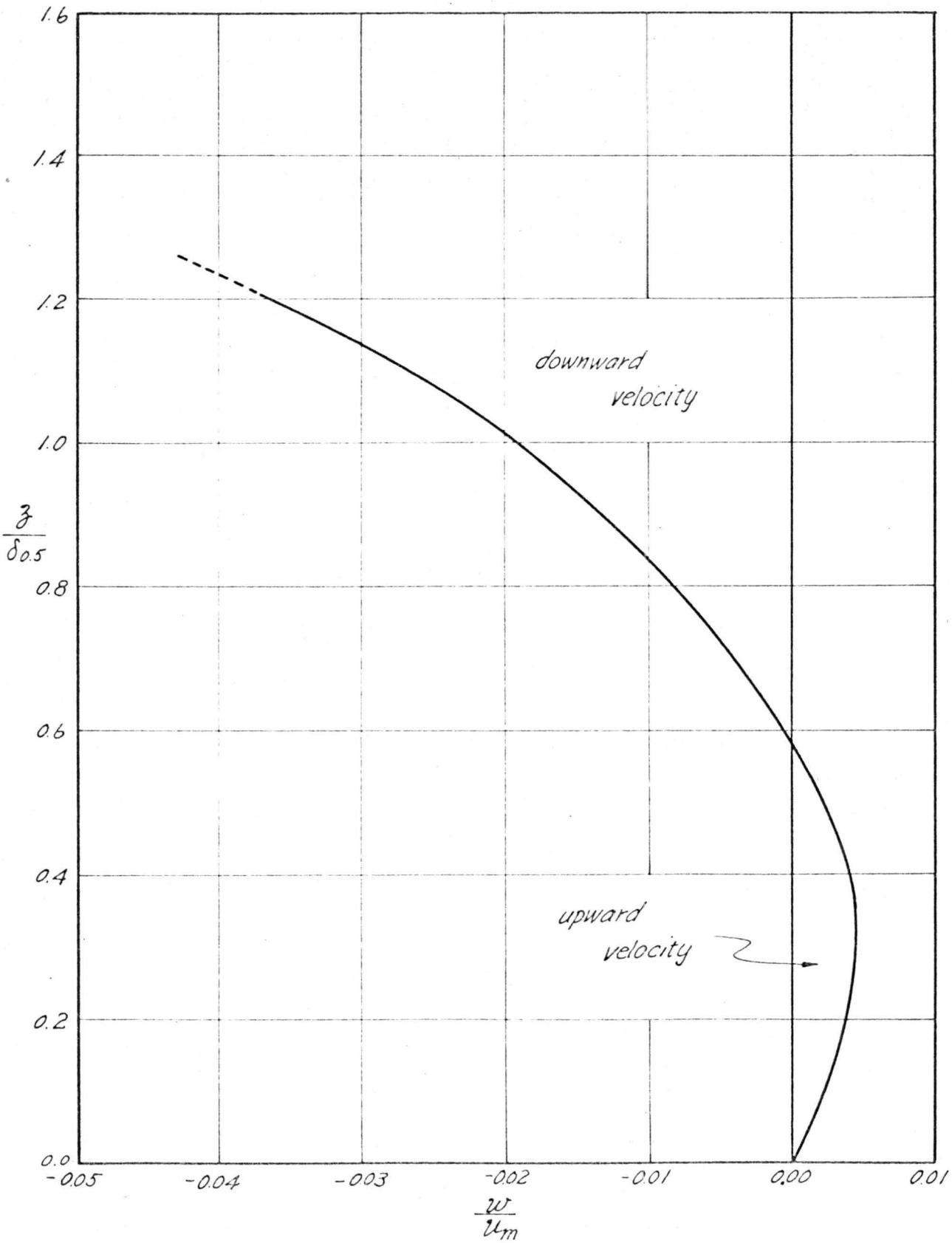

FIG. 20 DISTRIBUTION OF VERTICAL MEAN VELOCITY

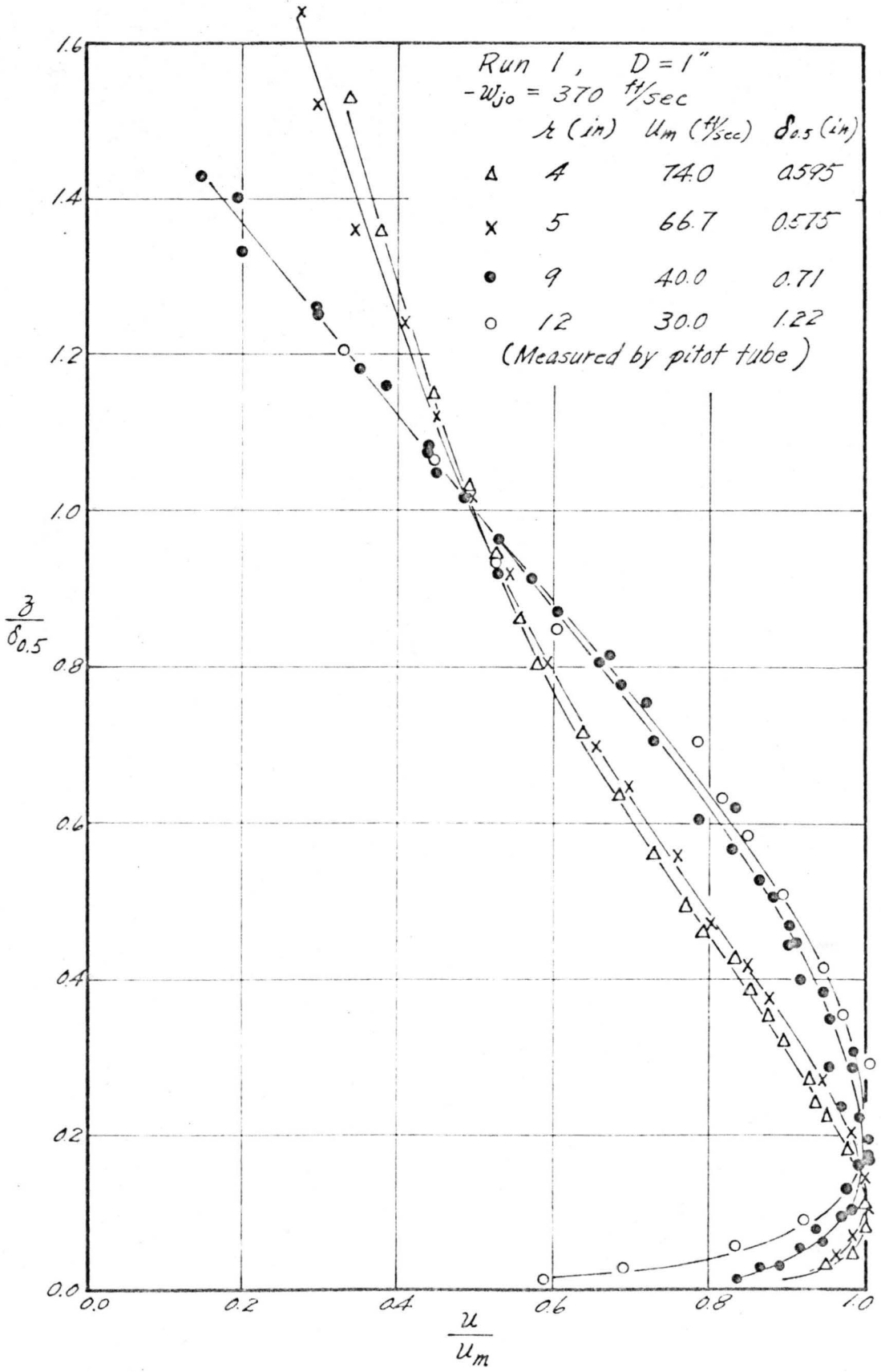

FIG. 21 APPROACH TO APPROXIMATE SIMILARITY CLOSE TO THE CENTRAL PORTION

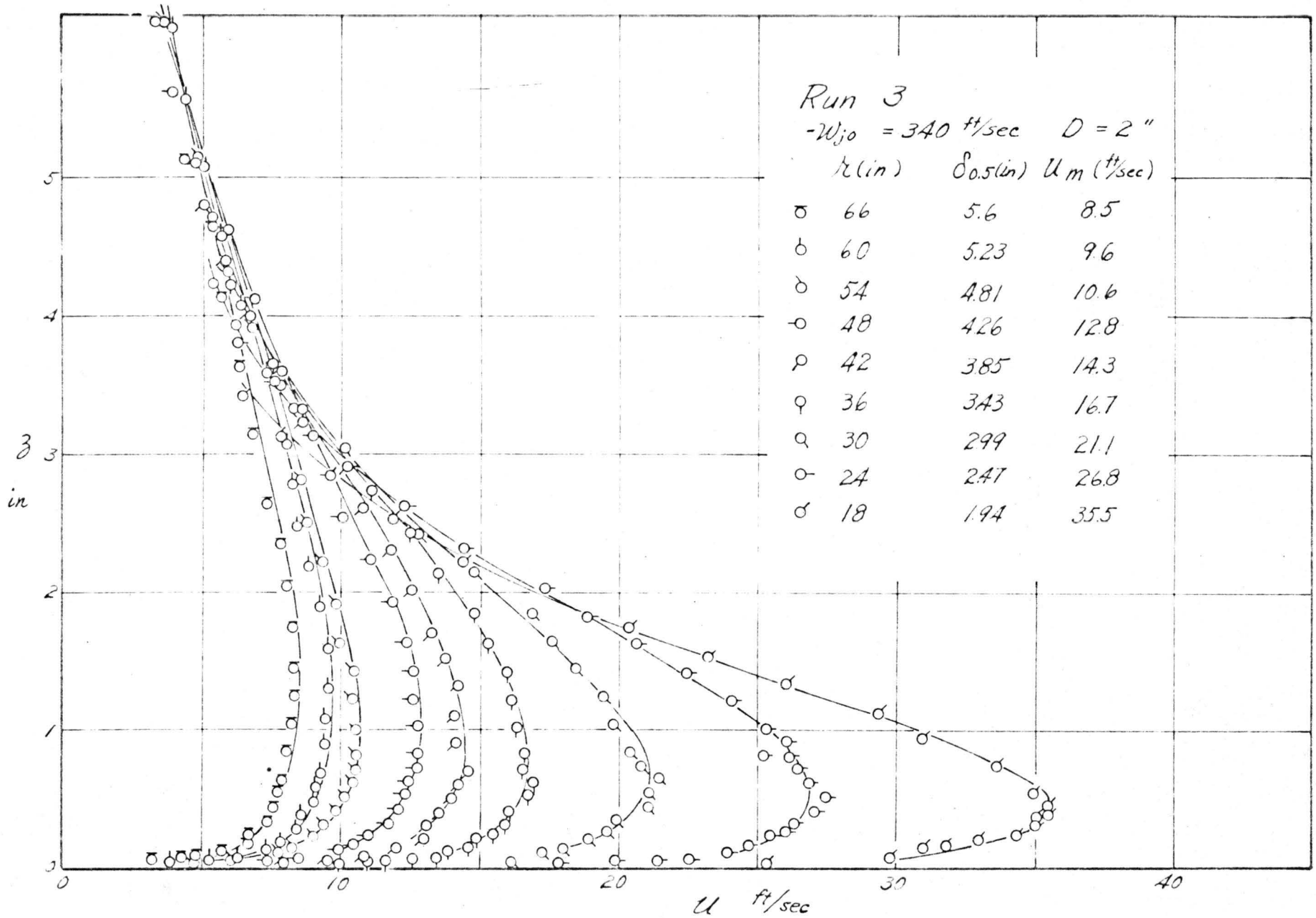

FIG. 22 DISTRIBUTION OF MEAN VELOCITY IN DIMENSIONAL FORM: RUN 3

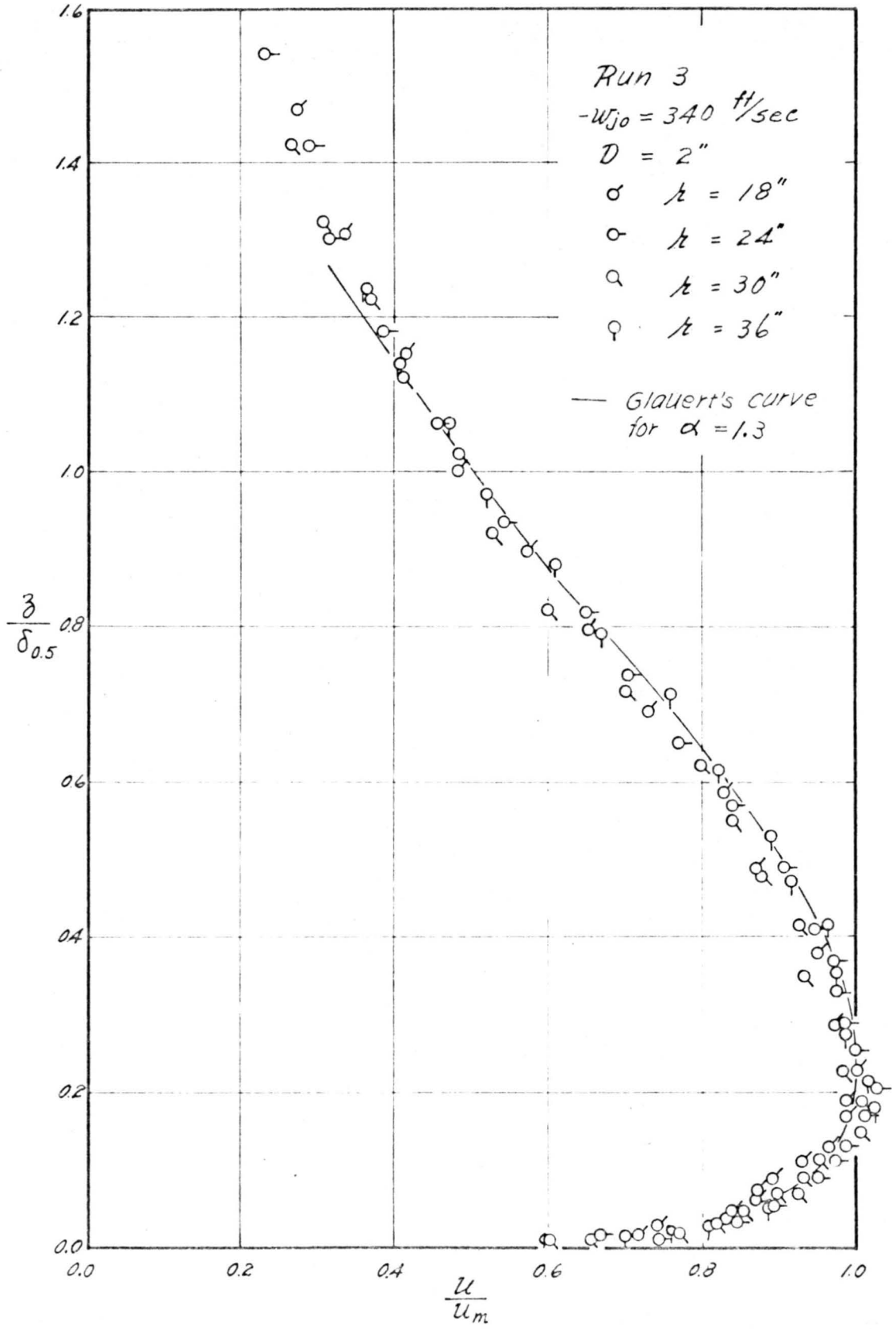

FIG. 23 DISTRIBUTION OF MEAN VELOCITY
RUN 3 STATIONS 18" TO 36"

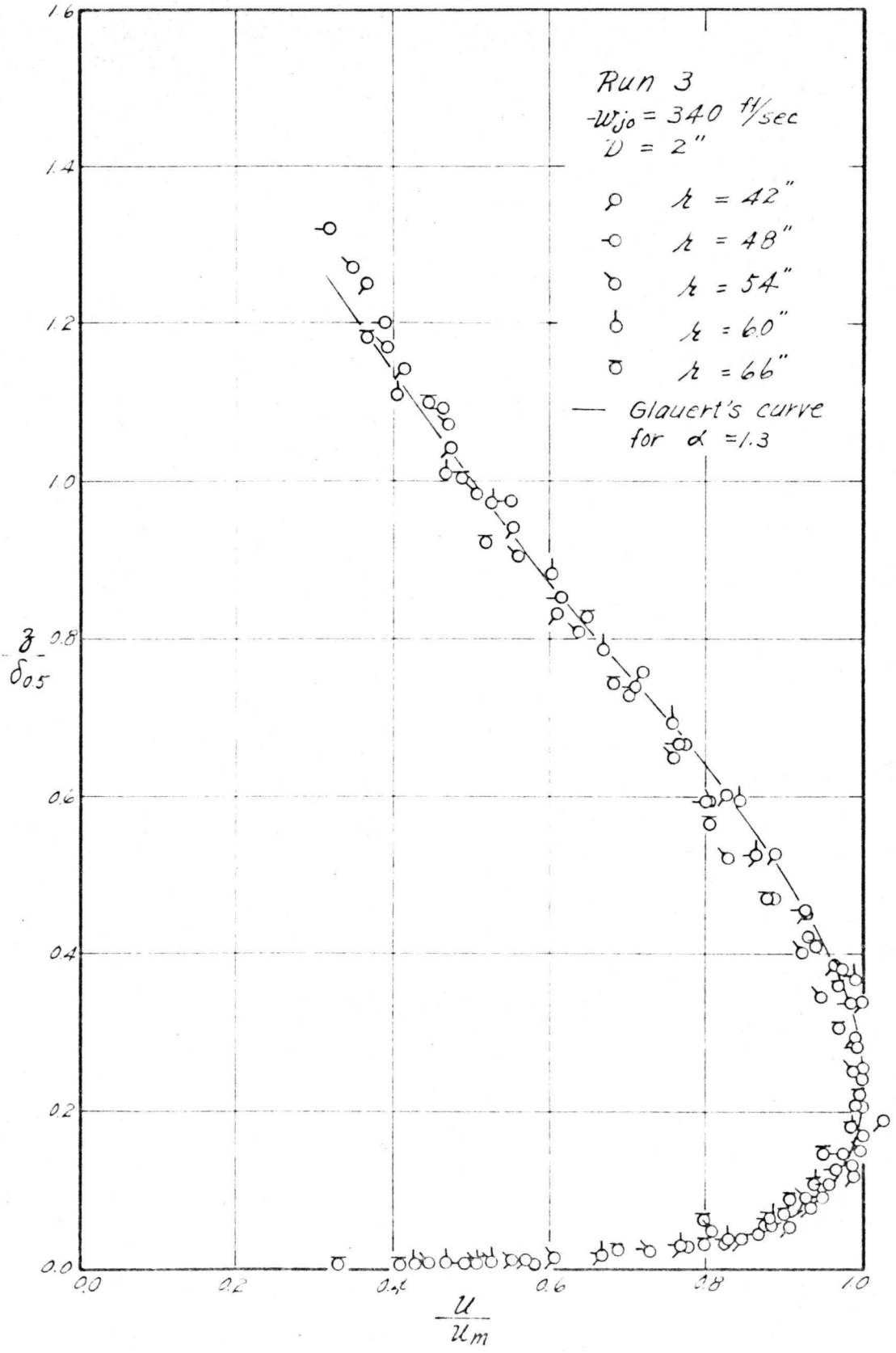

FIG. 24 DISTRIBUTION OF MEAN VELOCITY RUN 3 STATIONS 42" TO 66"

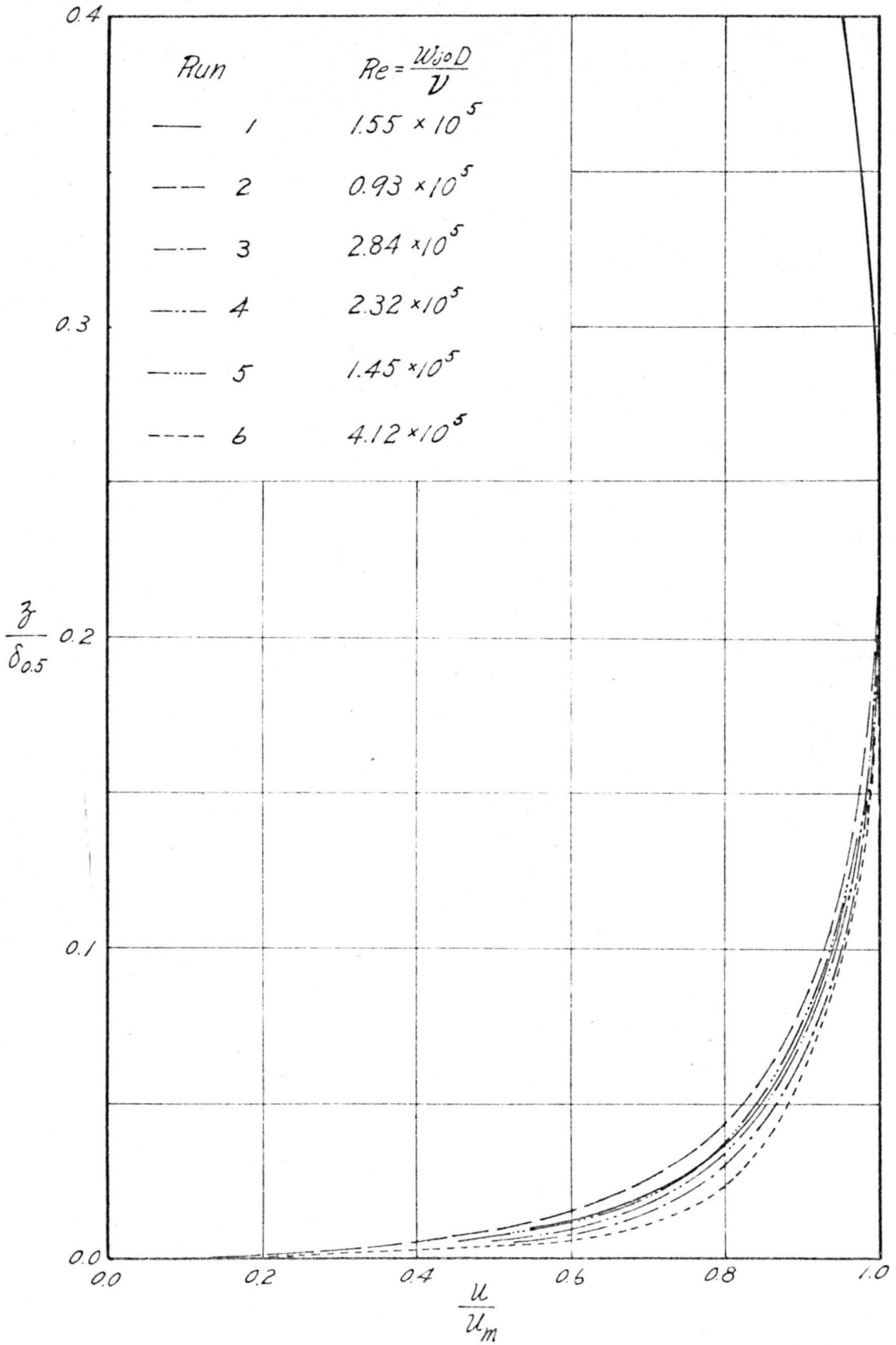

FIG. 24 a VARIATION OF INNER BOUNDARY-LAYER MEAN VELOCITY PROFILE WITH RESPECT TO REYNOLDS NUMBER

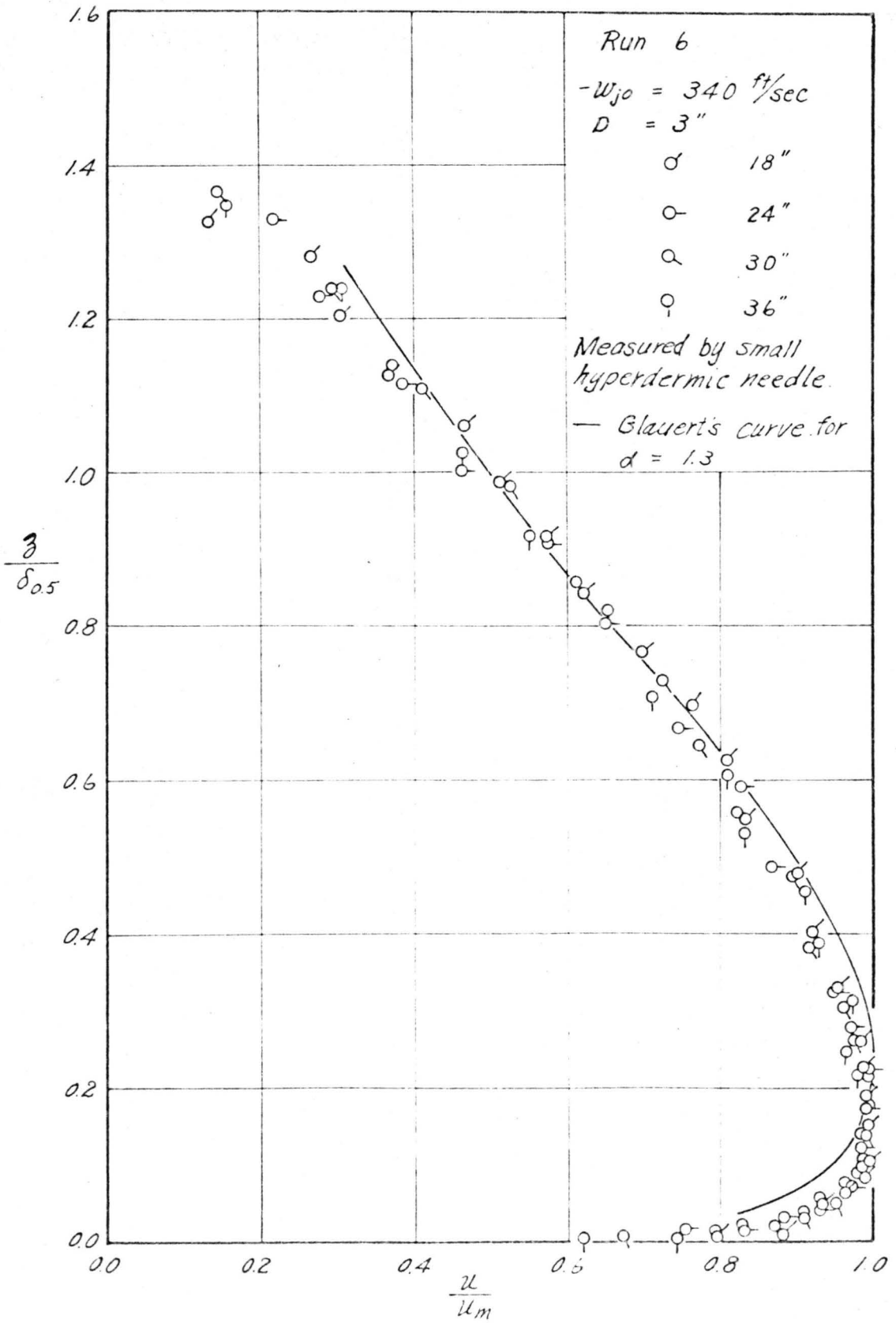

FIG. 25 DISTRIBUTION OF MEAN VELOCITY
RUN 6 STATIONS 18" TO 36"

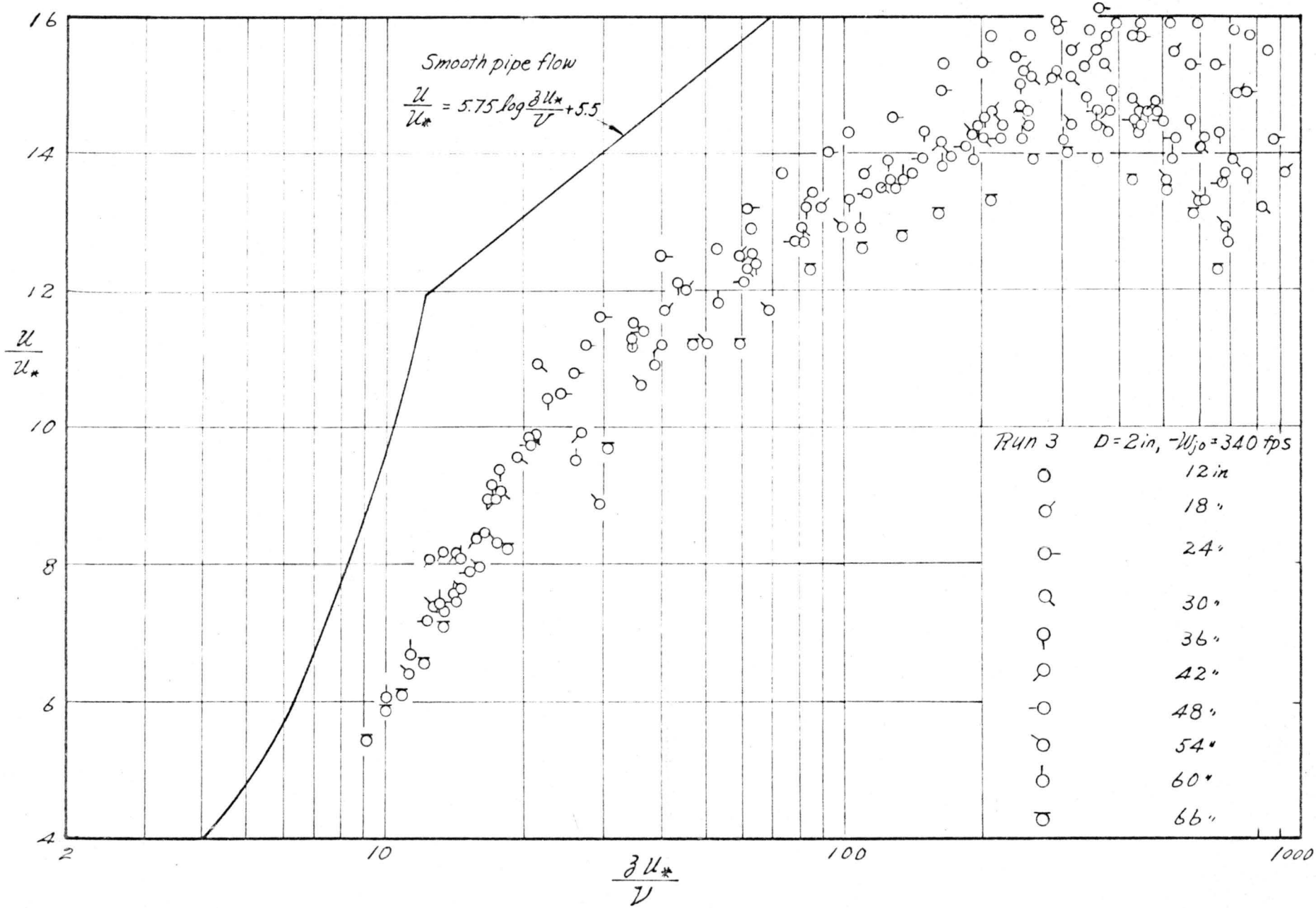

FIG. 26 INNER DISTRIBUTION OF MEAN VELOCITY

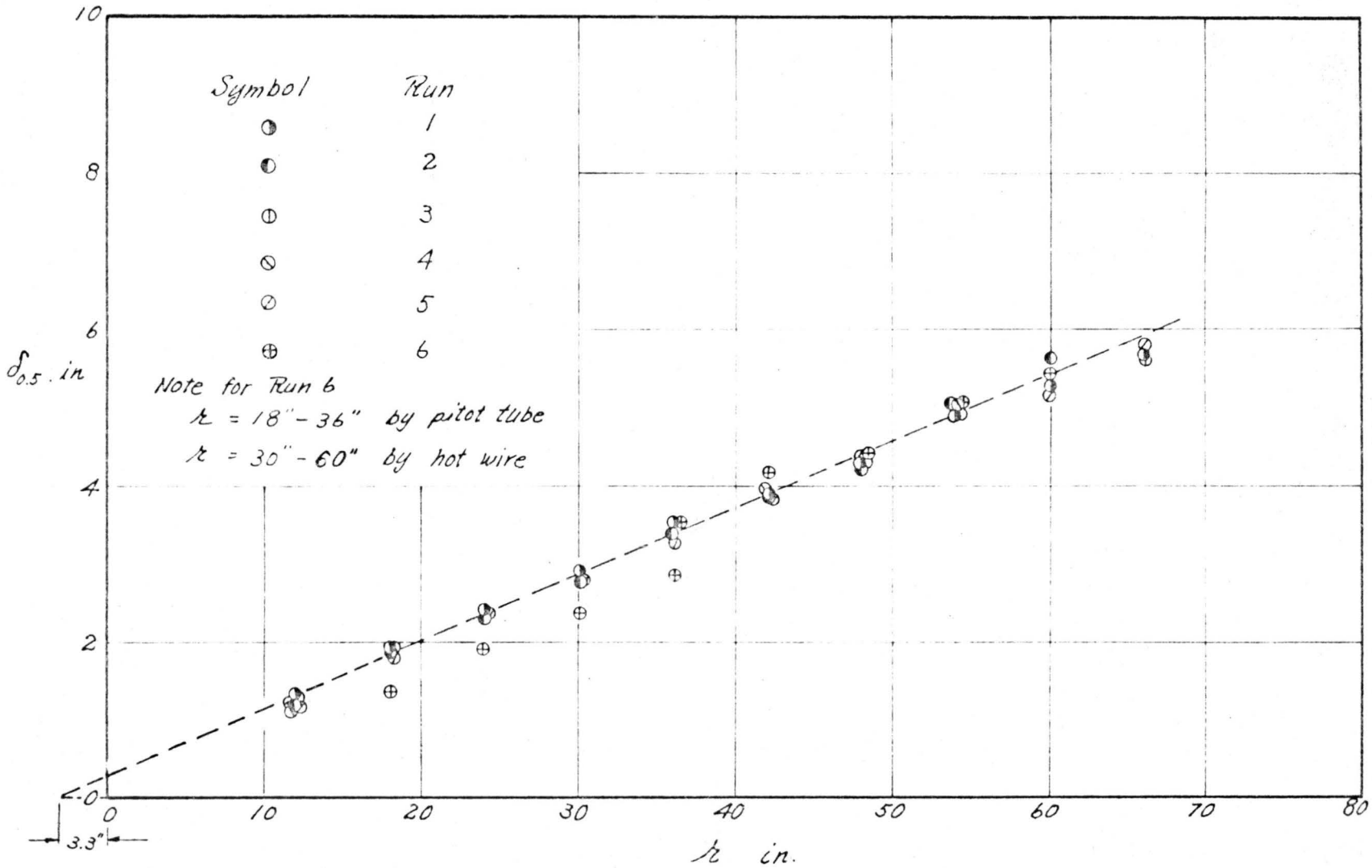

FIG. 27 GROWTH OF TURBULENT BOUNDARY-LAYER THICKNESS

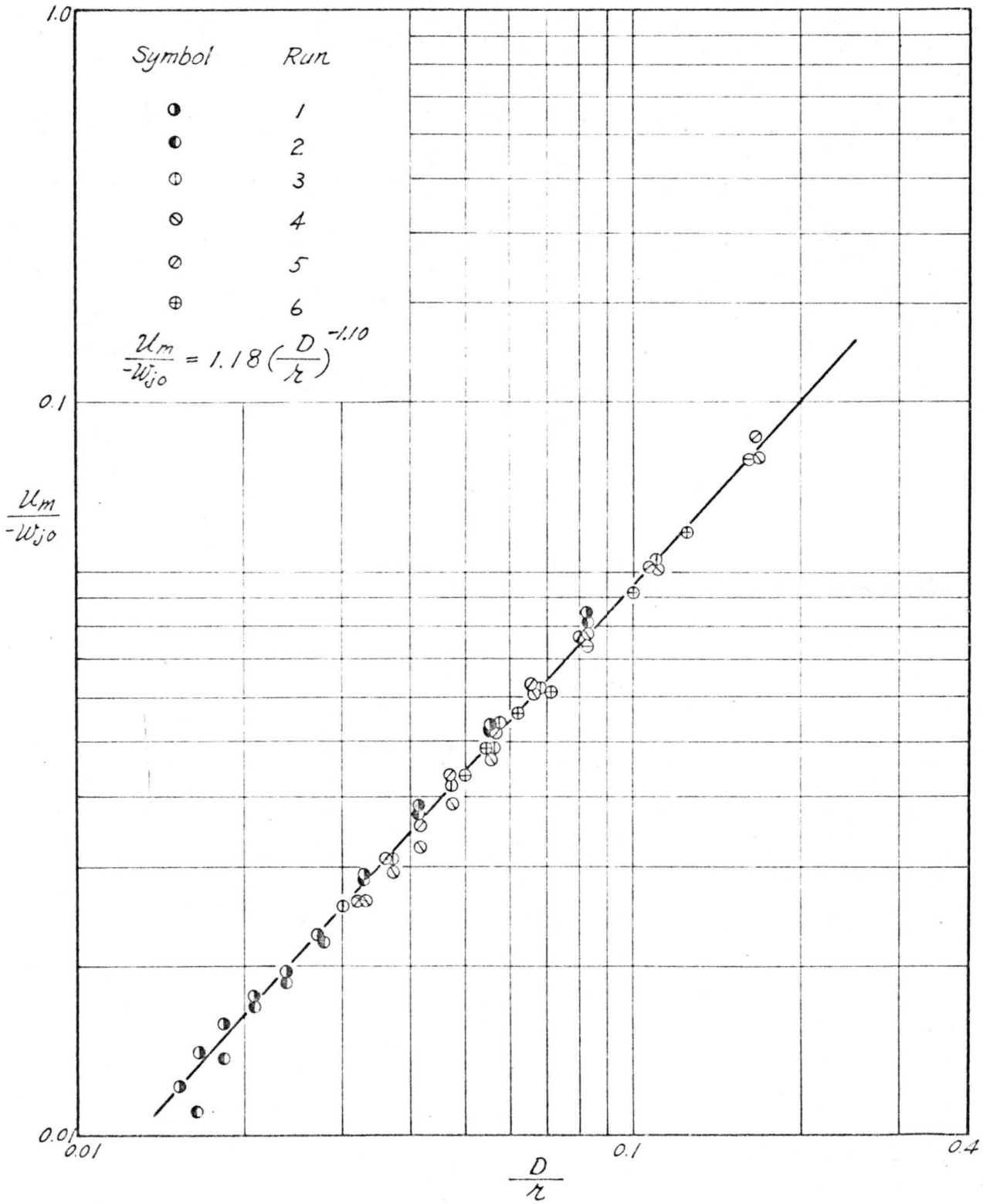

FIG. 28 DECAY OF PEAK VELOCITY u_m WITH RESPECT TO r

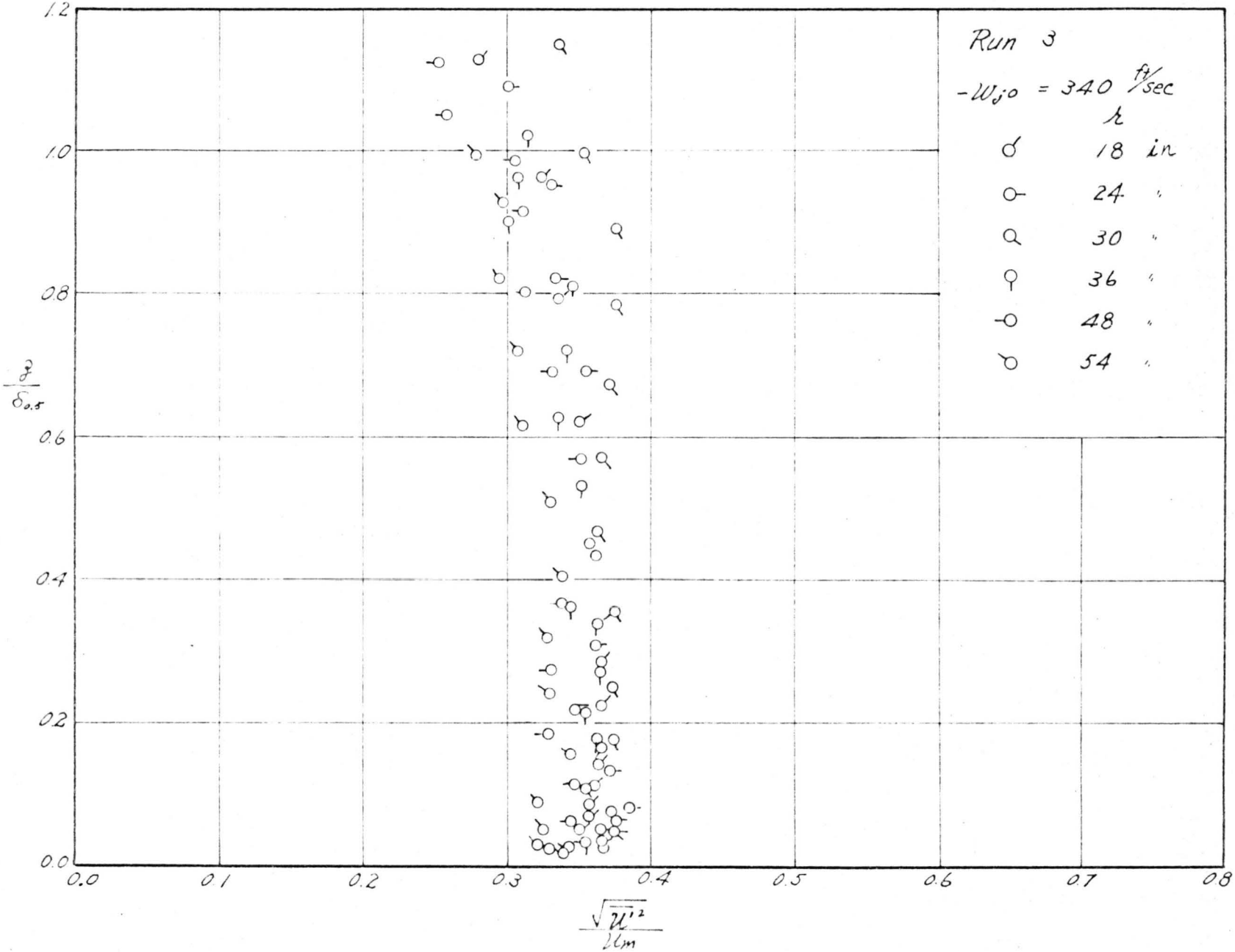

FIG. 29 DISTRIBUTION OF RADIAL TURBULENT INTENSITY

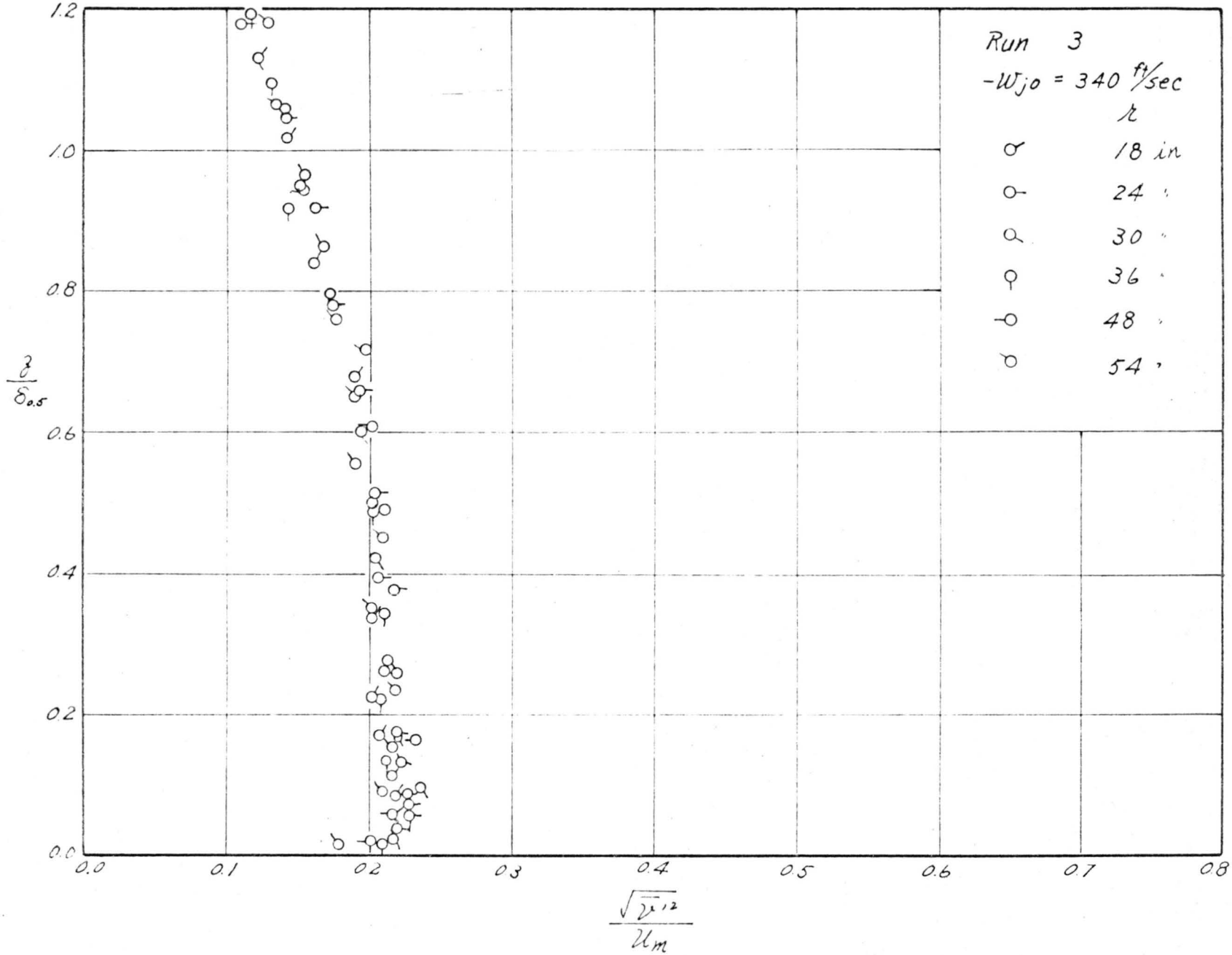

FIG. 30 DISTRIBUTION OF CIRCUMFERENTIAL TURBULENT INTENSITY

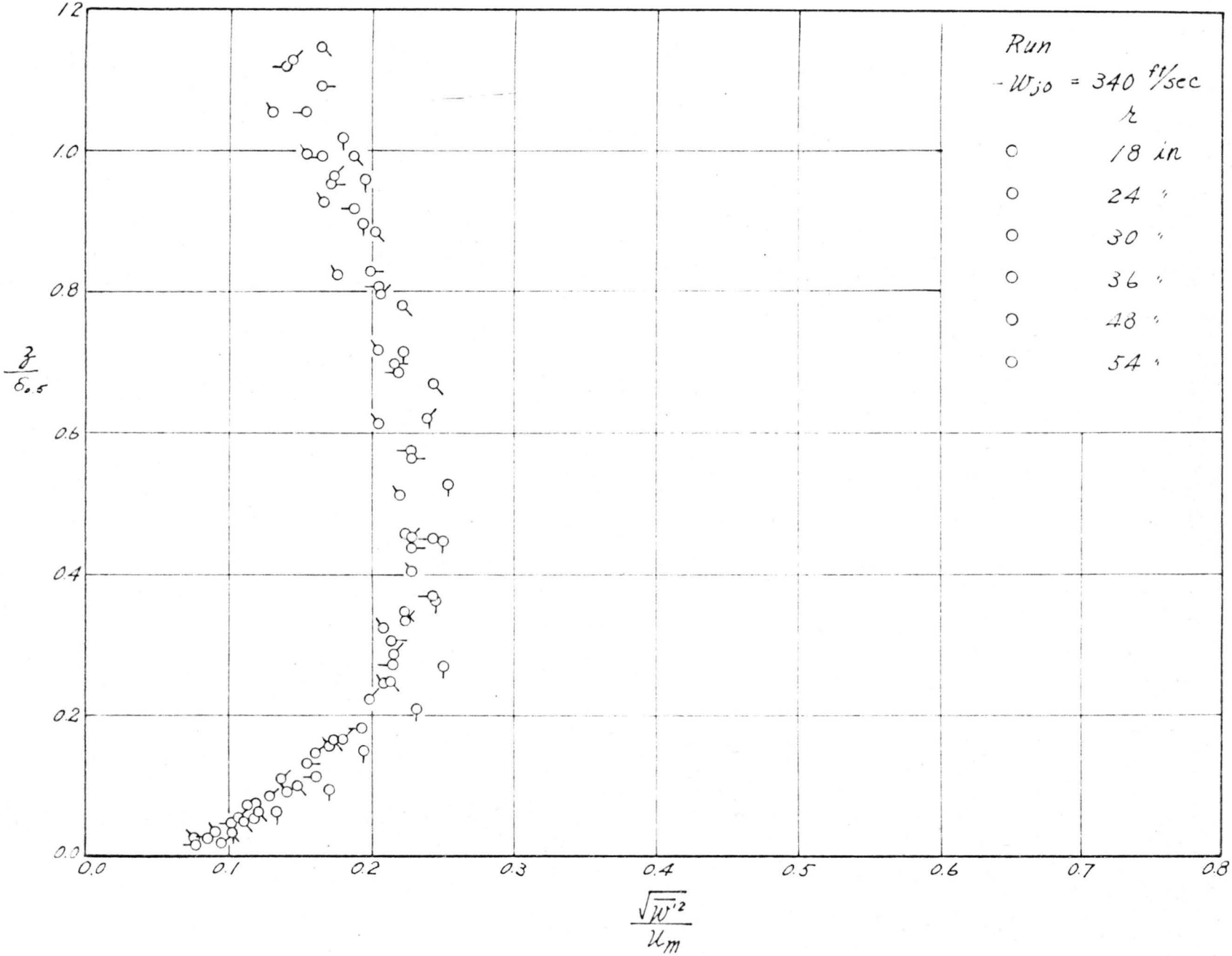

FIG. 31 DISTRIBUTION OF VERTICAL TURBULENT INTENSITY

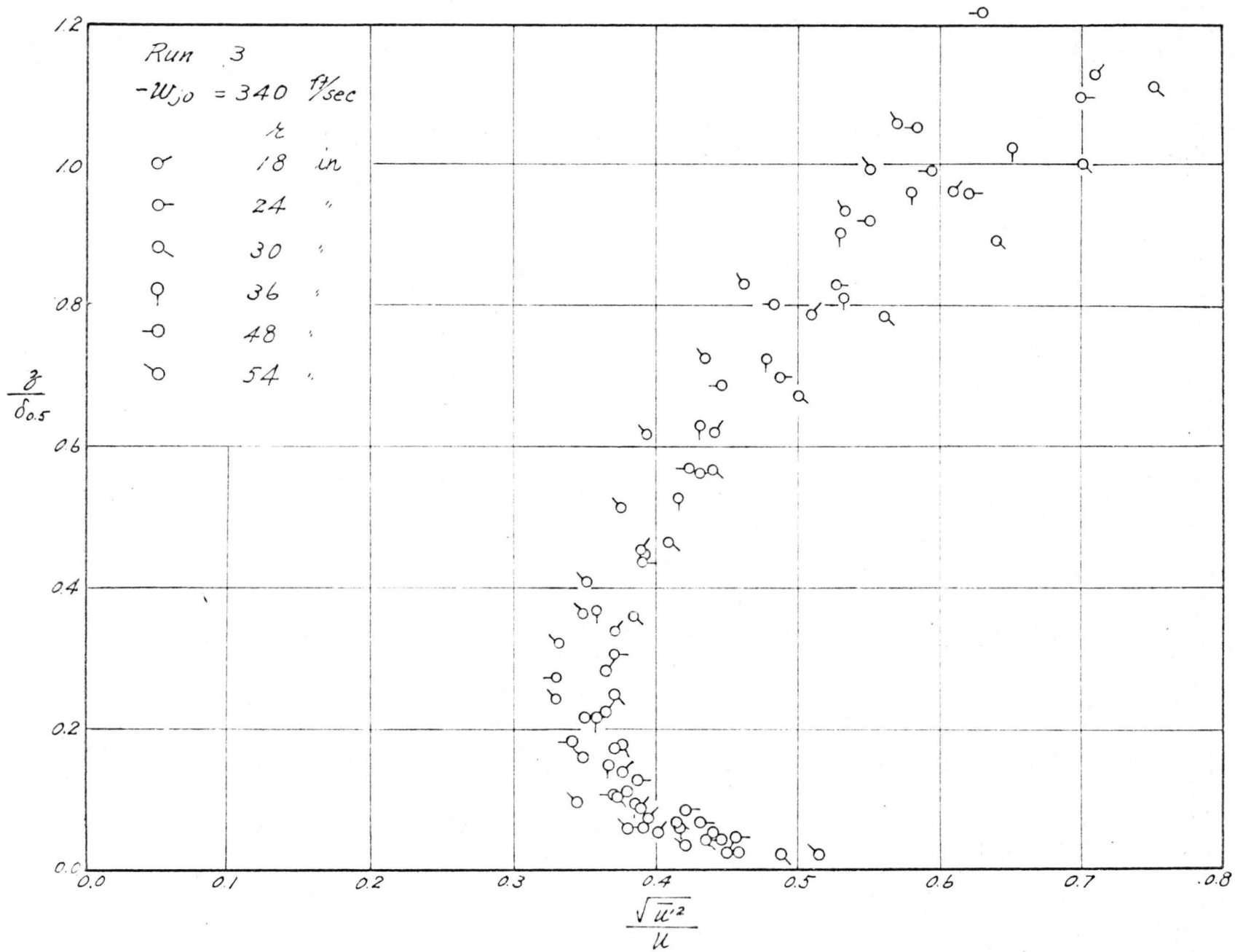

FIG. 32 DISTRIBUTION OF LOCAL RADIAL INTENSITY OF TURBULENCE

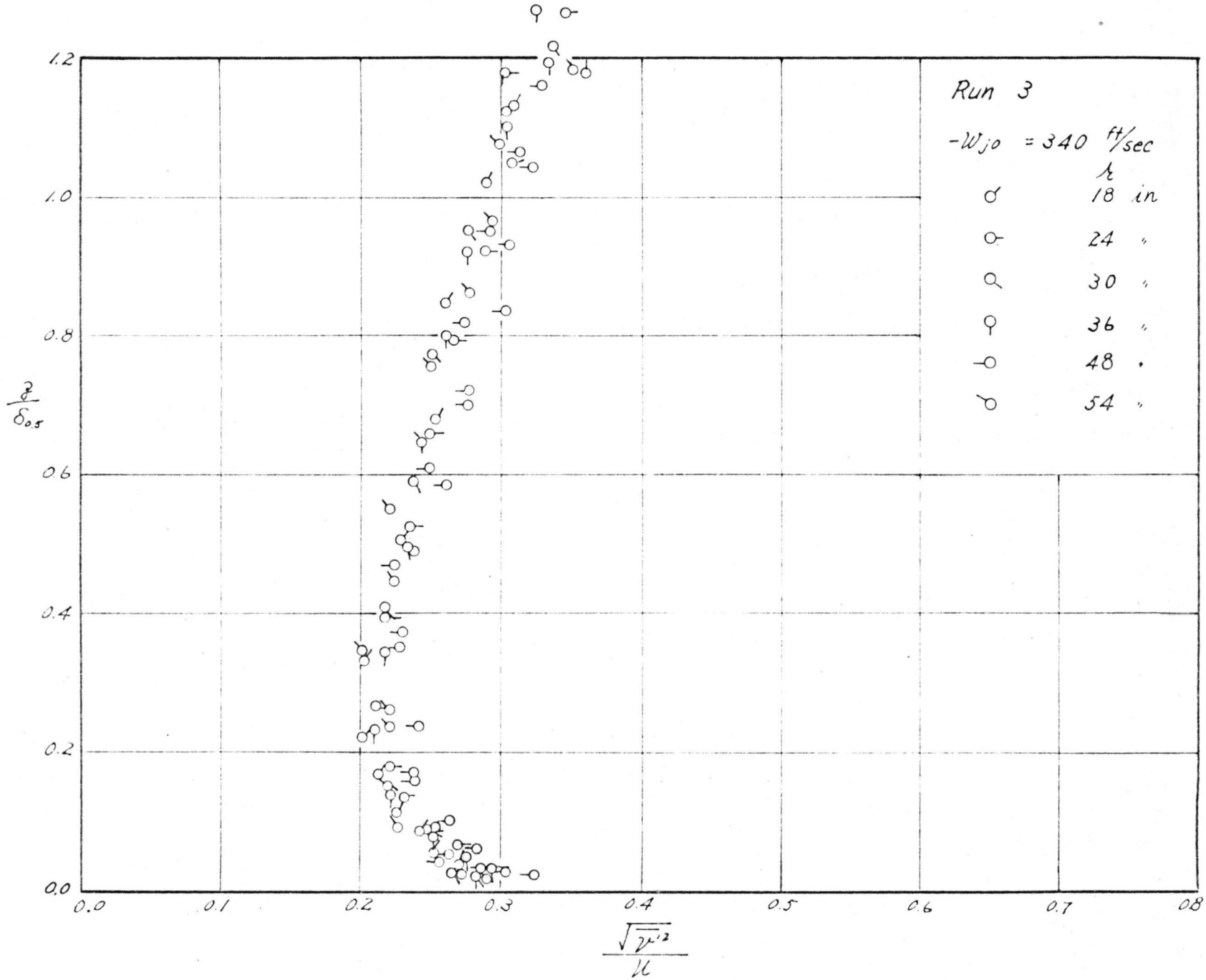

FIG. 33 DISTRIBUTION OF LOCAL CIRCUMFERENTIAL INTENSITY OF TURBULENT

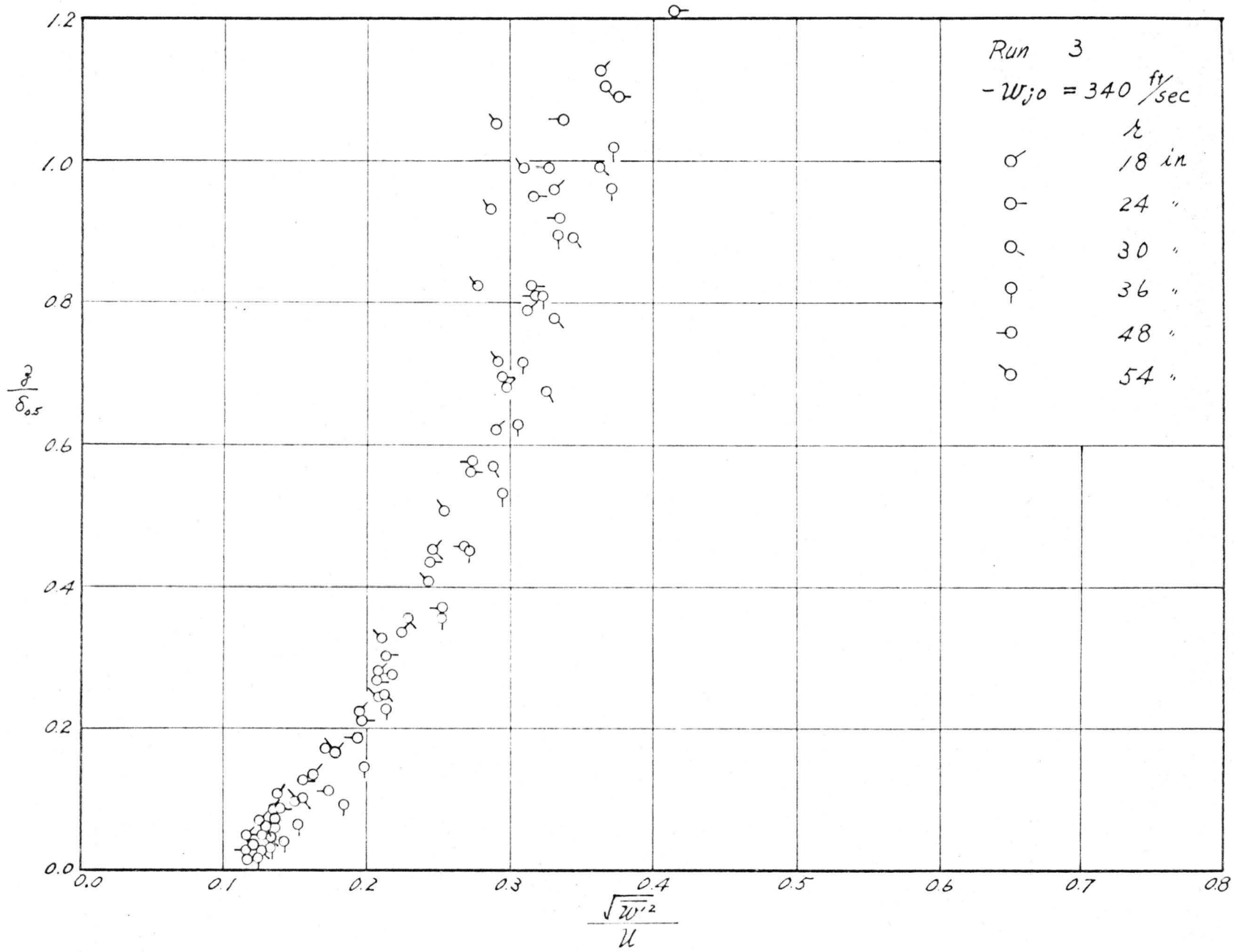

FIG. 34 DISTRIBUTION OF LOCAL VERTICAL INTENSITY OF TURBULENCE

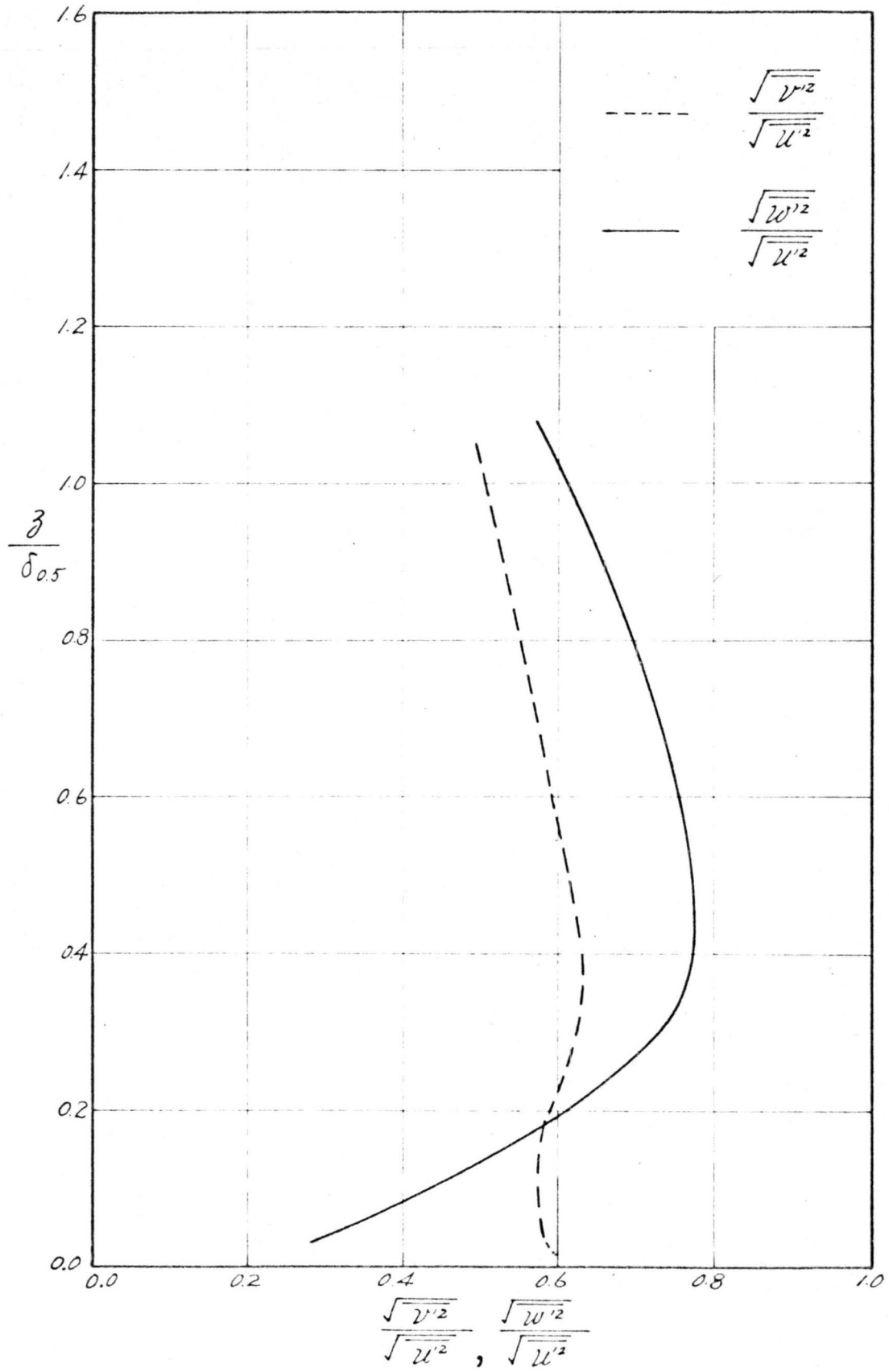

FIG. 35 RATIO OF TURBULENT INTENSITIES

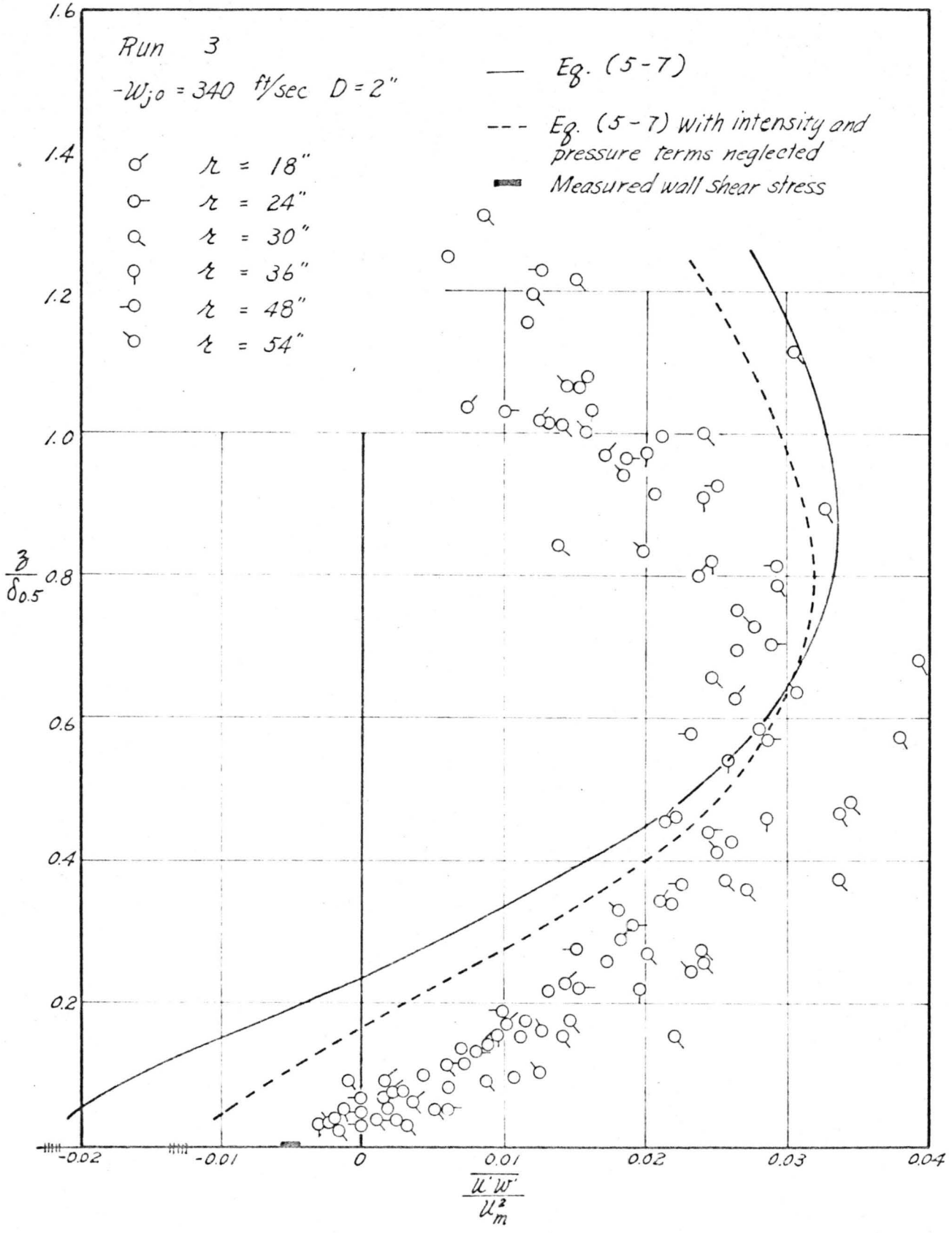

FIG. 36 DISTRIBUTION OF TURBULENT SHEAR STRESS IN RADIAL WALL JET

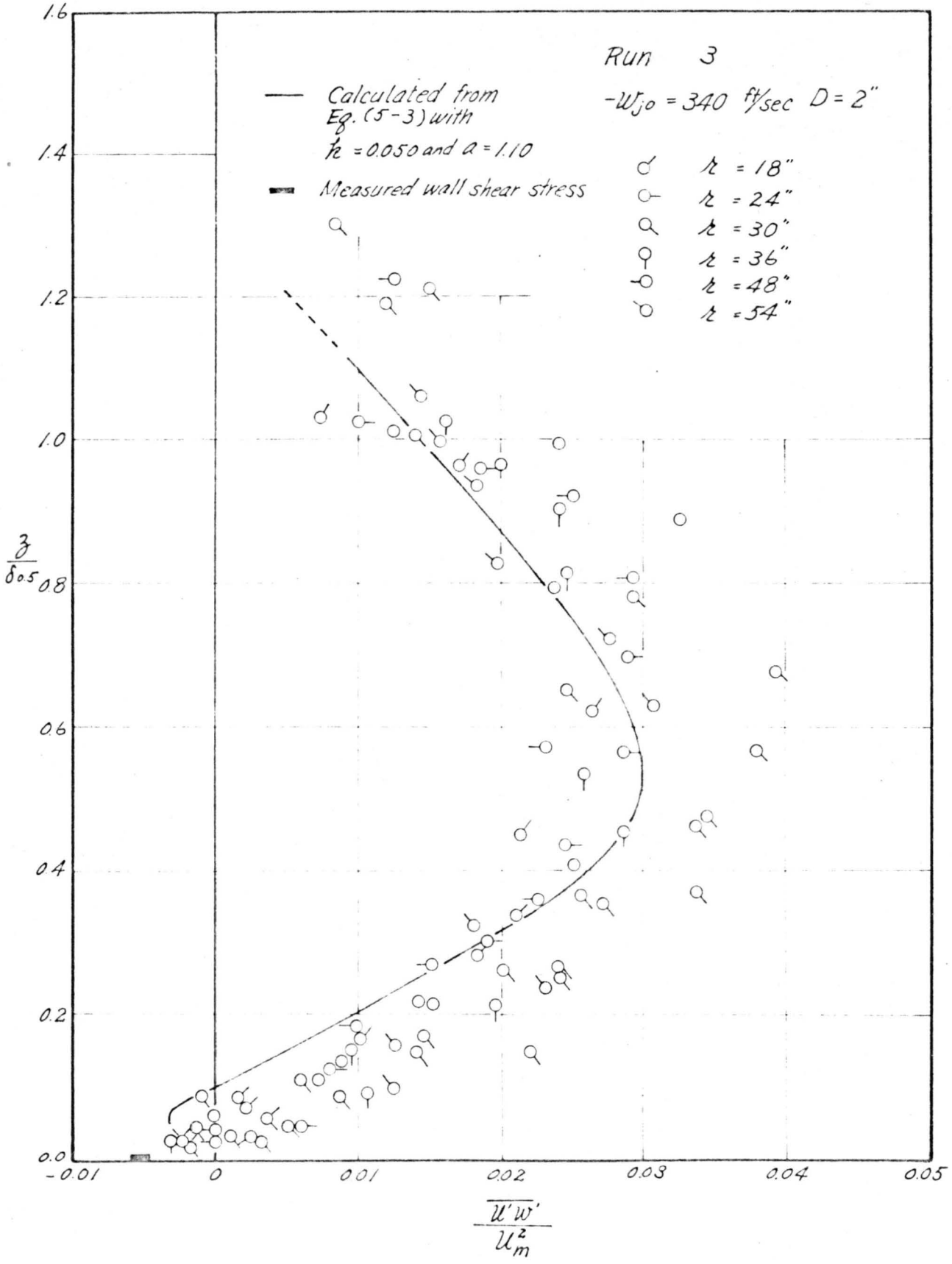

FIG. 37 COMPARISON OF CALCULATED AND MEASURED TURBULENT SHEAR STRESS FOR RADIAL WALL JET

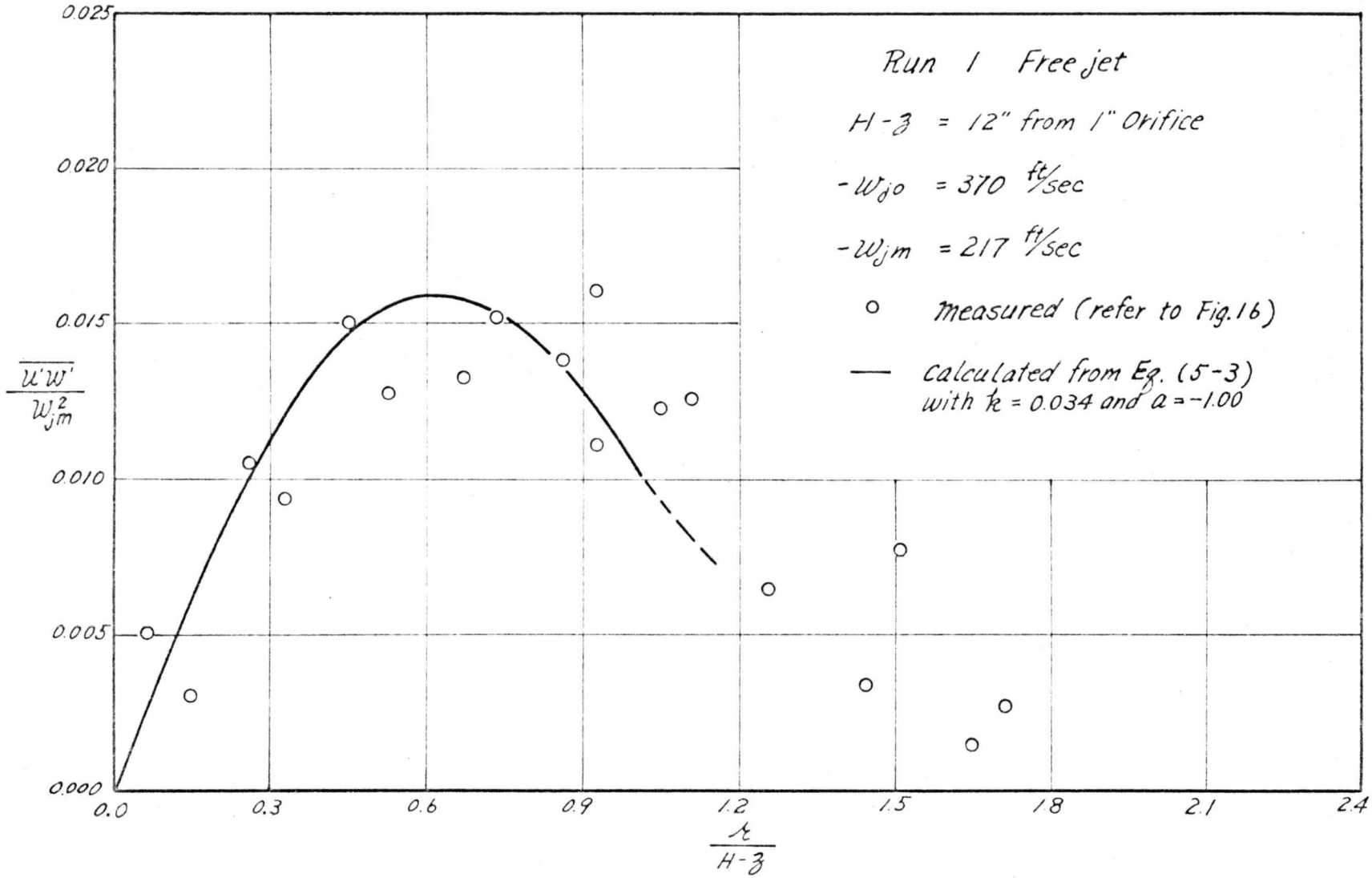

FIG. 38 COMPARISON OF CALCULATED AND MEASURED TURBULENT SHEAR STRESS FOR FREE CIRCULAR JET

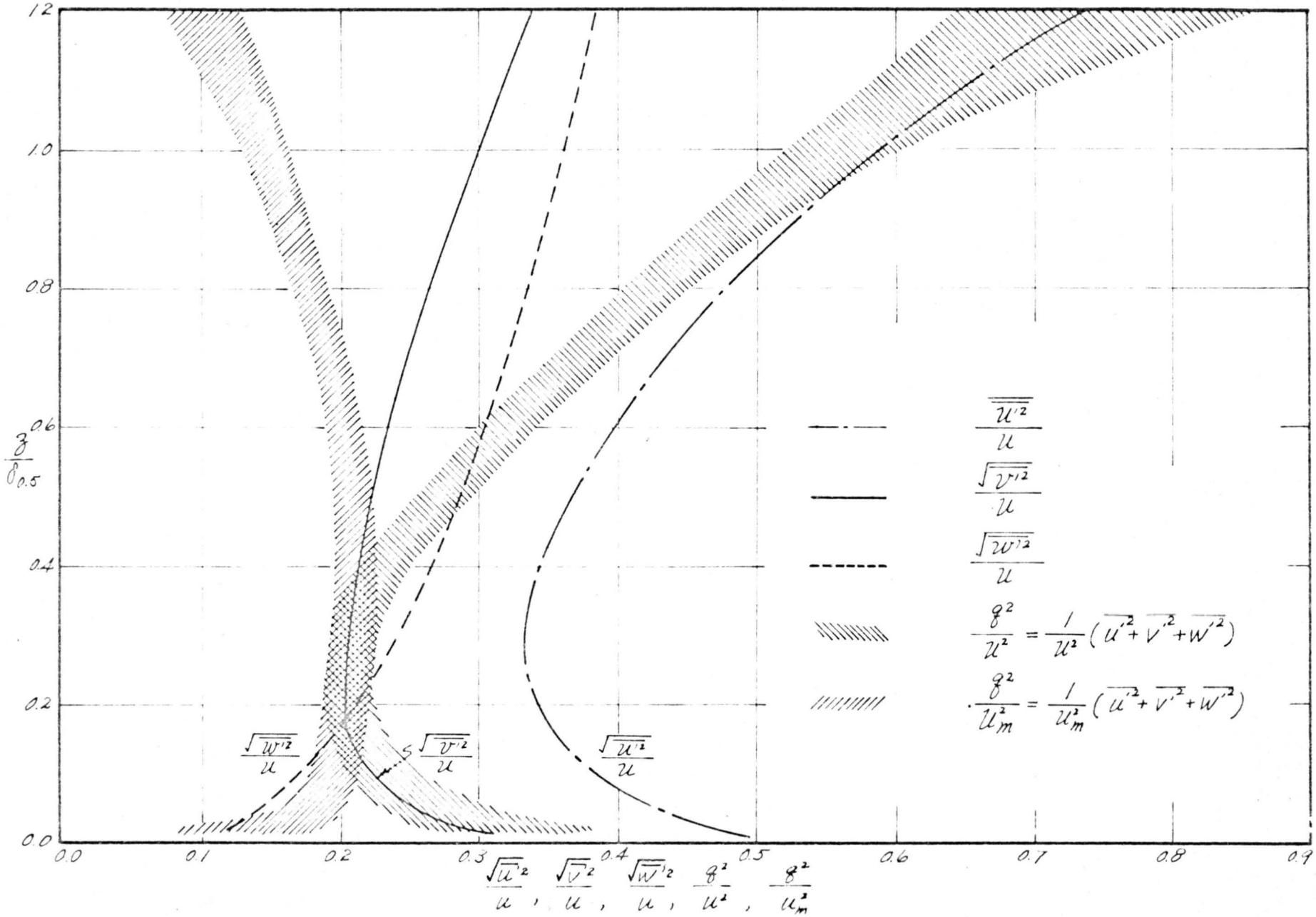

FIG. 39 DISTRIBUTION OF RELATIVE TURBULENT ENERGY

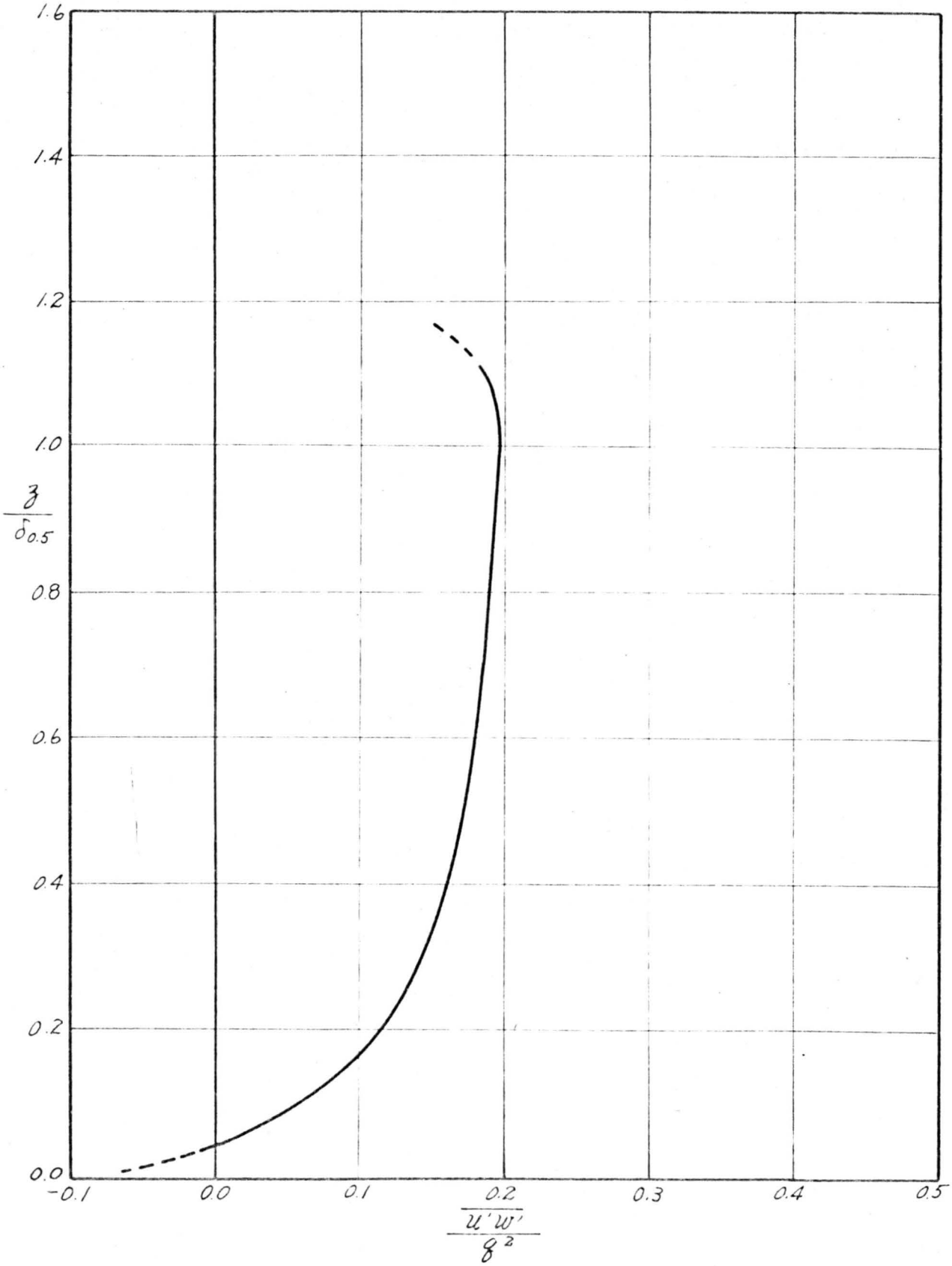

FIG. 40 RATIO BETWEEN TURBULENT SHEAR STRESS AND TURBULENT KINETIC ENERGY

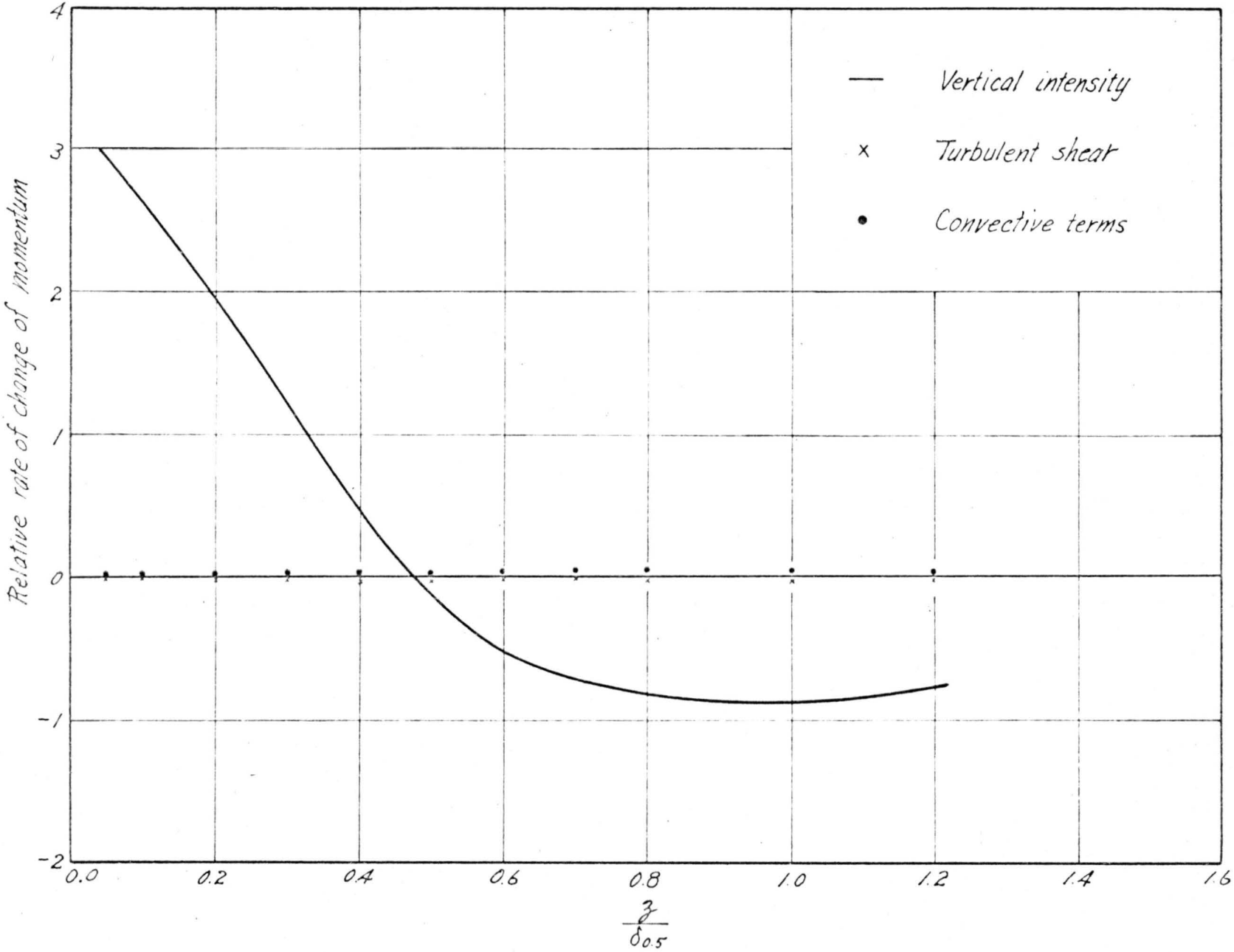

FIG. 41 DISTRIBUTION OF TERMS IN THE VERTICAL COMPONENT OF REYNOLDS EQUATION

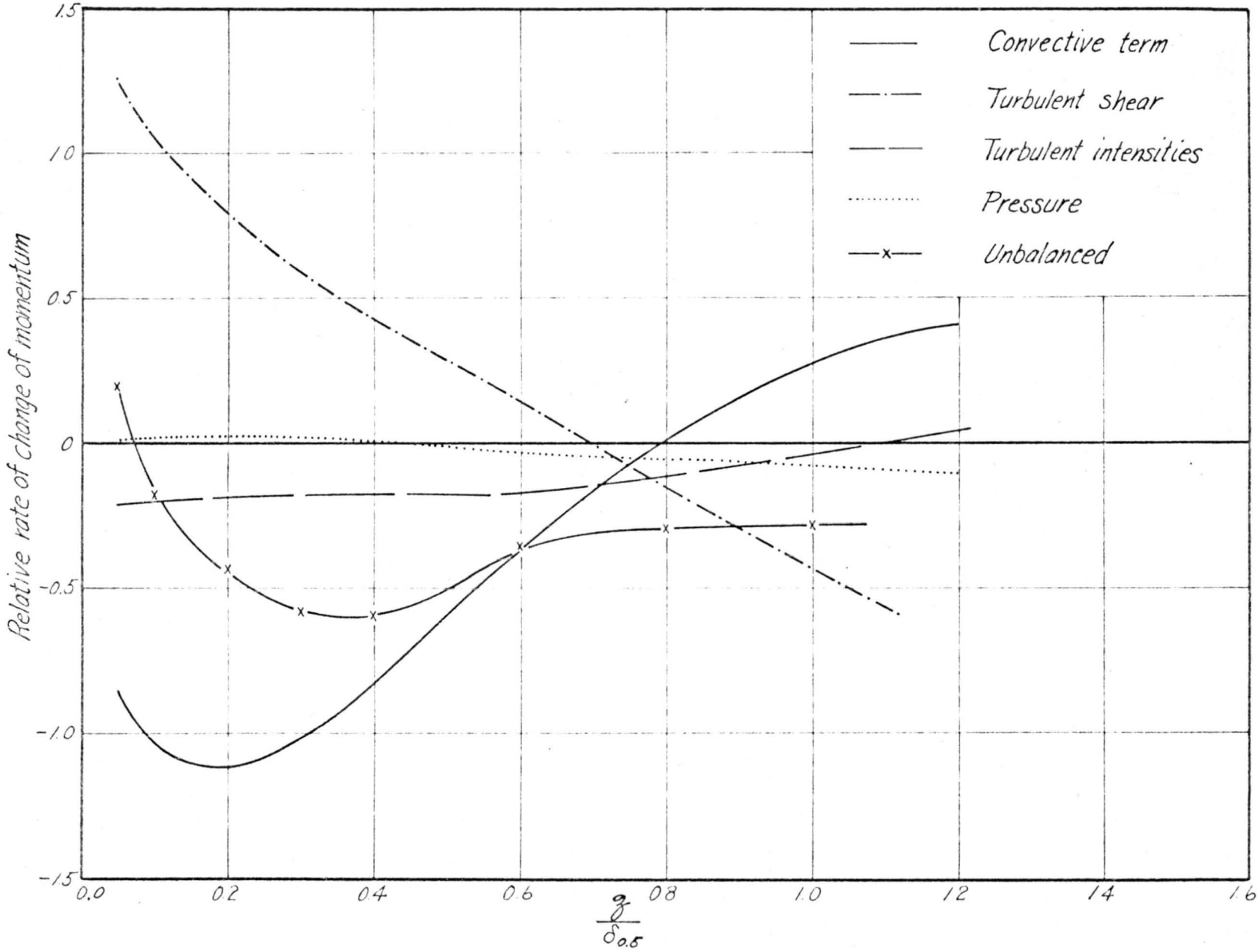

FIG. 42 DISTRIBUTION OF TERMS IN THE RADIAL COMPONENT OF REYNOLDS EQUATION

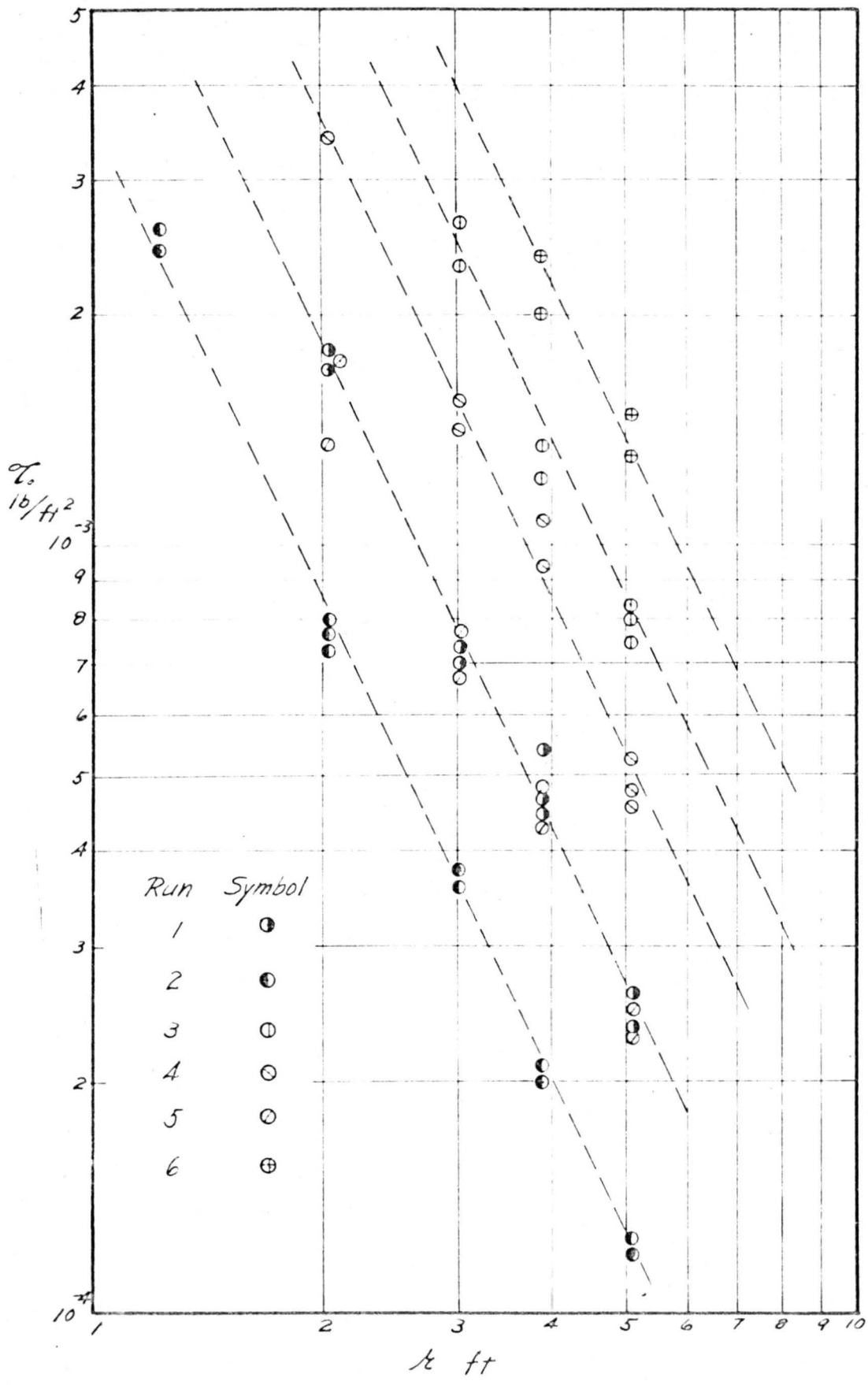

FIG. 43 DISTRIBUTION OF WALL SHEAR STRESS

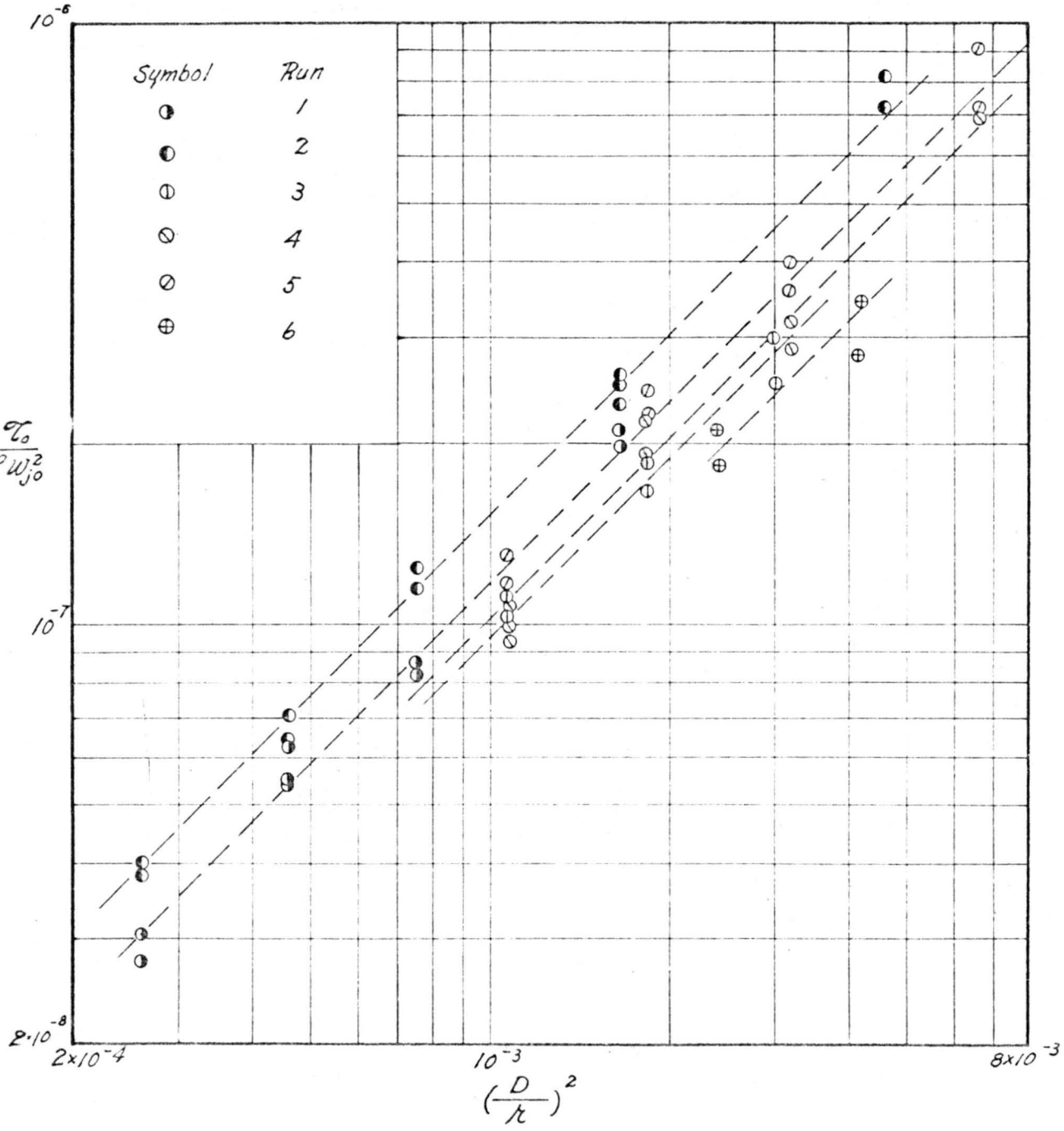

FIG. 44 DISTRIBUTION OF WALL SHEAR STRESS IN DIMENSIONLESS FORM

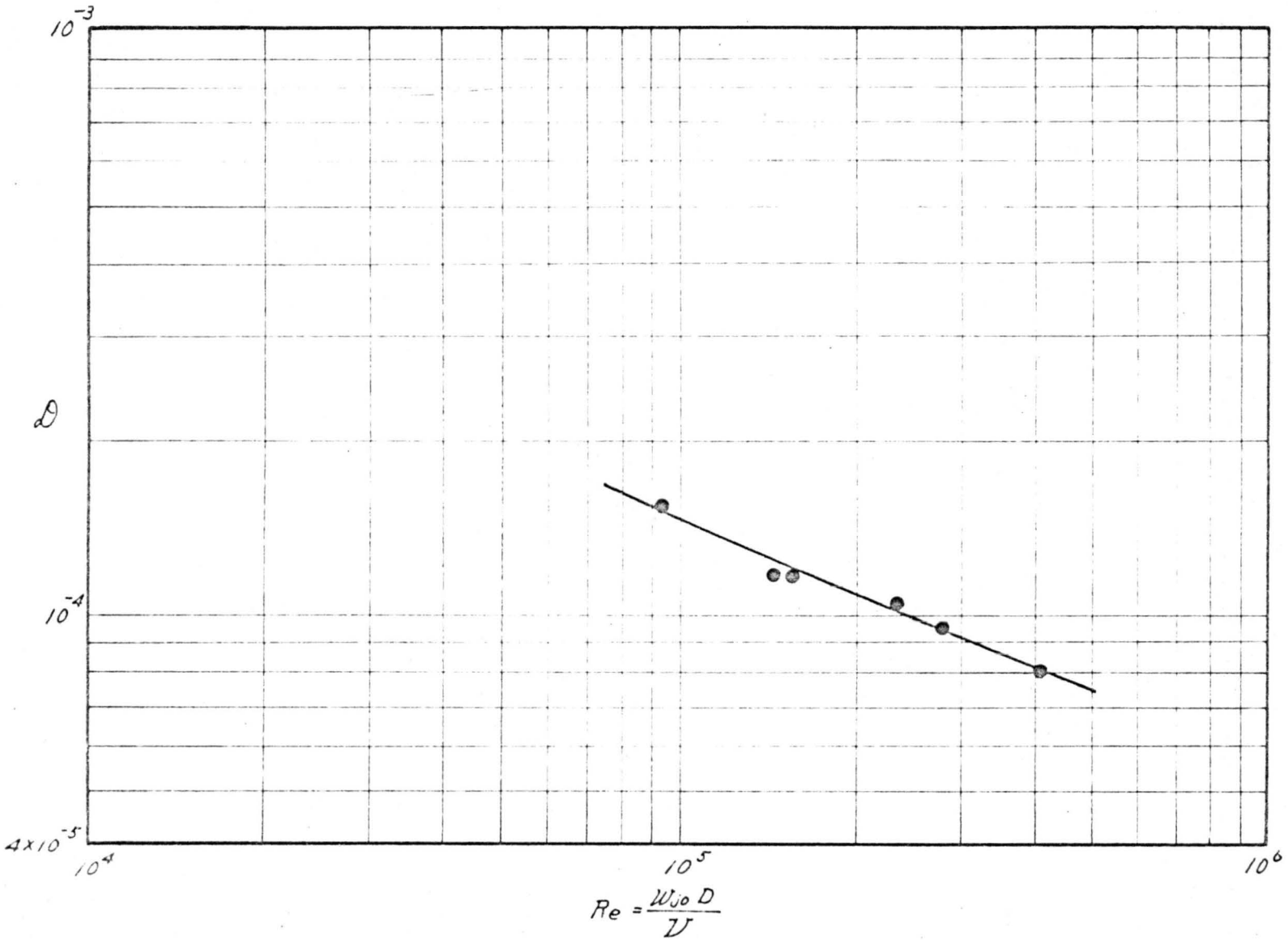

FIG. 45 RELATION BETWEEN REYNOLDS NUMBER AND PROPORTIONALITY FACTOR OF WALL SHEAR EQUATION

APPENDIX A

An Analysis of the Momentum Equation for the Turbulent Wall Jet

by

Junn-Ling Chao and Lionel V. Baldwin

An extensive and careful investigation was made of the turbulent Reynolds equations of motion for axisymmetric boundary-layer flow developed by a jet of air impinging normal to a smooth surface. These equations in the radial and vertical directions for an incompressible radial wall jet with constant physical properties may be written as

$$u\frac{\partial u}{\partial r} + w\frac{\partial u}{\partial z} + \frac{\partial \overline{u'^2}}{\partial r} + \frac{1}{r}\left(\overline{u'^2} - \overline{v'^2}\right) + \frac{\partial \overline{u'w'}}{\partial z} = -\frac{1}{\rho}\frac{\partial p}{\partial z} + \nu\left\{\frac{\partial^2 u}{\partial r^2} + \frac{1}{r}\frac{\partial u}{\partial r} - \frac{u}{r^2} + \frac{\partial^2 u}{\partial z^2}\right\} \qquad (1)^*$$

$$u\frac{\partial w}{\partial r} + w\frac{\partial w}{\partial z} + \frac{\partial \overline{u'w'}}{\partial r} + \frac{\overline{u'w'}}{r} + \frac{\partial \overline{w'^2}}{\partial z} = -\frac{1}{\rho}\frac{\partial p}{\partial z} + \nu\left\{\frac{\partial^2 w}{\partial r^2} + \frac{1}{r}\frac{\partial w}{\partial r} + \frac{\partial^2 w}{\partial z^2}\right\} \qquad (2)^*$$

with the following boundary conditions

$$u = w = u' = v' = w' = 0 \quad , \quad p = p_w \quad \text{at} \quad z = 0$$

and $\quad u = 0 \quad \text{as} \quad z \longrightarrow \infty$

in which p_w is the static pressure at the wall.

From an analysis of the boundary layer approximation, as given in Chapter III - Boundary Layer Approximation, it is possible to write the momentum equation in the vertical direction given by equation 2 (neglecting all small terms) as

$$w\frac{\partial w}{\partial z} + \frac{\partial \overline{w'^2}}{\partial z} = -\frac{1}{\rho}\frac{dp}{\partial z}$$

and

$$\int_0^z \left(w\frac{\partial w}{\partial z} + \frac{\partial \overline{w'^2}}{\partial z}\right) dz = -\frac{1}{\rho}\int_0^z \frac{\partial p}{\partial z}\, dz$$

Since $w = \overline{w'^2} = 0$ at $z = 0$, and $\overline{w'^2} \longrightarrow 0$ as $z \longrightarrow \infty$, then

---

* All symbols in both numbered and unnumbered equations are identified on pages xii and xiii.

$$p_w = \frac{\rho}{2} (w^2)_\infty + p_\infty$$

Furthermore, it can be assumed that a potential flow exists as z becomes infinite, thus

$$p_{atm} = \frac{\rho}{2} (w^2)_\infty + p_\infty \quad \text{where} \quad u = 0 \ ,$$

and

$$p_w = p_{atm}$$

Data plotted on Fig. 3 show that at various locations very close to the smooth deflecting surface, $z = 0^+$, the calculated pressure has a measurable magnitude (although it was not measured). This indicates the existence of a discrepancy in the equality $p_w = p_{atm}$, which may be due to omission of the viscous term in the vertical momentum equation even though laminar viscous stresses are significant in the region very close to the deflecting surface. However, it will be evident in a later section that this apparent paradox does not effect the final result.

If p_{atm} is taken as the reference pressure, the total pressure can be estimated at any given height above the surface for a specified radial station. The corresponding equation is

$$-\frac{1}{\rho} p_z = \frac{1}{2} w_z^2 + \overline{w'^2_z} \tag{3}$$

In equation 3 only $\overline{w'^2}$ can be obtained from experiment. However, the vertical mean velocity can be calculated by means of the equation of conservation of mass given by

$$\frac{\partial U}{\partial r} + \frac{U}{r} + \frac{1}{r} \frac{\partial V}{\partial \phi} + \frac{\partial W}{\partial z} = 0$$

Due to axisymmetry and quasi-steady flow, obtain

$$\frac{\partial}{\partial t} = 0 \ , \quad \frac{\partial}{\partial \phi} = 0 \ , \quad v = 0 \ , \quad v' \neq 0$$

and $\overline{u'v'} = \overline{v'w'} = 0$

in which the primes (') indicate the fluctuation about the mean.

Upon time averaging the equation for the conservation of mass and using the above symmetry conditions we obtain

$$\frac{\partial u}{\partial r} + \frac{u}{r} + \frac{\partial w}{\partial z} = 0 \tag{4}$$

integrating equation 4 gives

$$w = -\frac{1}{r}\int_0^z \left(u + r\frac{\partial u}{\partial r}\right) dz$$

From the similarity consideration for the radial mean velocity as given in Chapter III - Similarity Consideration, introduce into equation 4 the relation

$$\mathcal{U} = \frac{u}{u_m}$$

and $$\zeta = \frac{z}{\delta_{0.5}}$$

in which $\delta_{0.5}$ and u_m are functions of r only.

Thus

$$\frac{\partial u}{\partial r} = \frac{\partial}{\partial r}(\mathcal{U} u_m) = \mathcal{U}\frac{\partial u_m}{\partial r} + u_m \frac{\partial \mathcal{U}}{\partial r}$$

$$= \mathcal{U} A\, a r^{a-1} + u_m \frac{\partial \mathcal{U}}{\partial \zeta}\frac{\partial \zeta}{\partial r}$$

$$= \mathcal{U}_a \frac{u_m}{r} + u_m \frac{\partial \mathcal{U}}{\partial \zeta}\left[\frac{z}{D}(-r^2)\right]$$

$$= \mathcal{U}_a \frac{u_m}{r} - \frac{u_m}{r}\zeta\frac{\partial \mathcal{U}}{\partial \zeta}$$

in which

$$u_m = A r^a, \quad \delta_{0.5} = Dr$$

and

$$w = -\frac{1}{r}\int_0^z u_m \left(\mathcal{U} + a\mathcal{U} - \zeta\frac{\partial \mathcal{U}}{\partial \zeta}\right) dz$$

$$= -\frac{1}{r}\left[u_m \delta_{0.5}(1+a)\int_0^\zeta \mathcal{U}\, d\zeta + \delta_{0.5} u_m \int_0^\zeta \zeta \frac{\partial \mathcal{U}}{\partial \zeta}\, d\zeta\right]$$

$$= \frac{1}{r}\left[\zeta \delta_{0.5} u_m \mathcal{U} - u_m \delta_{0.5}(2+a)\int_0^\zeta \mathcal{U}\, d\zeta\right]$$

$$= \frac{\delta_{0.5} u_m}{r}\left[\zeta \mathcal{U} - 0.9\int_0^\zeta \mathcal{U}\, d\zeta\right]$$

in which $a = -1.10$

The plot of data in Fig. 1 shows that the values of the vertical mean velocity though small are not negligible, especially in the region far above the deflecting surface. This point is further emphasized in Figs. 2-a to 2-d which shows that at lower elevations, the value of p is primarily determined by the magnitude of $\overline{w'^2}$. It is noteworthy, however, that as z increases the vertical mean velocity, w, becomes increasingly important. Finally the value of p equals the value of $1/2\, w^2$ as z becomes greater than a few feet.

Using experimental data, each term as it appears in eq. 1 is plotted against the vertical axis for a given radial station. These plots are shown on Figs. 4-a to 9-d. By neglecting the viscous term, since it is not important except very close to the smooth surface, eq. 1 was then integrated term by term from $z = 0^+$ to $z = z$ for a number of radial stations. The results for one station have been plotted on Figs. 10-a to 10-d. Of interest on these figures is the relatively large magnitude of the radial turbulent intensity term. Explanation of this fact is not clearly understood. Although the radial pressure gradient term is small, its magnitude is in the desired direction to balance the momentum equation; and, furthermore, although the balance of the momentum equation is still incomplete, the experimental data show the significant Reynolds stress terms for axisymmetric boundary-layer flow developed by a jet impinging on a normal smooth surface.

An additional characteristic of the flow field of interest to be noted on Fig. 11 is that $\overline{u'w'} = 0$ and $\frac{\partial u}{\partial z} = 0$ do not occur at the same plane, and, furthermore, the distance between these two planes increases as the radial distance from the stagnation point increases. This is an unusual phenomena, which, from a careful review of literature, has been discussed only twice previously.

The initial phase of study of the flow characteristics of a radial wall jet formed by the normal impingement of an air jet on a smooth flat plate has been completed. The case of the rough flat plate should now be investigated to make the results of the initial study more meaningful.

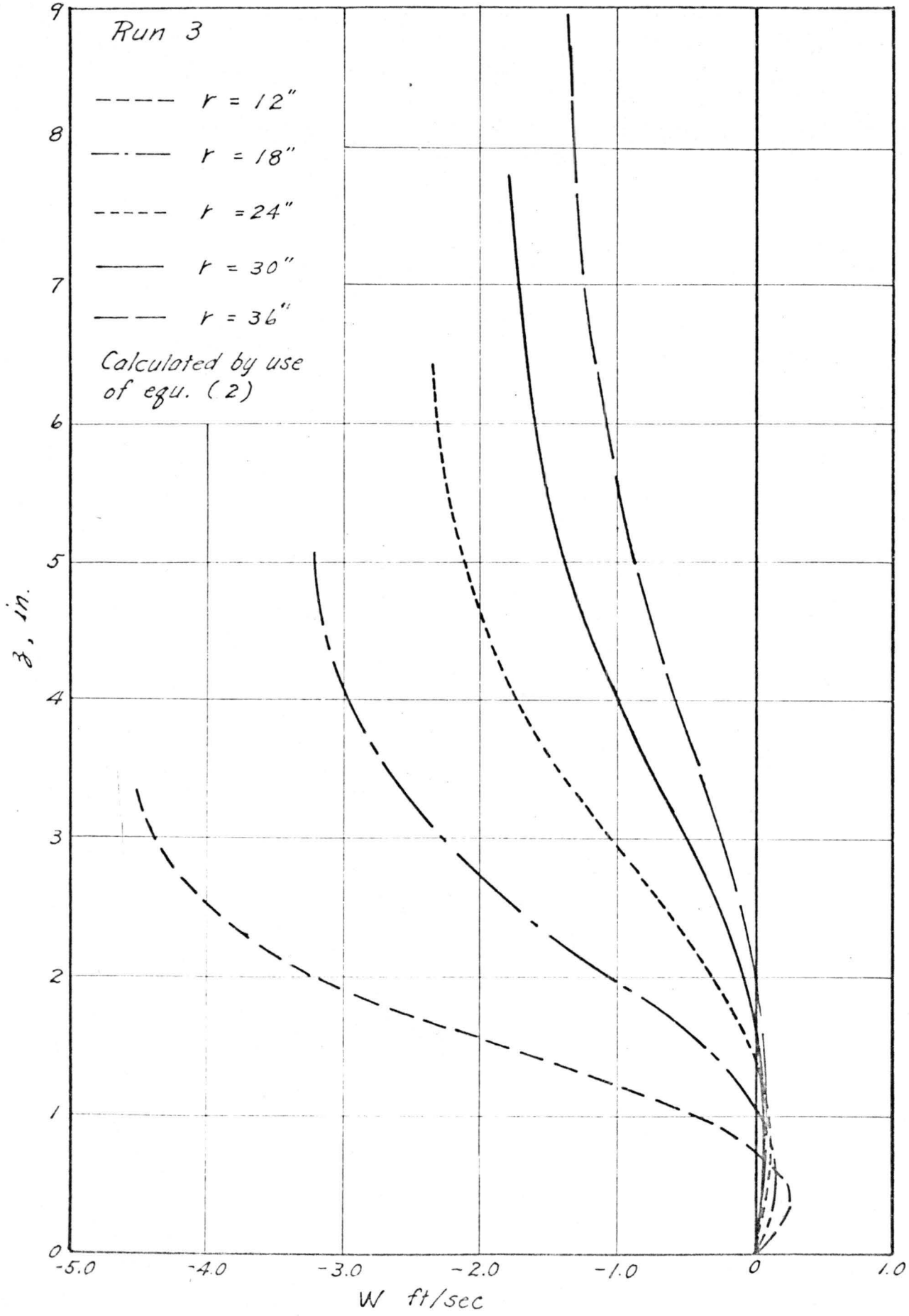

Fig. 1 Vertical Distribution of Vertical Mean Velocity

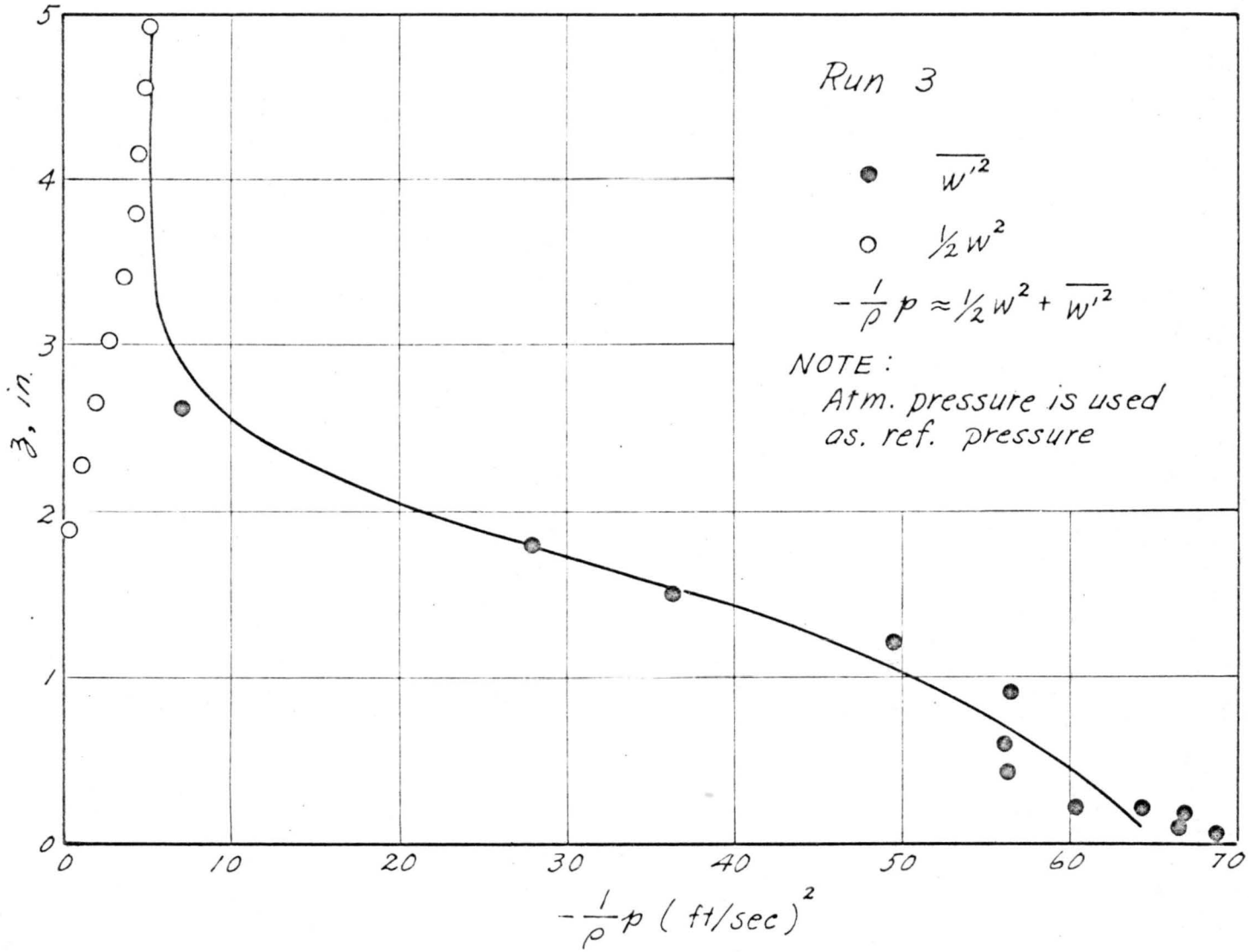

Fig. 2a Calculated Pressure Distribution At Sta. r=18"

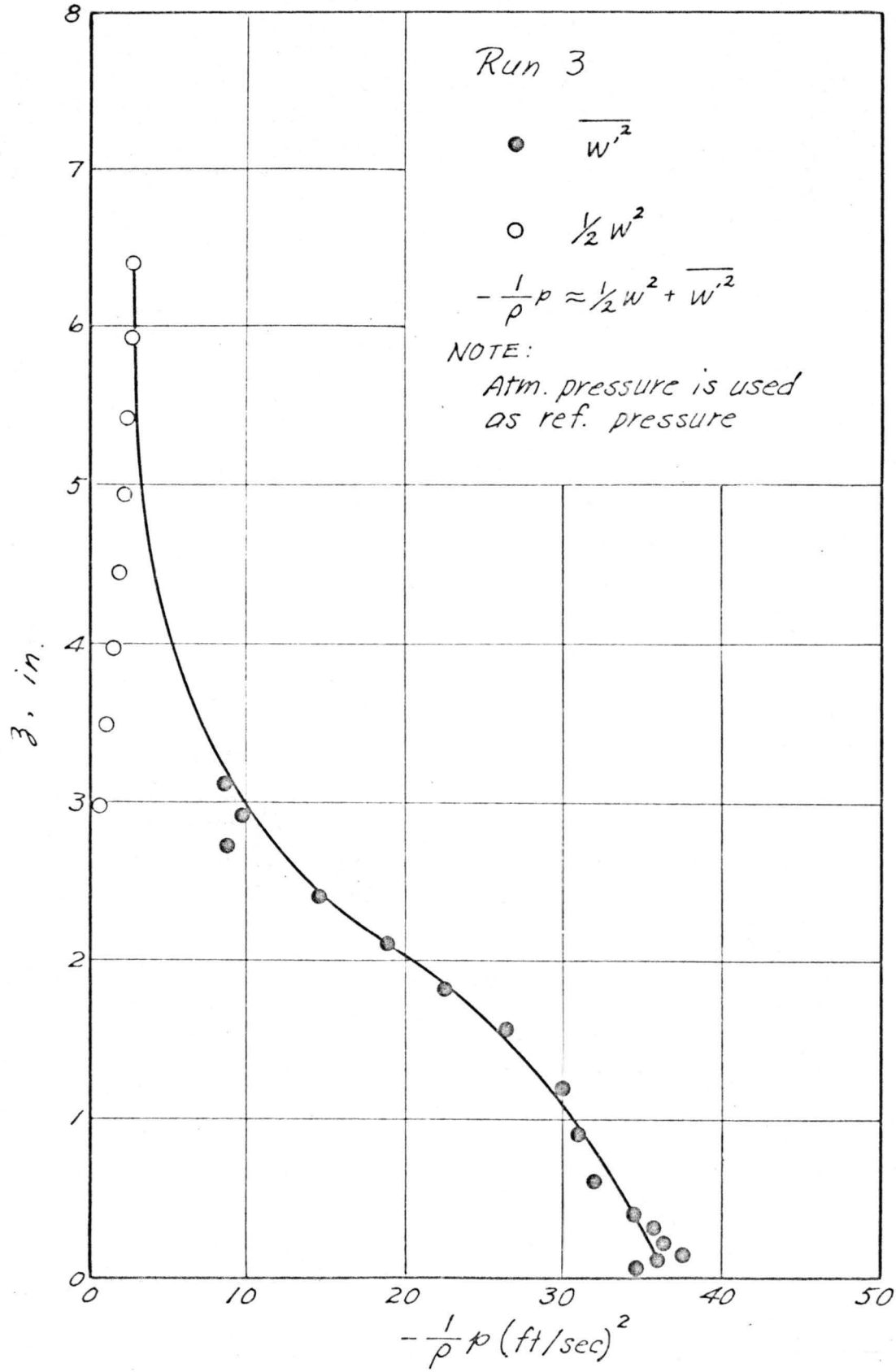

Fig. 2b Calculated Pressure Distribution At Sta. r = 24"

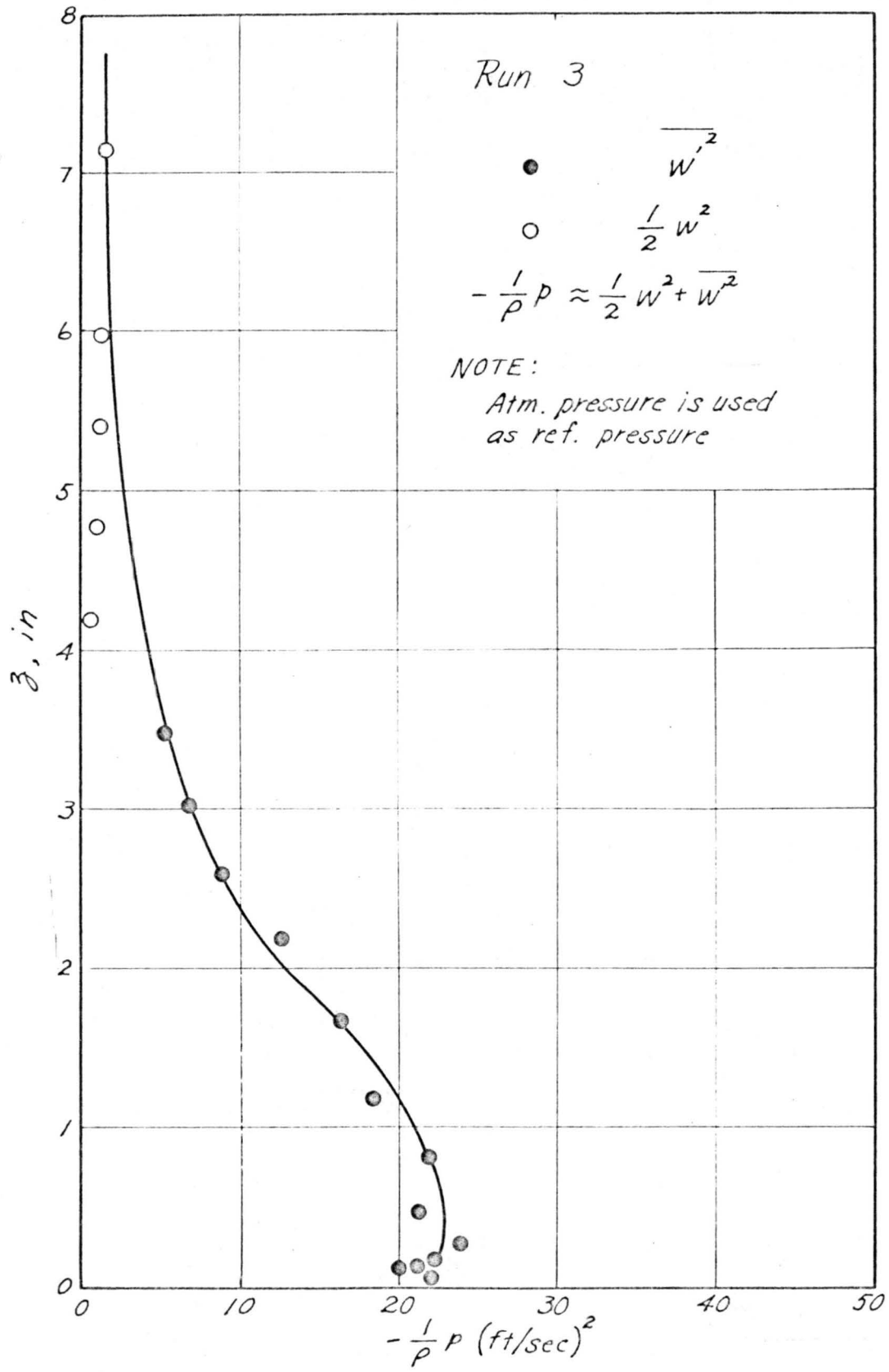

Fig. 2c Calculated Pressure Distribution At Sta. r = 30"

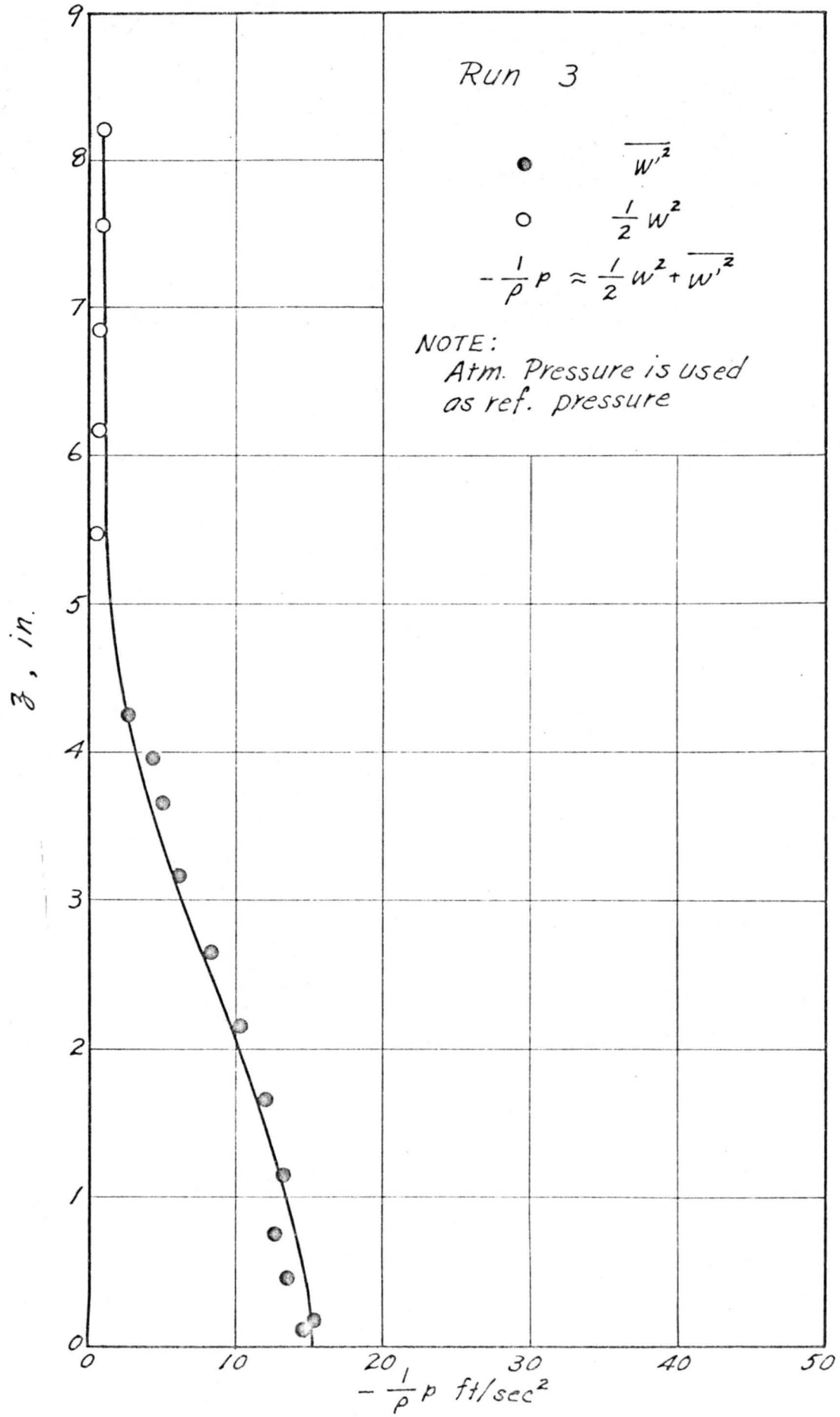

Fig. 2d Calculated Pressure Distribution At Sta. r = 36"

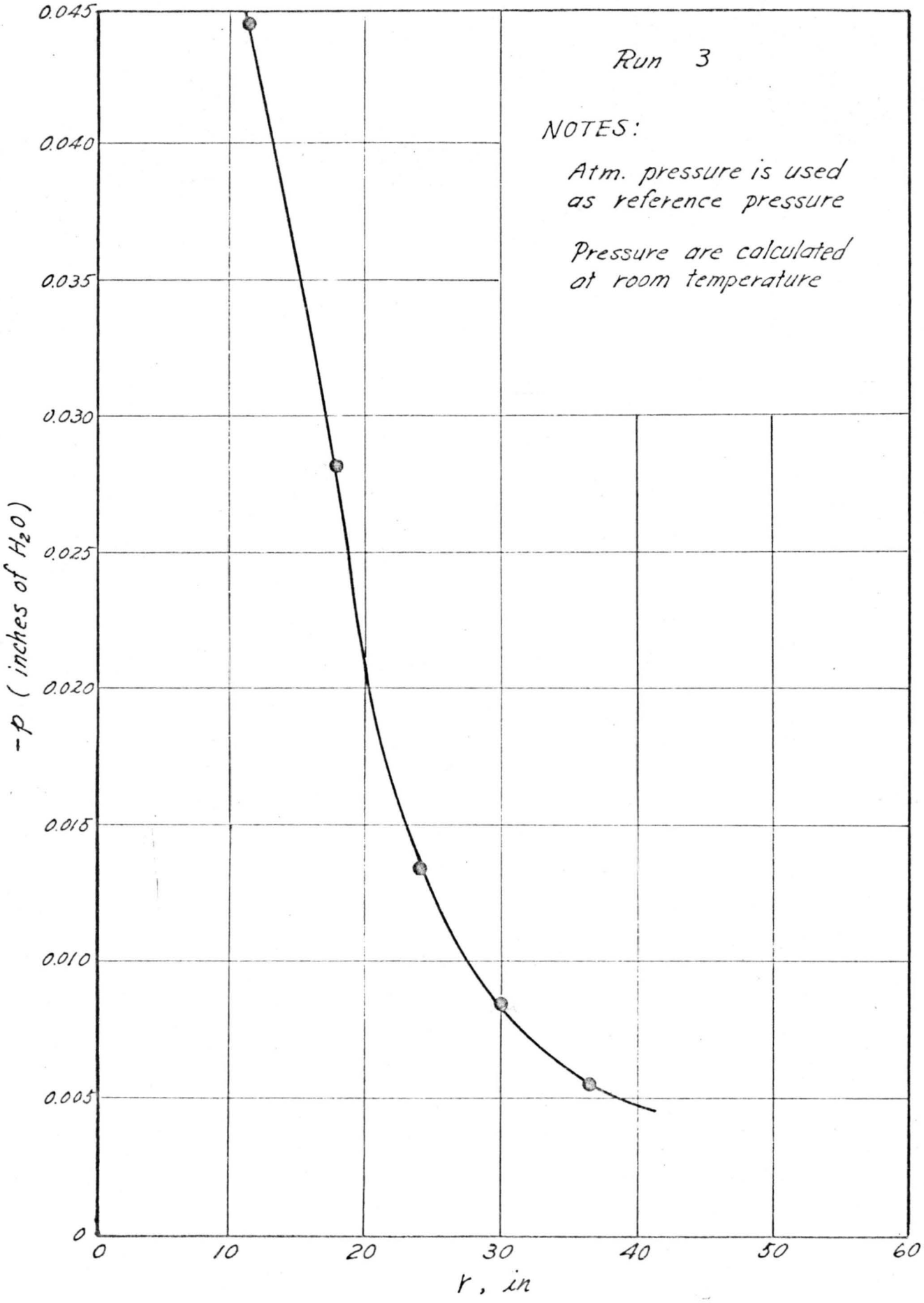

Fig. 3 Calculated Vertical Pressure Drop as $Z \neq 0$ Along the Radial Direction

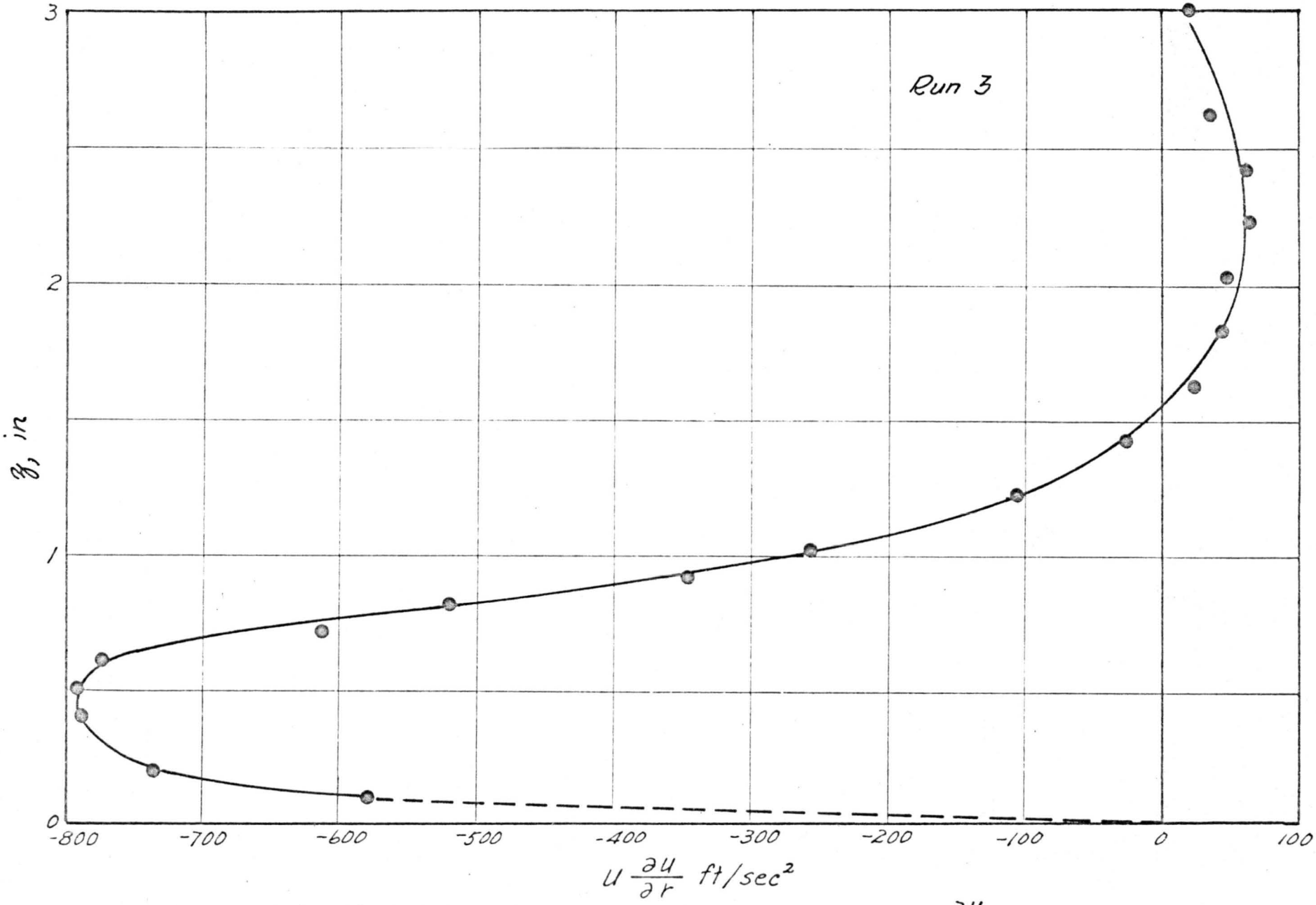

Fig. 4a Distribution of Radial Convective Acceleration $u\frac{\partial u}{\partial r}$ At Sta. $r = 18"$

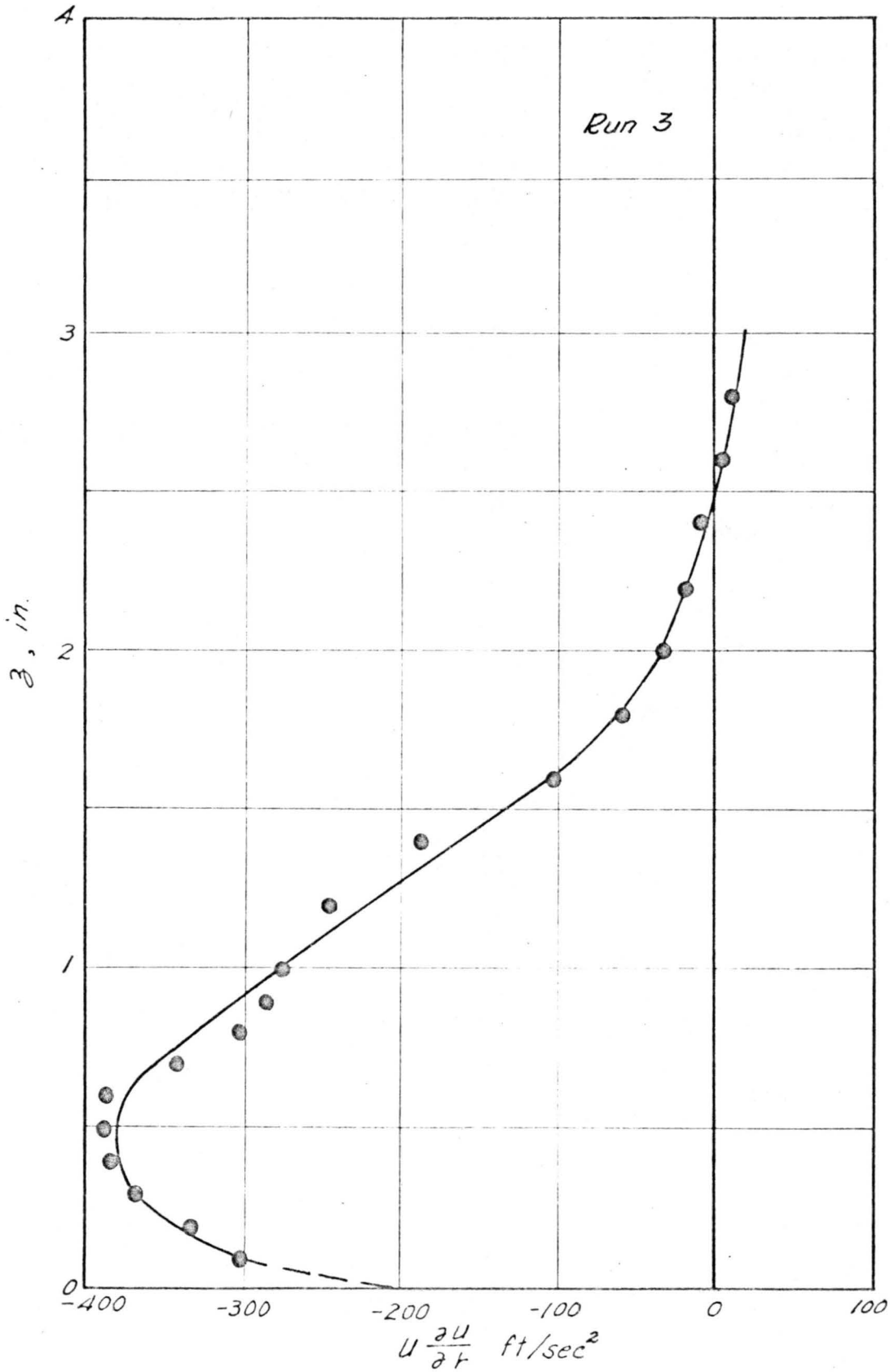

Fig. 4b Distribution of Radial Convective Acceleration $u\frac{\partial u}{\partial r}$ At Sta. $r = 24"$

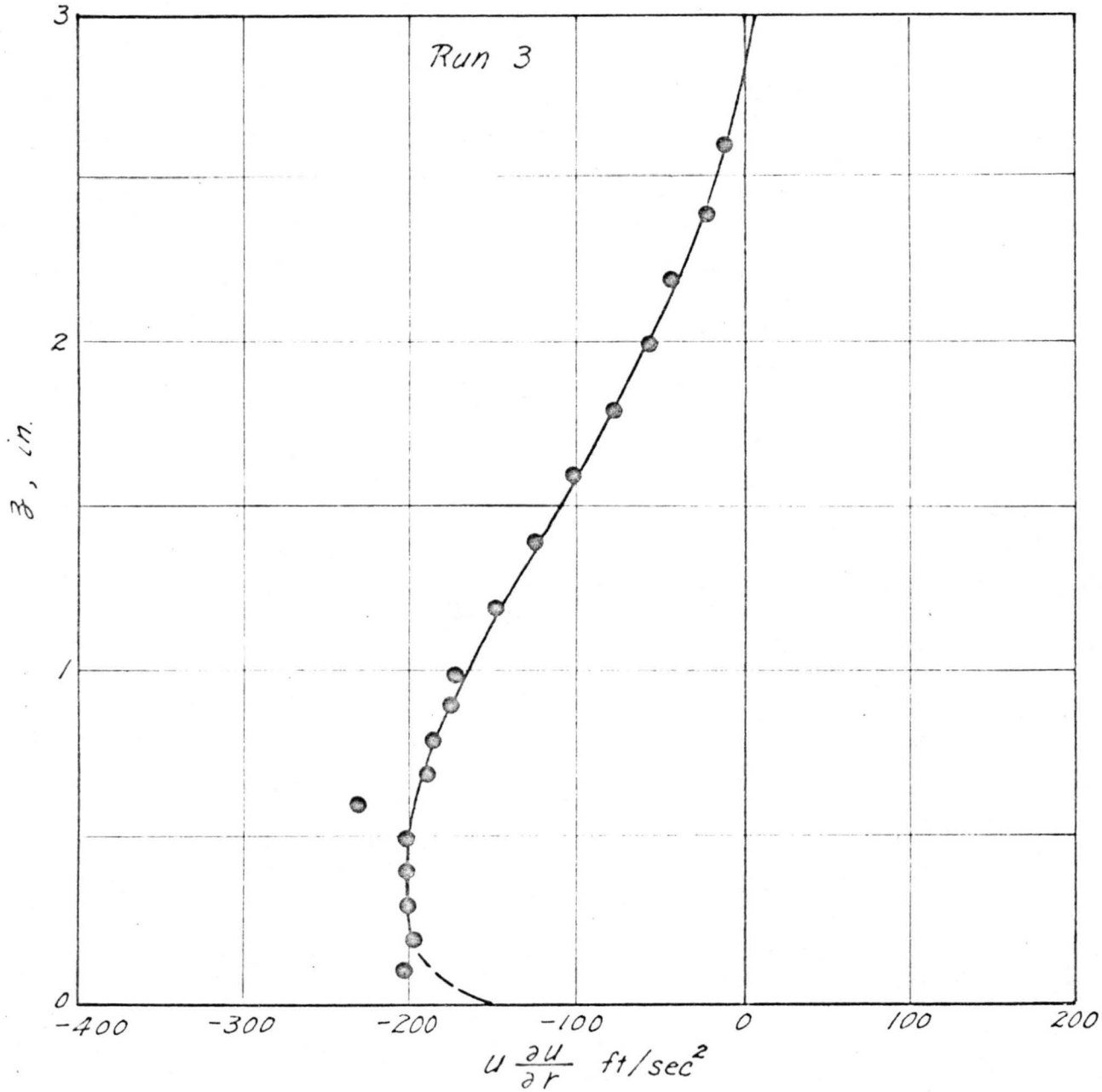

Fig. 4c Distribution of Radial Convective Acceleration $u\frac{\partial u}{\partial r}$ At Sta. $r = 30''$

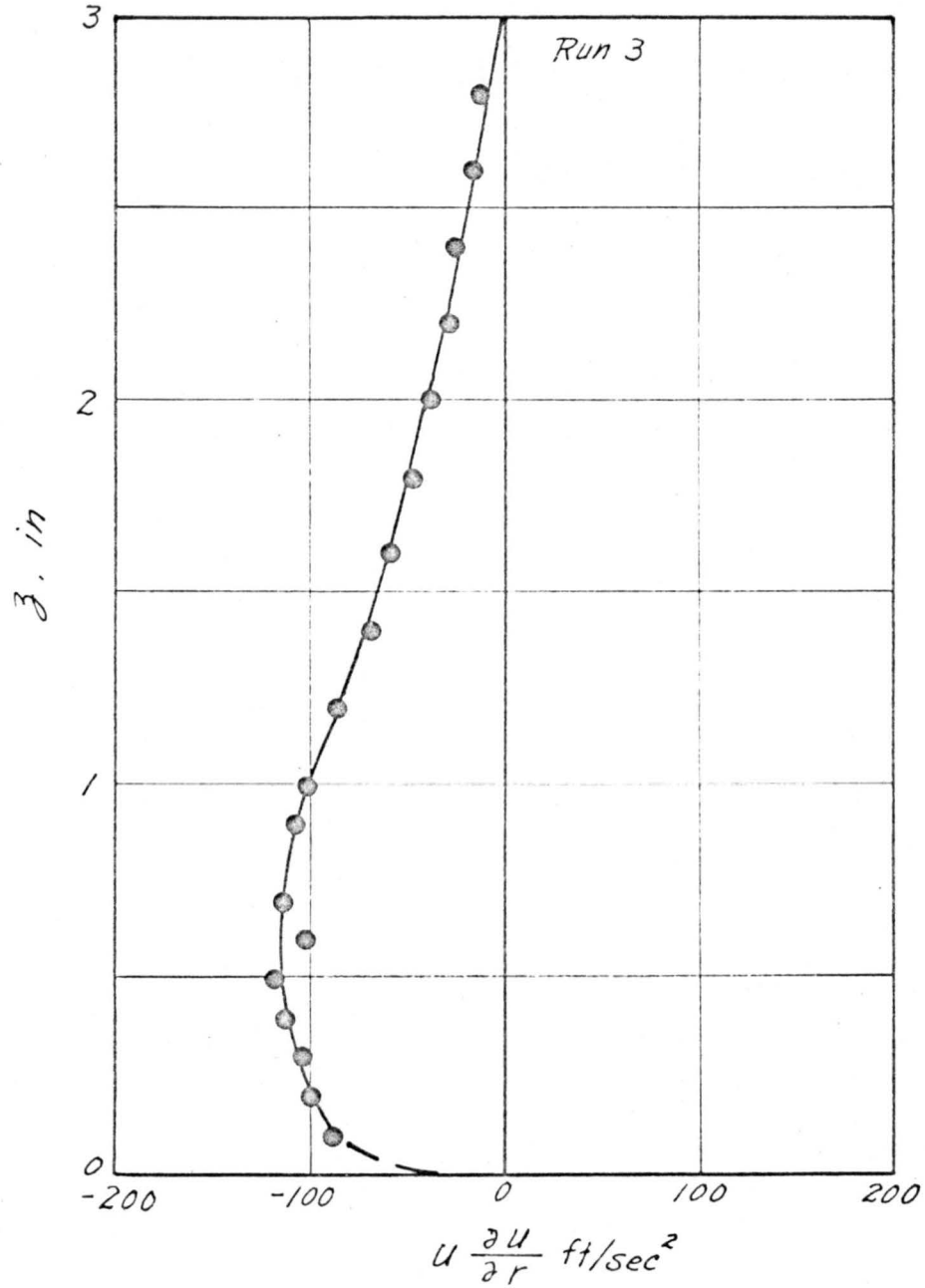

Fig. 4d Distribution of Radial Convective Acceleration $u\frac{\partial u}{\partial r}$ At Sta. r=36"

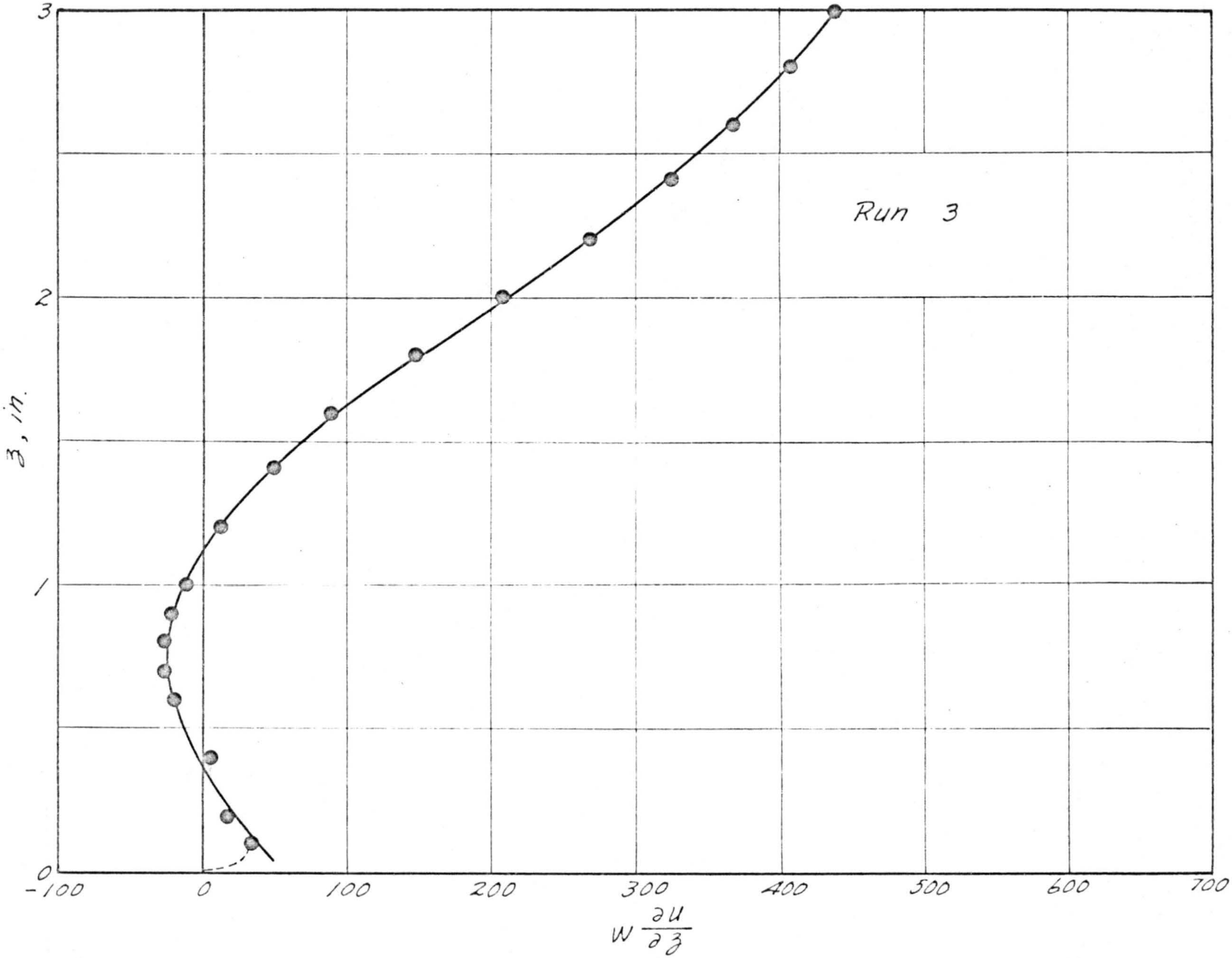

Fig. 5a Distribution of Radial Convective Acceleration $w\frac{\partial u}{\partial z}$ At Sta. r=18"

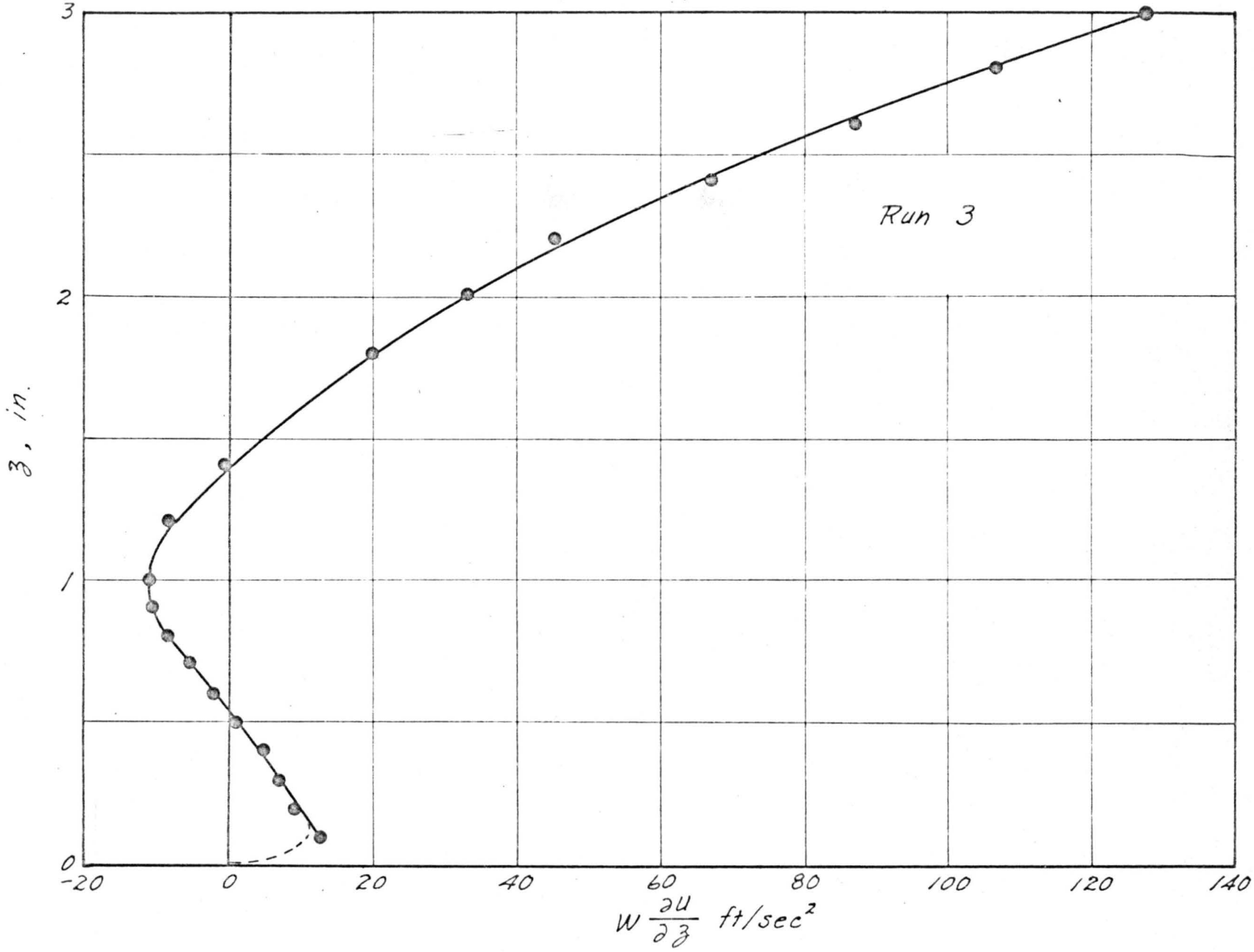

Fig. 5b Distribution of Radial Convective Acceleration $W\frac{\partial u}{\partial z}$ At Sta. r=24"

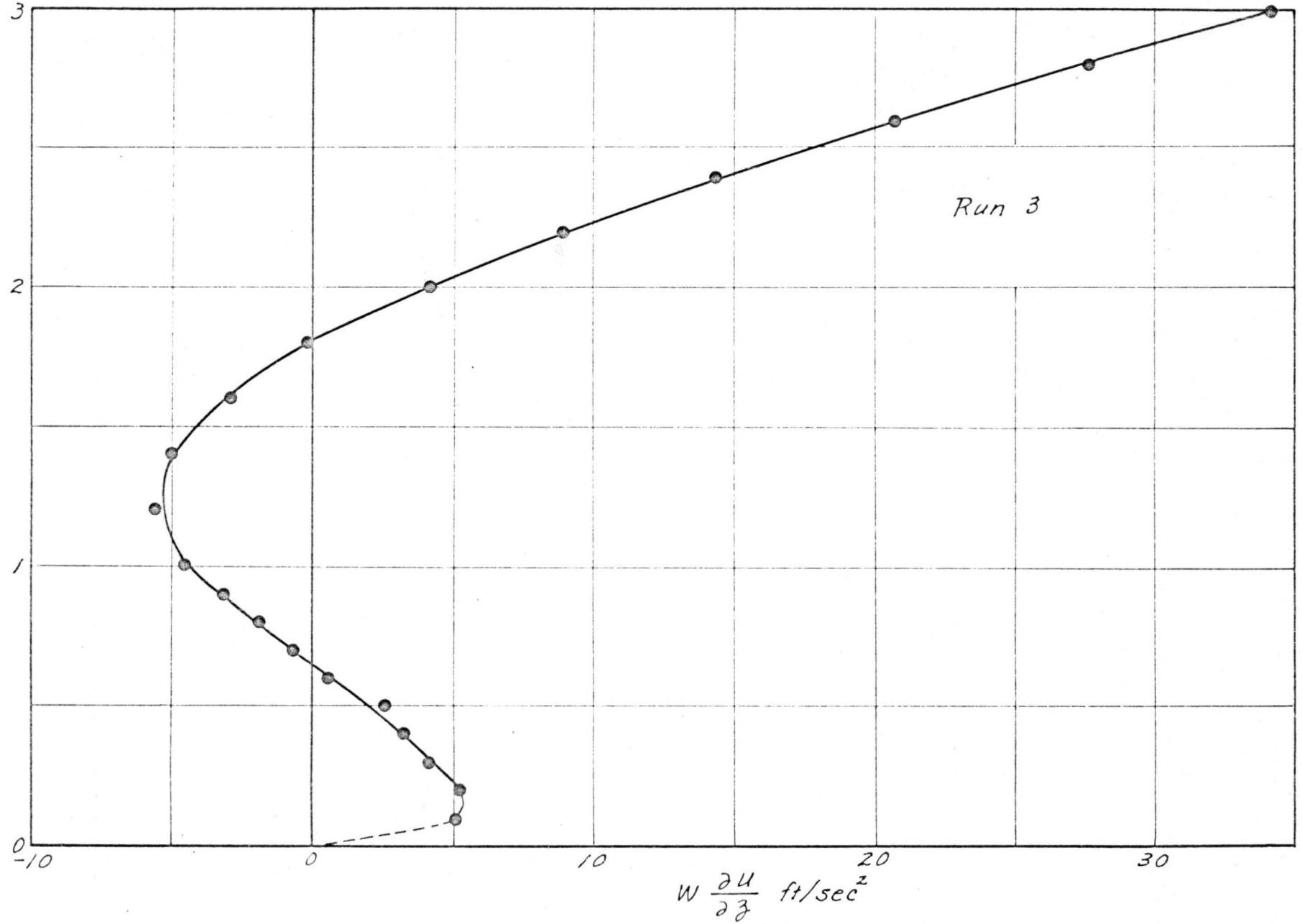

Fig. 5c. Distribution of Radial Convective Acceleration $W\frac{\partial u}{\partial z}$ At Sta. $r = 30''$

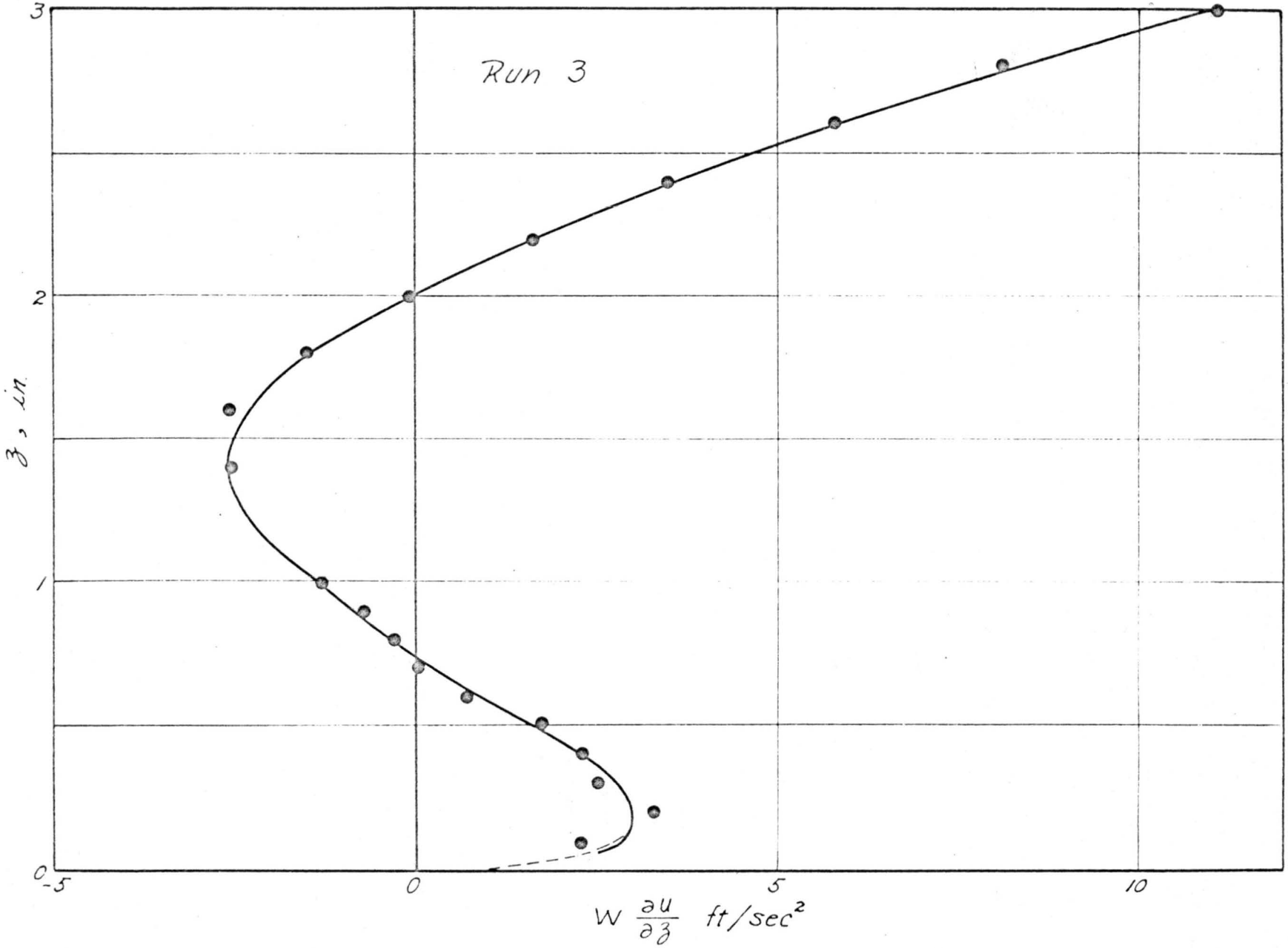

Fig. 5d Distribution of Radial Convective Acceleration $W \frac{\partial u}{\partial z}$ At Sta. $r = 36''$

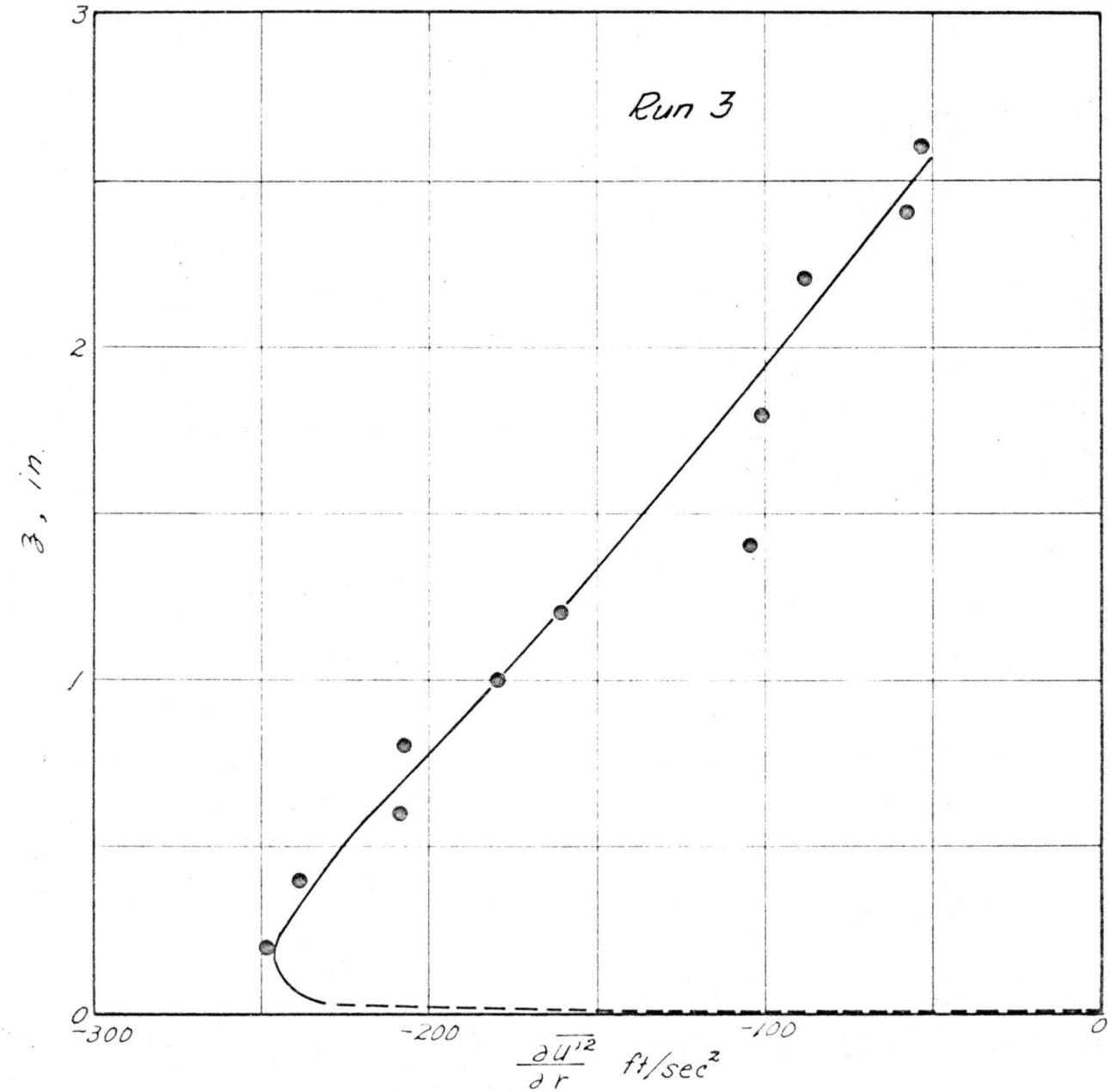

Fig. 6a Distribution of Rate of Change of Radial Turbulent Intensity
At Sta. r = 18"

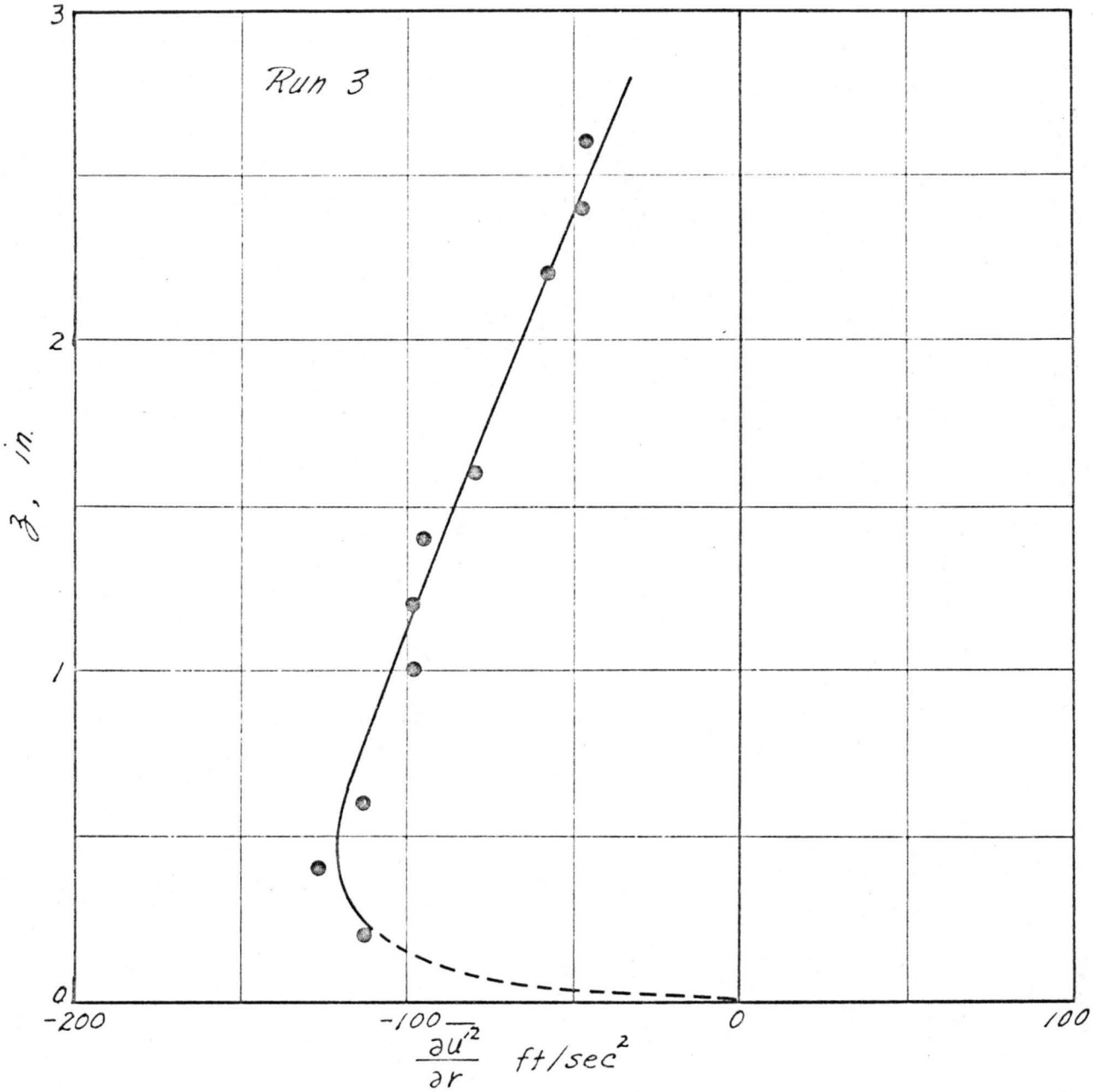

Fig. 6b Distribution of Rate of Change of Radial Turbulent Intensity At Sta. r = 24"

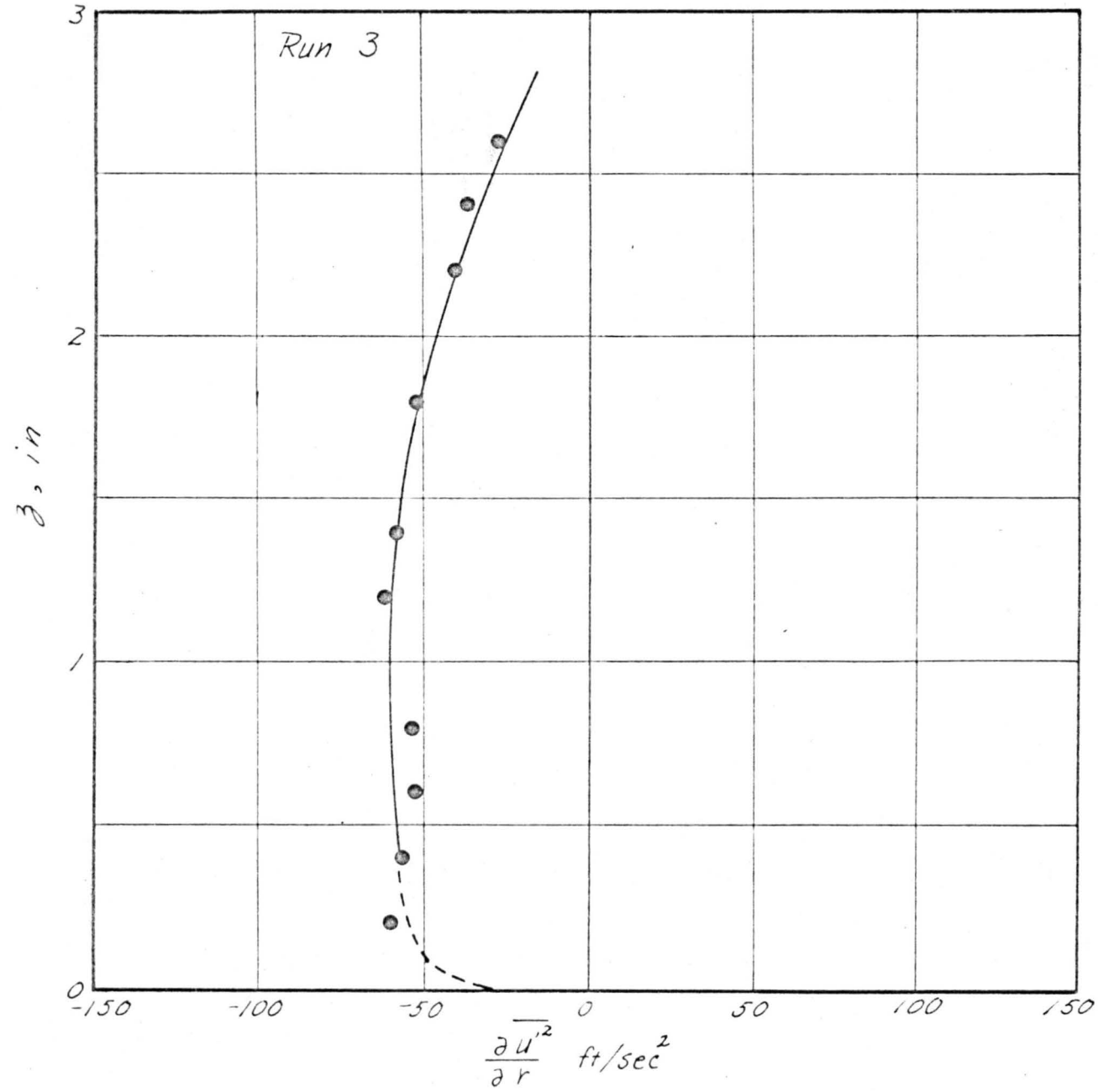

Fig. 6c Distribution of Rate of Change of Radial Turbulent Intensity At Sta. r=30"

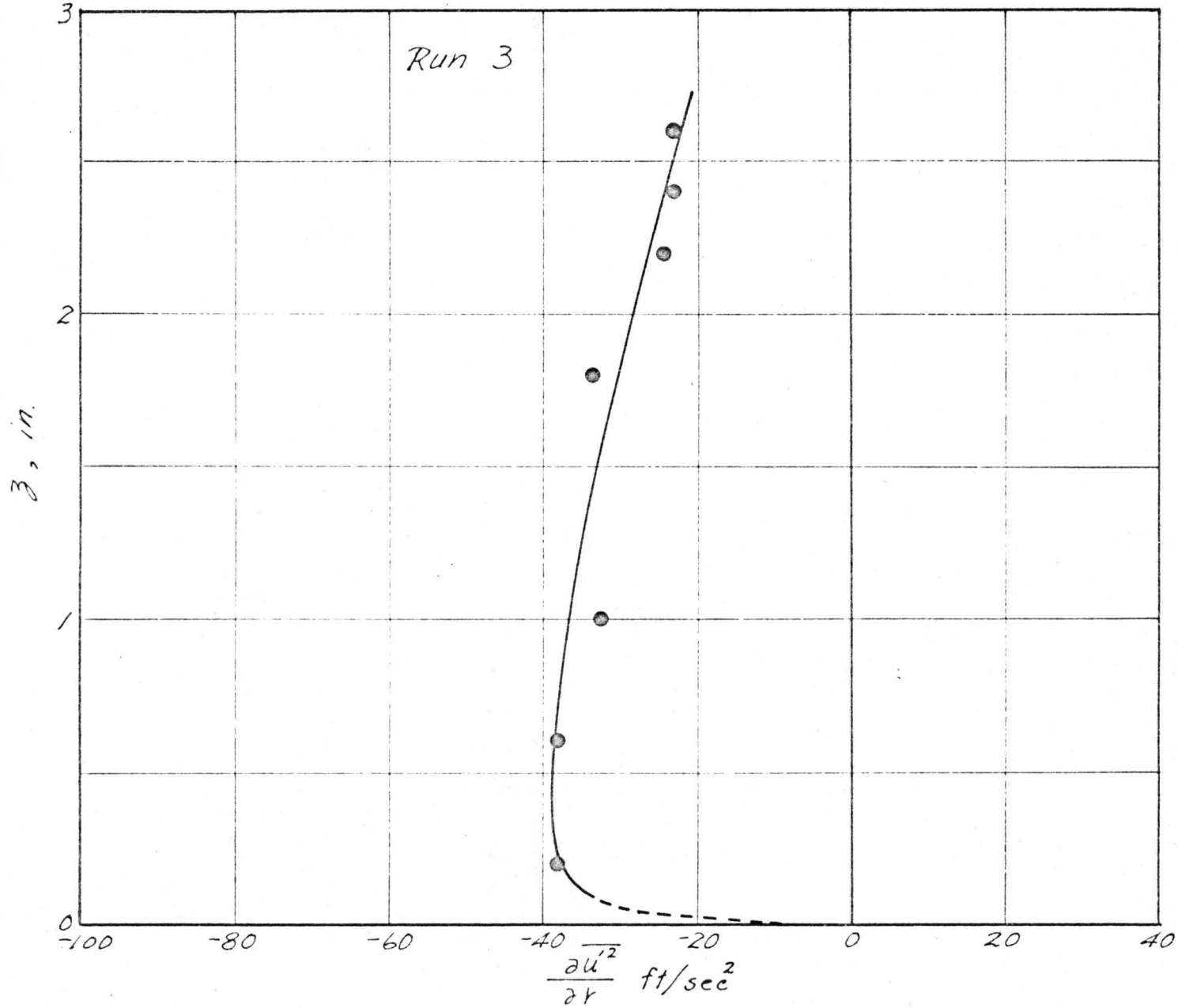

Fig. 6d Distribution of Rate of Change of Radial Turbulent Intensity At Sta. r=36"

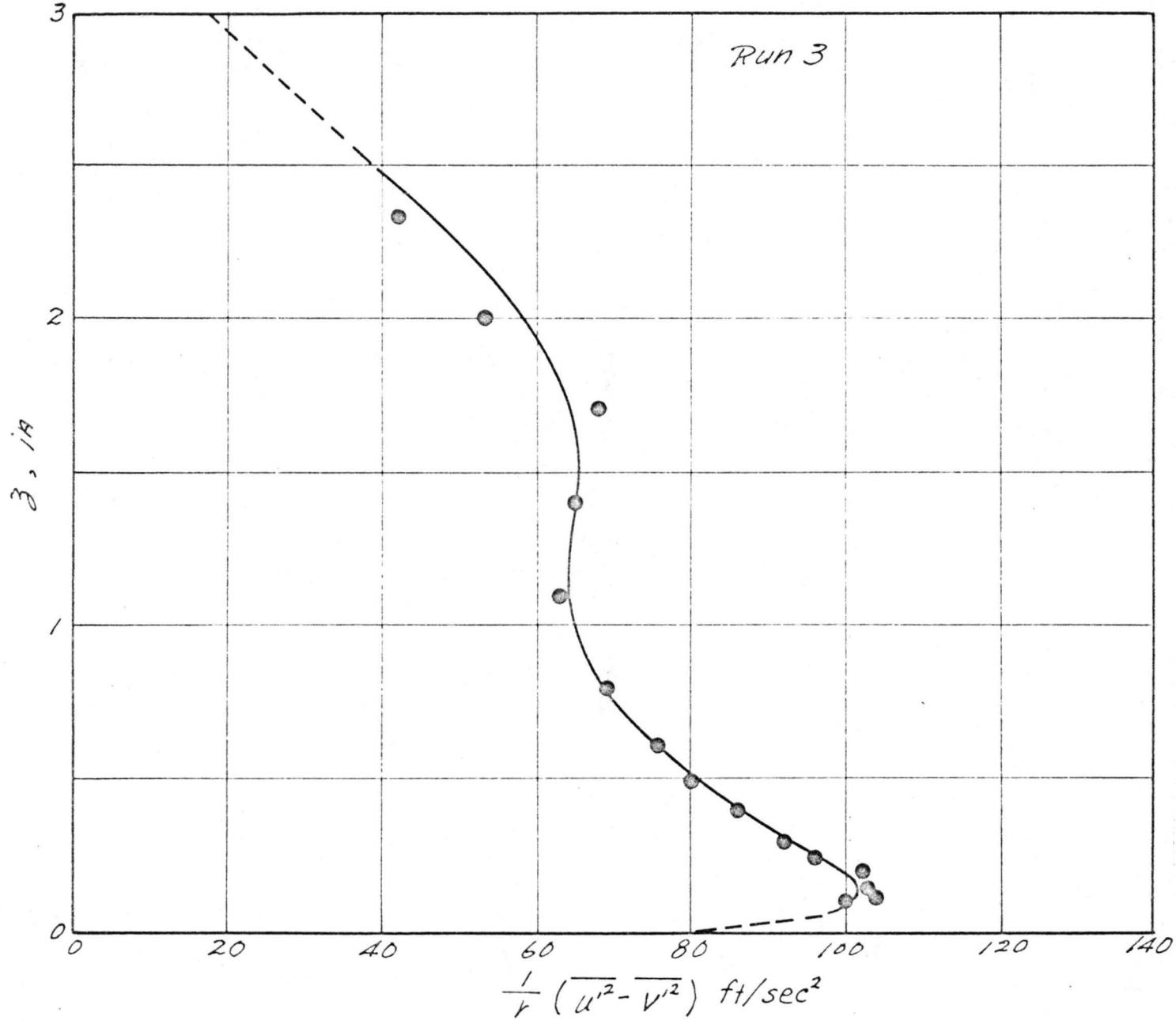

Fig. 7a Distribution of Anisotropic Normal Reynold's Stresses
At Sta. r = 18"

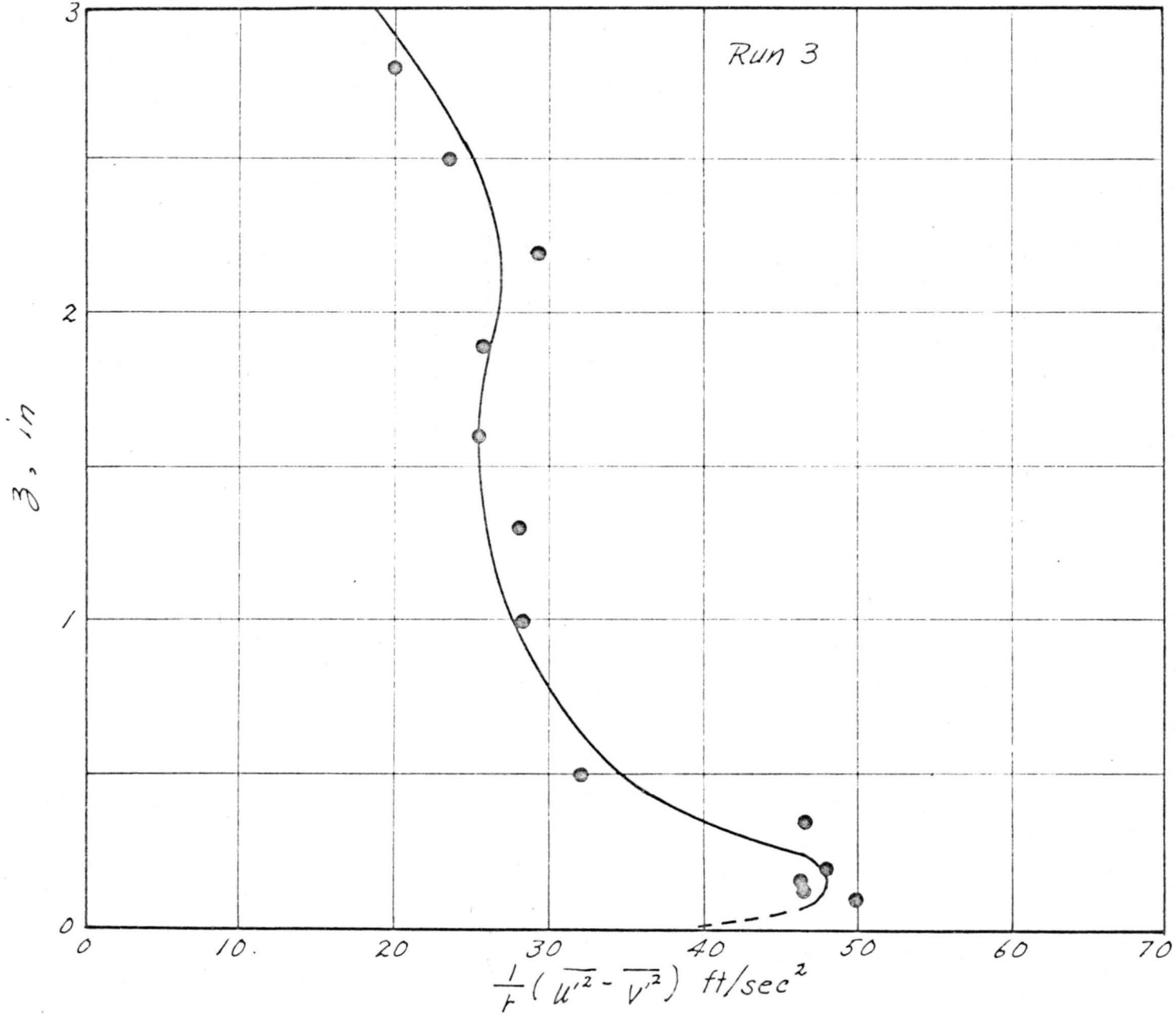

Fig. 76 Distribution of Anisotropic Normal Reynold's Stresses At Sta. r = 24"

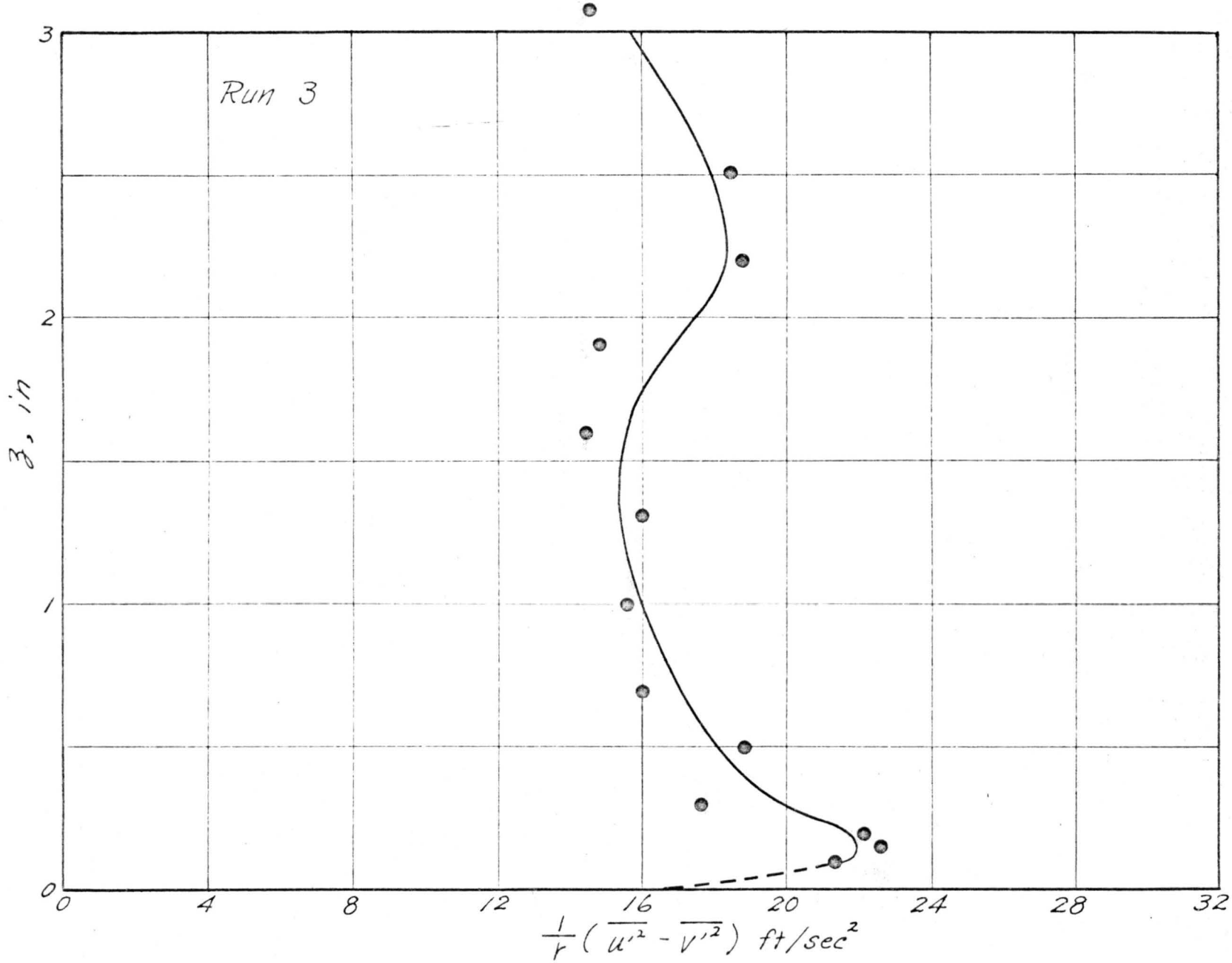

Fig. 7c Distribution of Anisotropic Normal Reynold's Stresses At Sta. r = 30"

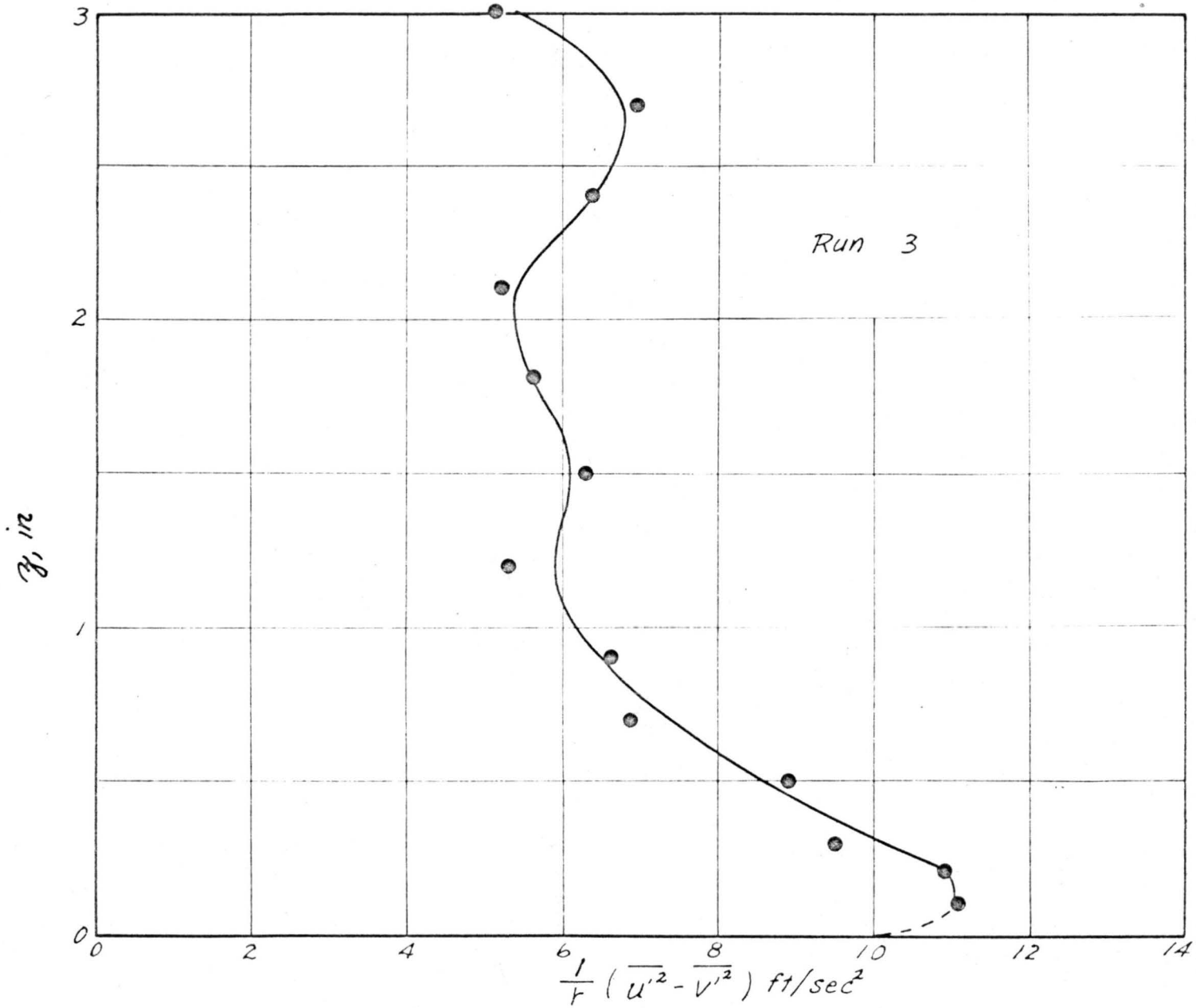

Fig. 7d Distribution of Anisotropic Normal Reynold's Stresses At Sta. r = 36"

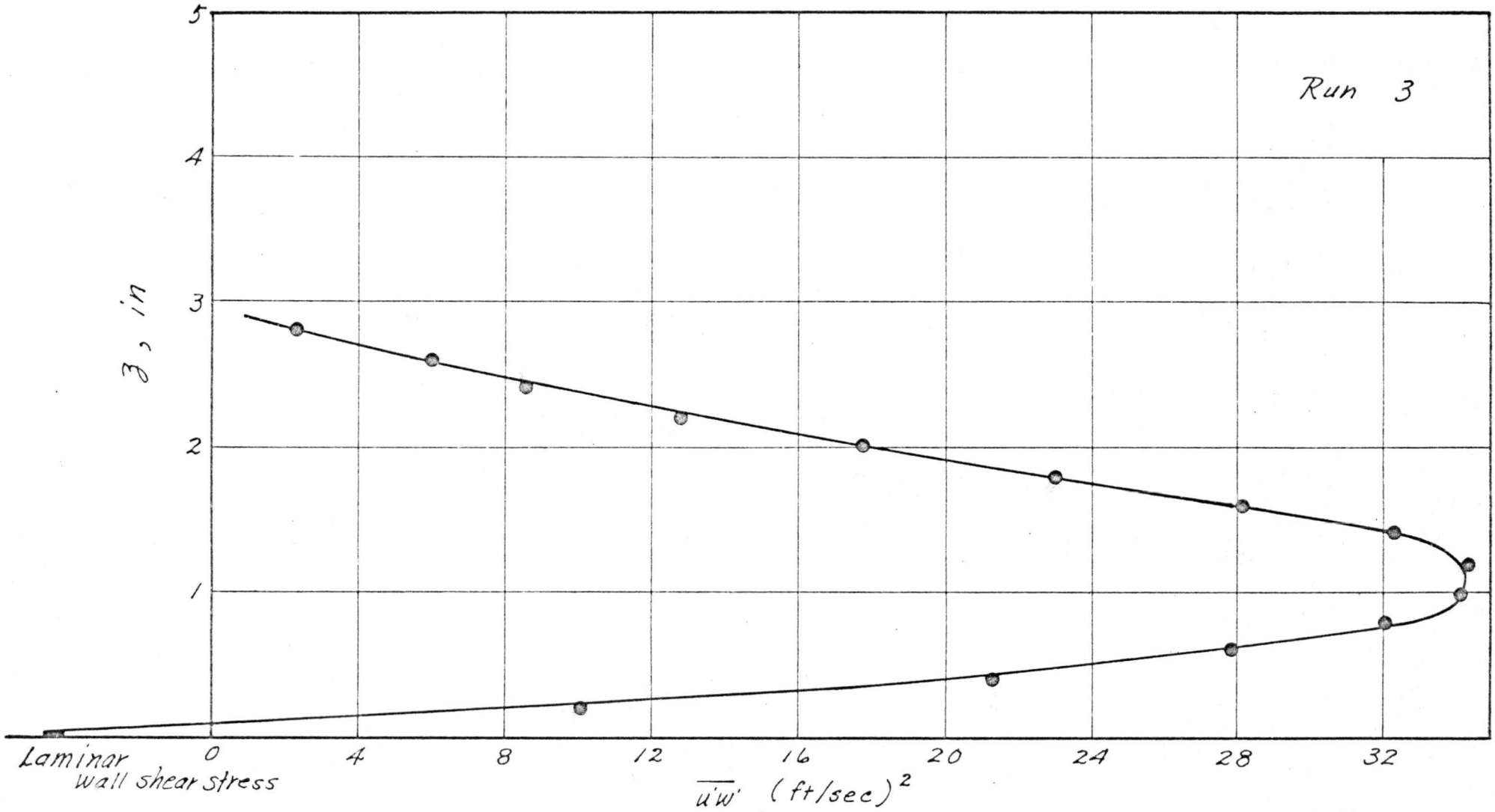

Fig. 8a Distribution of Turbulent Shear Stress At Sta. r = 18"

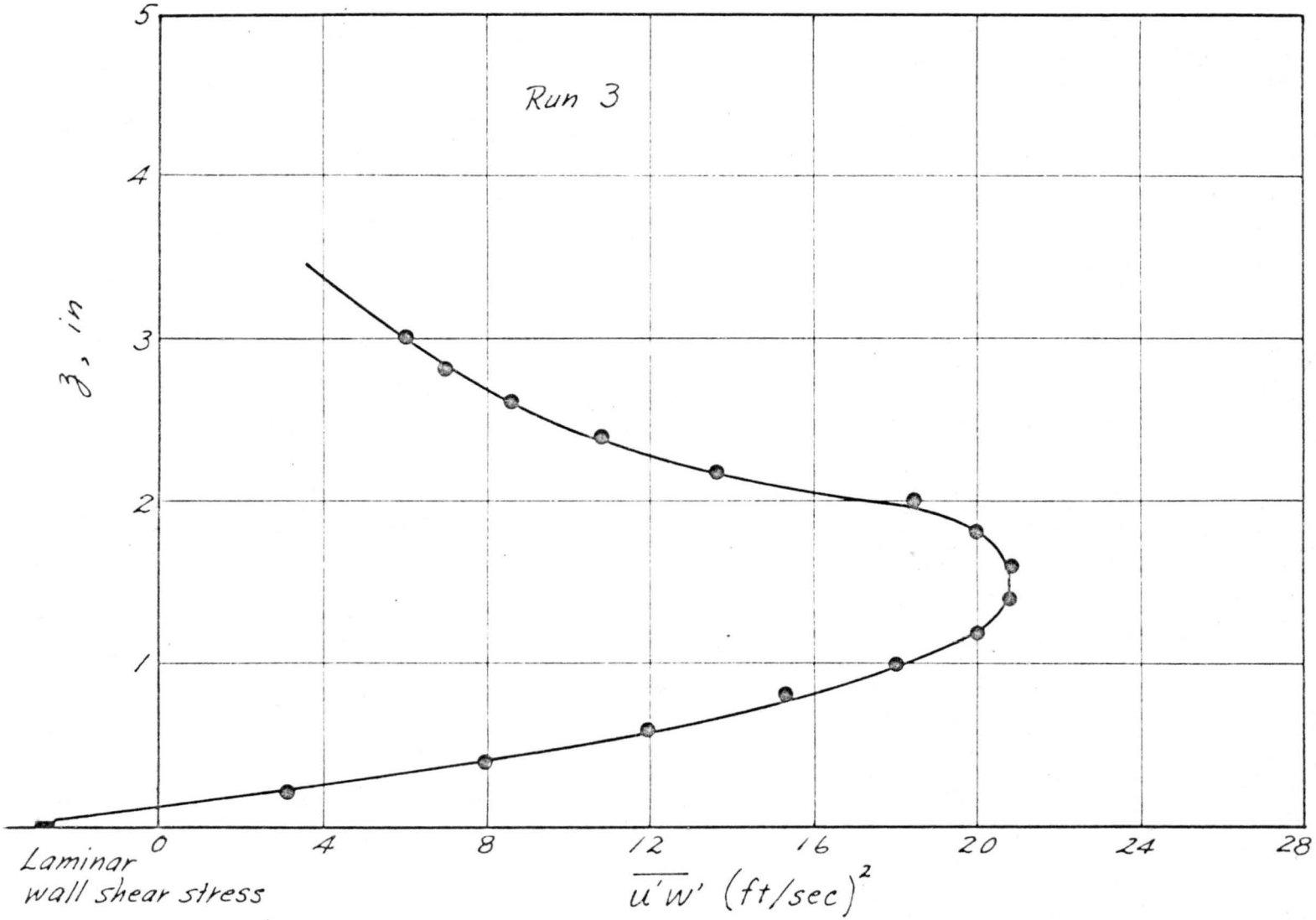

Fig. 8b Distribution of Turbulent Shear Stress At Sta. r = 24"

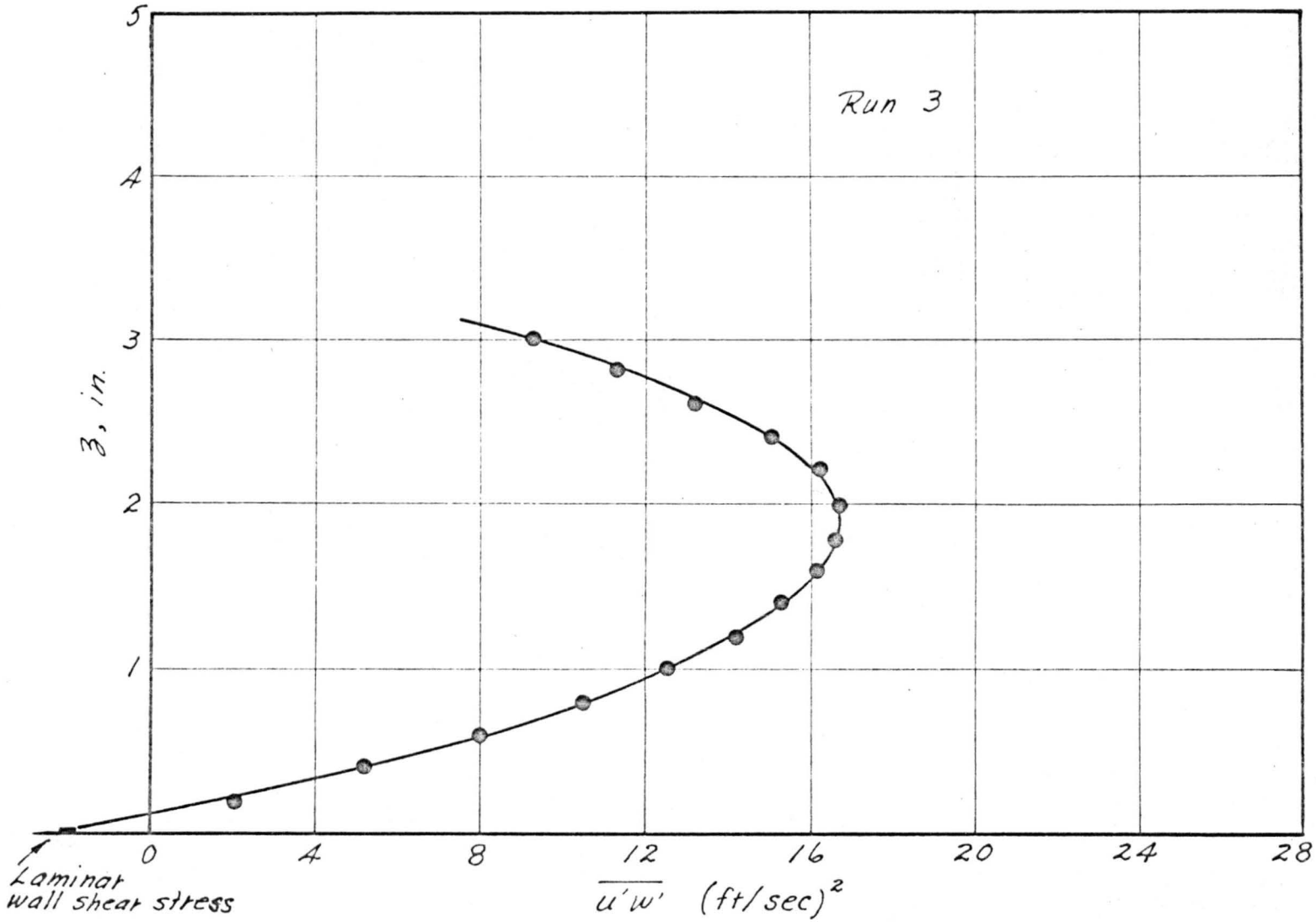

Fig. 8c Distribution of Turbulent Shear Stress At $r = 30''$

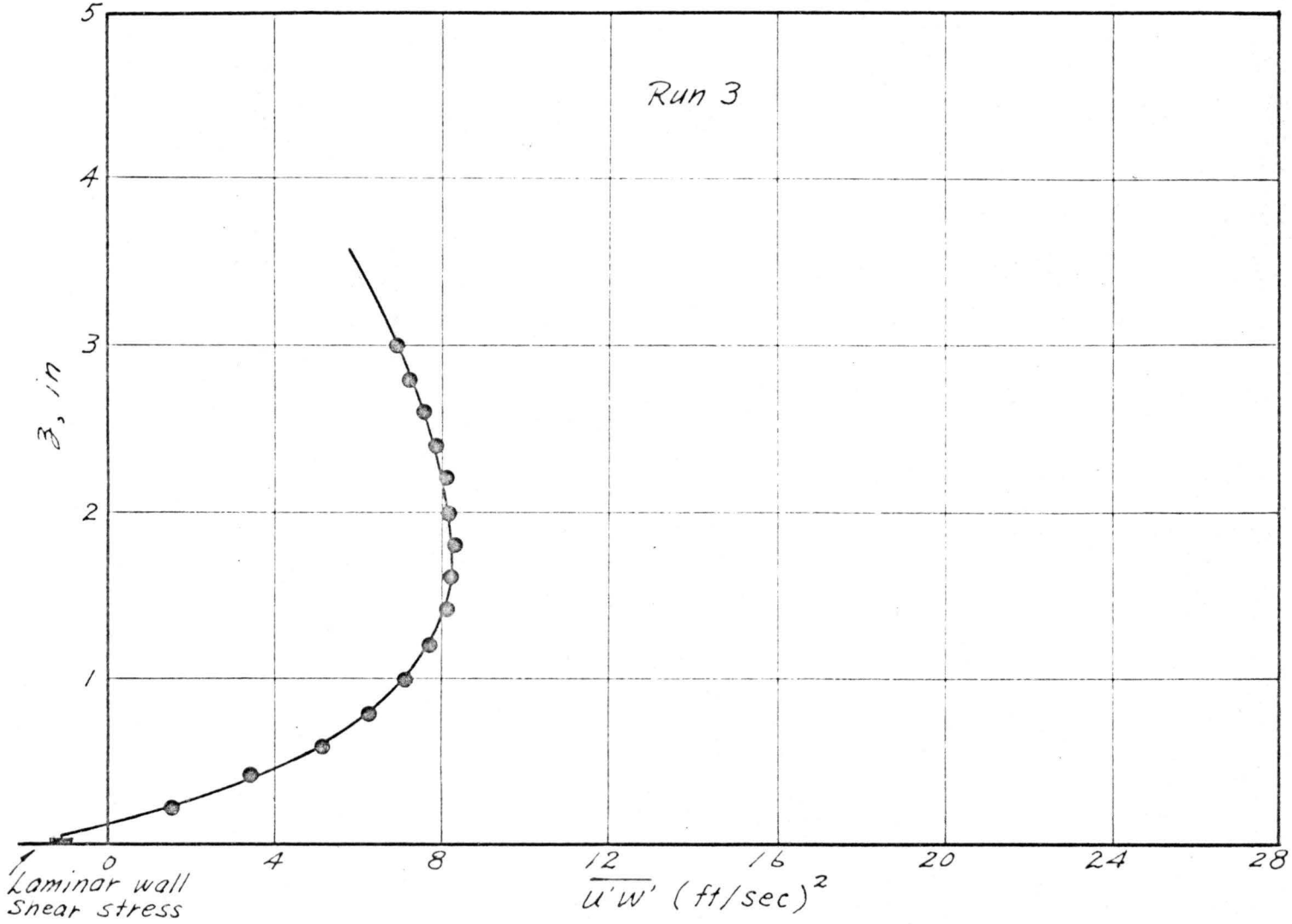

Fig. 8d Distribution of Turbulent Shear Stress At Sta. r = 36"

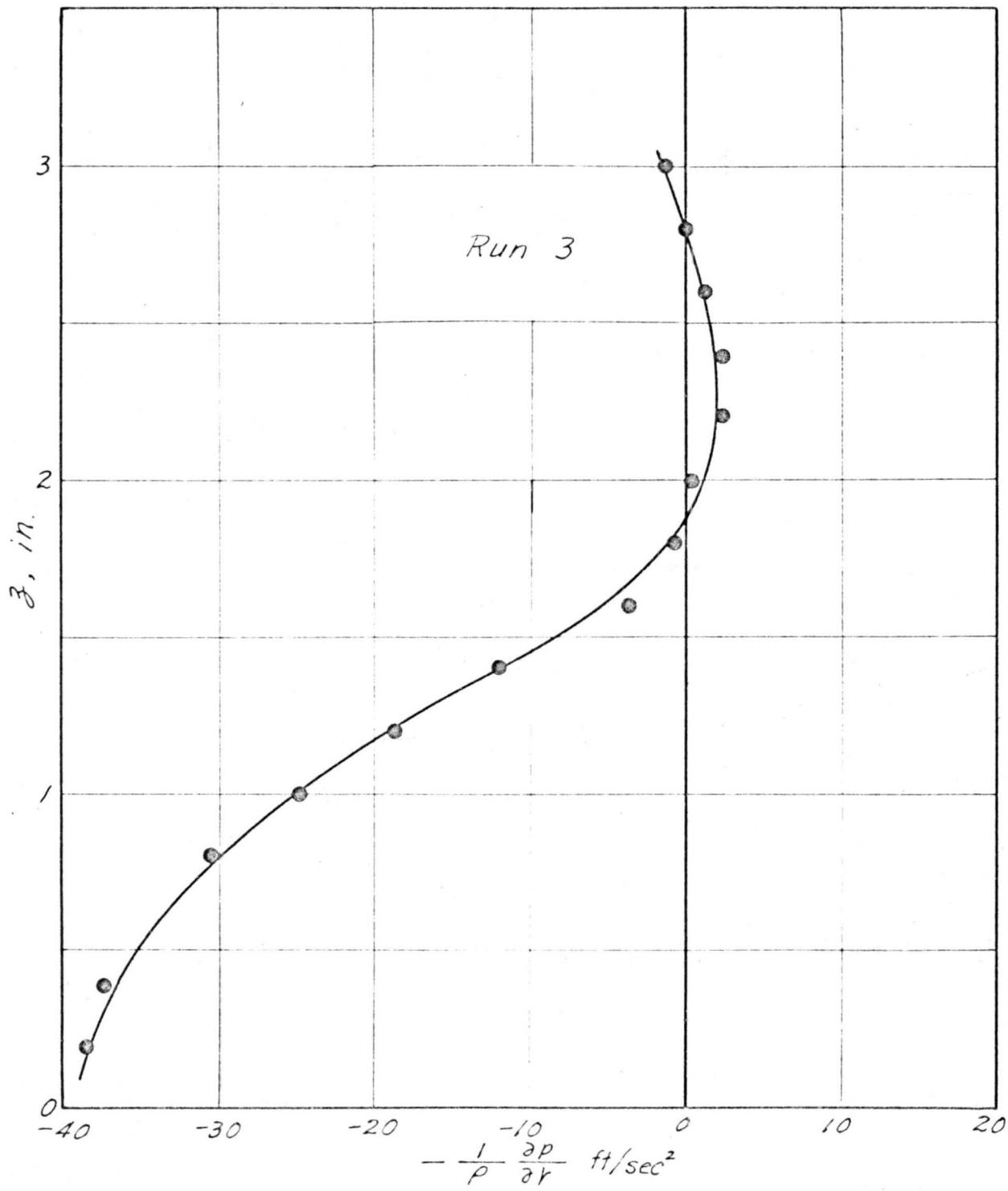

Fig. 9a Distribution of Radial Pressure Gradient
At Station r = 18"

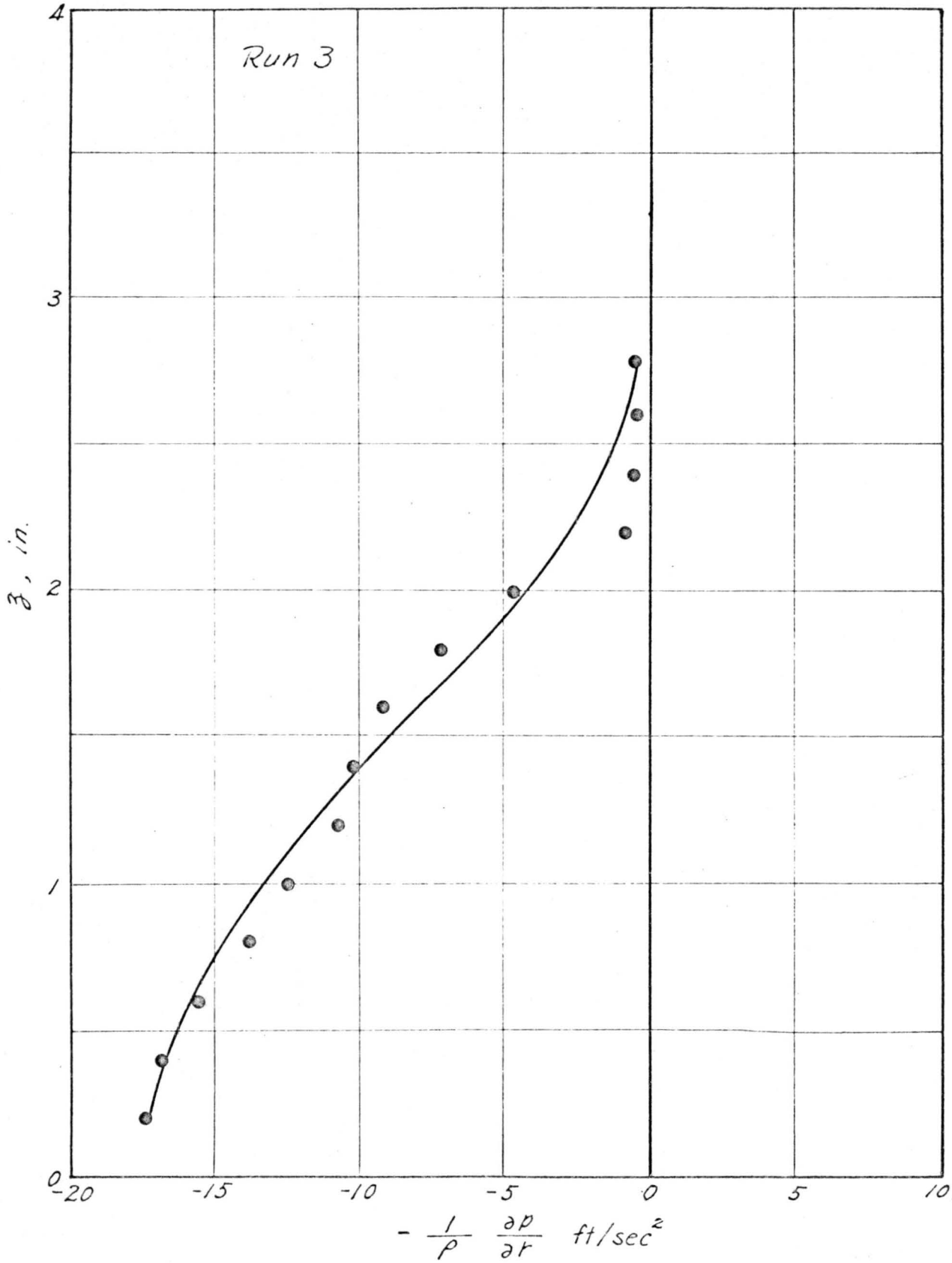

Fig. 9b Distribution of Radial Pressure Gradient At Sta. r=24"

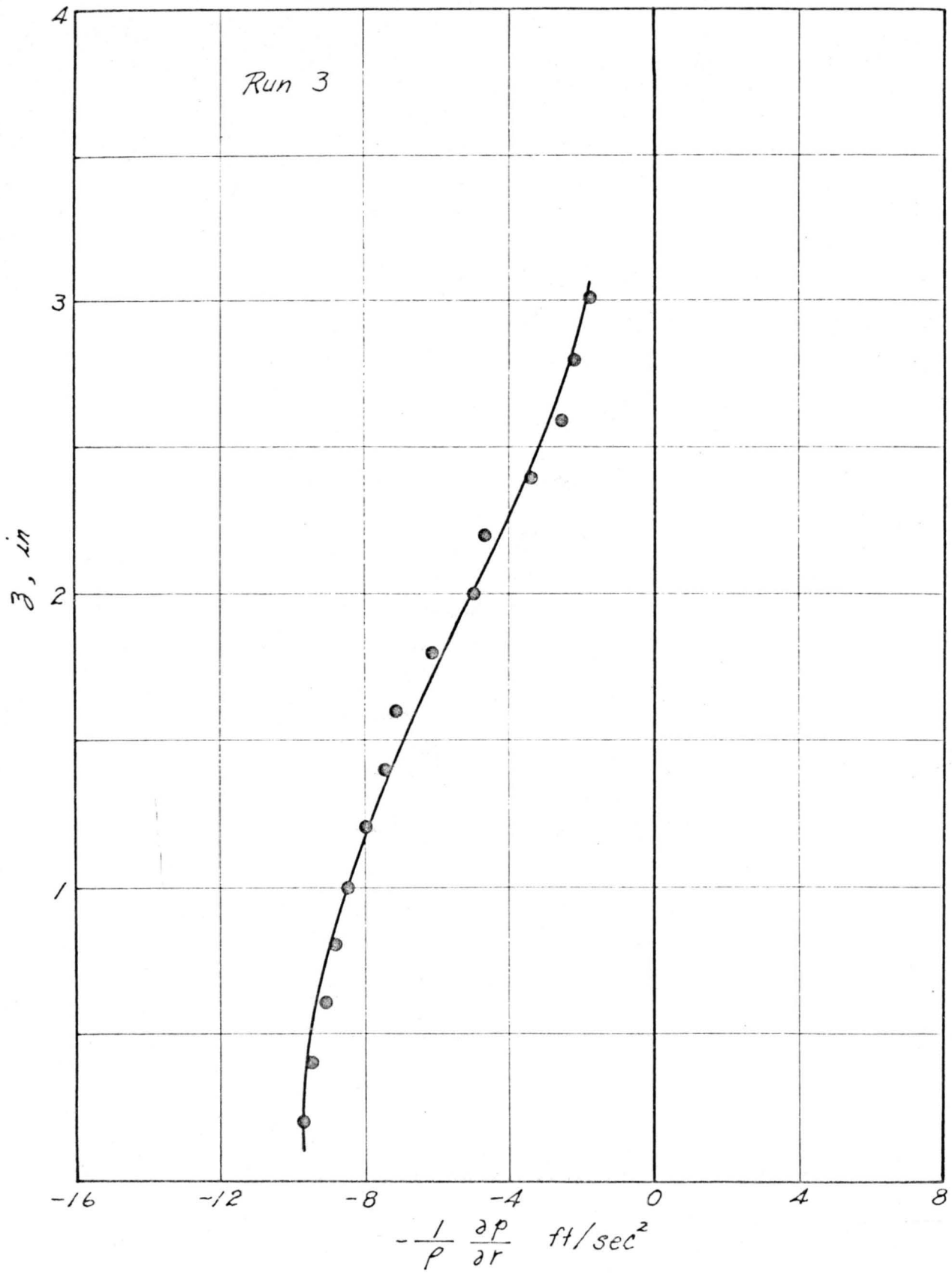

Fig. 9c Distribution of Radial Pressure Gradient At Sta. r=30"

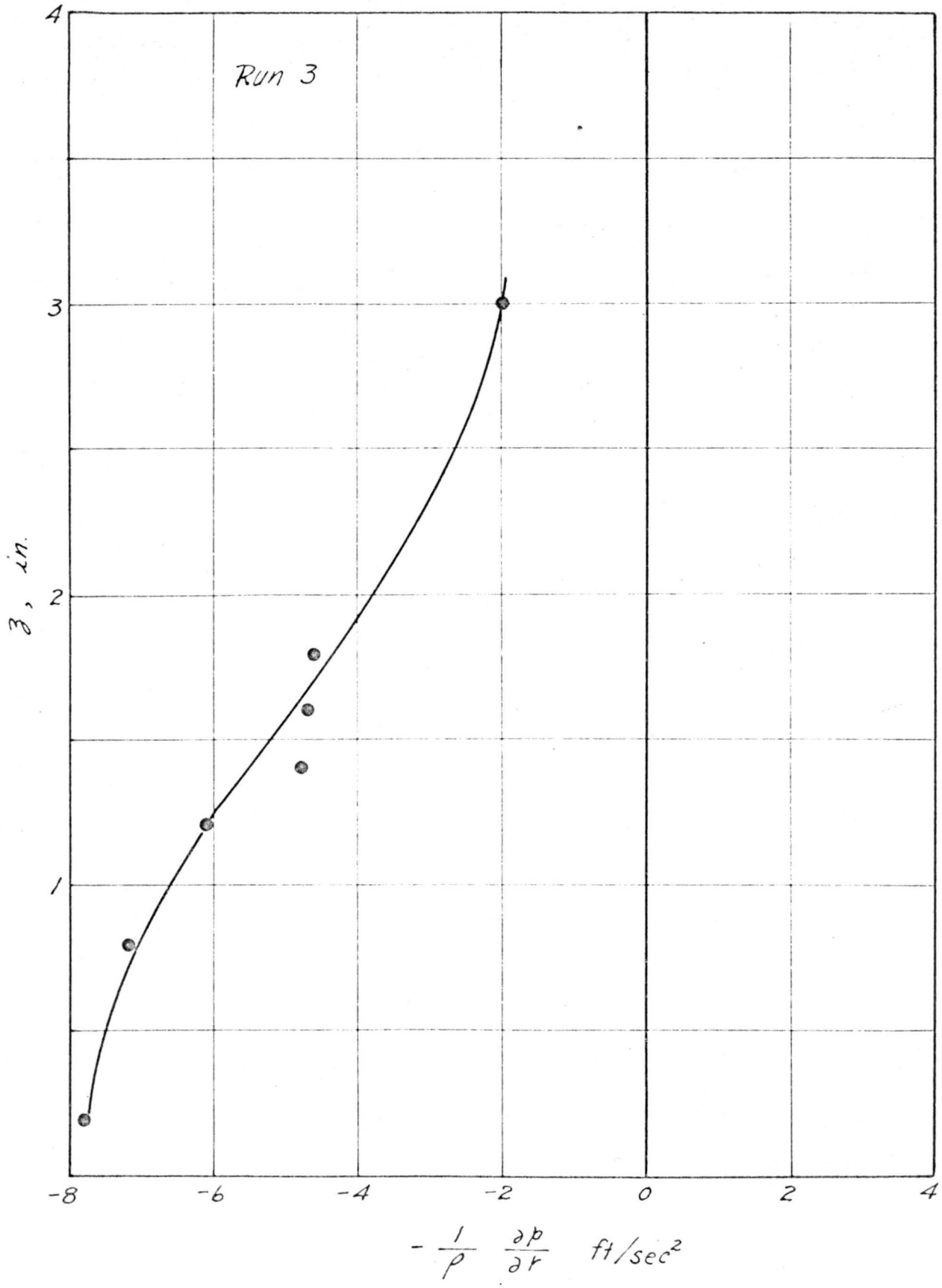

Fig. 9d Distribution of Radial Pressure Gradient At Sta. r=36"

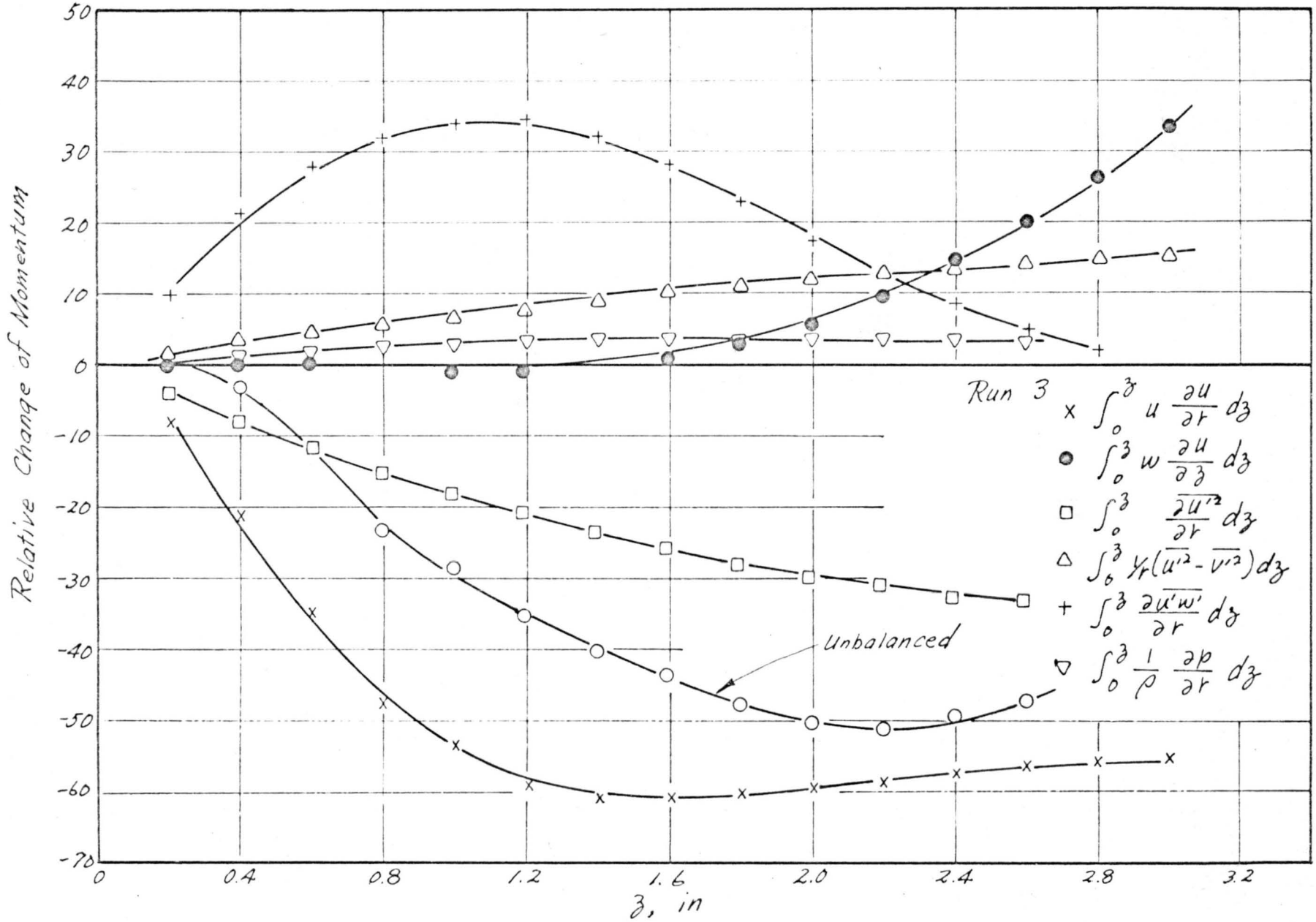

Fig. 10a Momentum Balance in the Vertical Direction At Sta. r = 18"

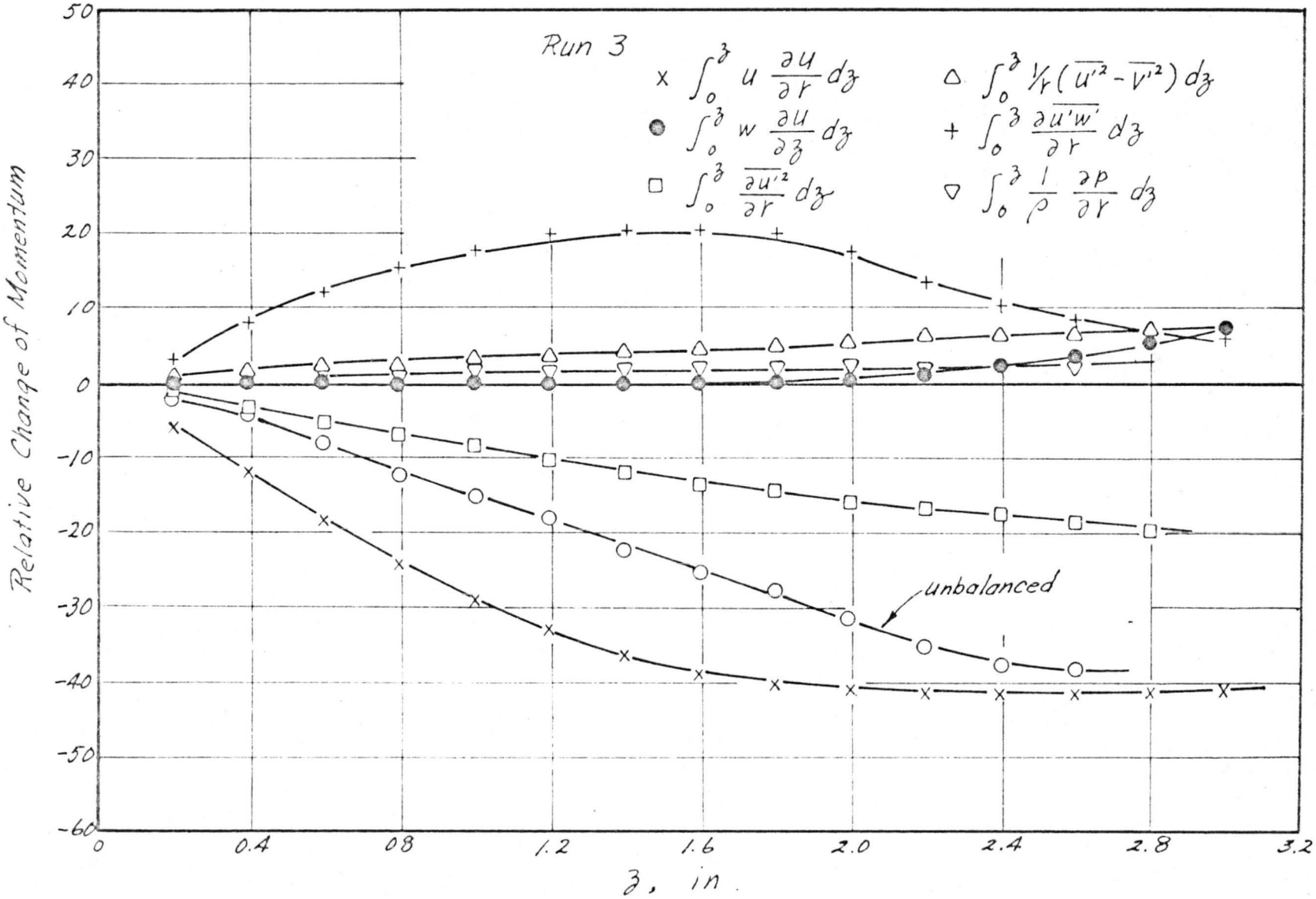

Fig. 10b Momentum Balance in the Vertical Direction At Sta. r = 24"

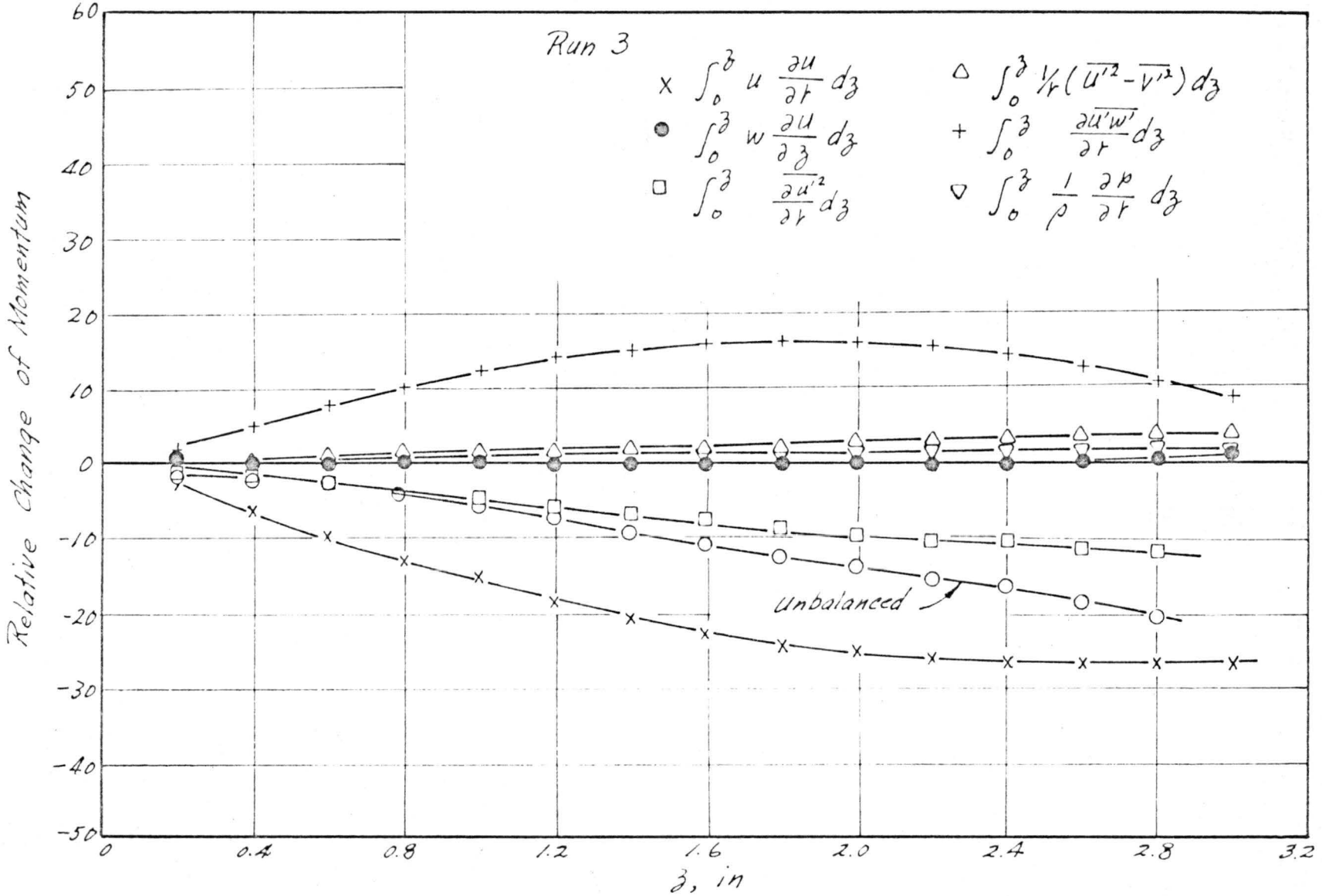

Fig. 10c Momentum Balance in the Vertical Direction At Sta. r = 30"

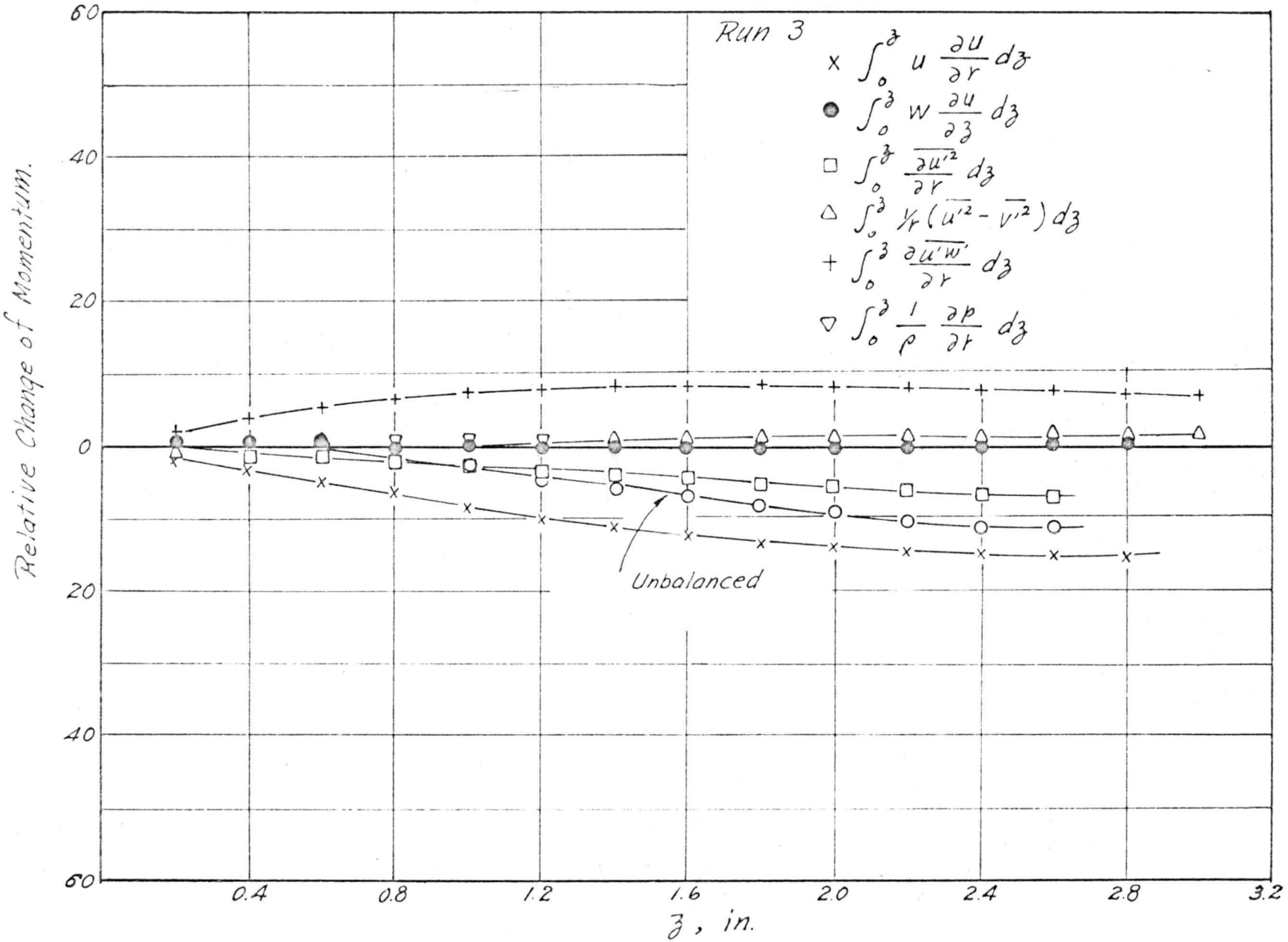

Fig. 10d Momentum Balance in the Vertical Direction At Sta. r=36"

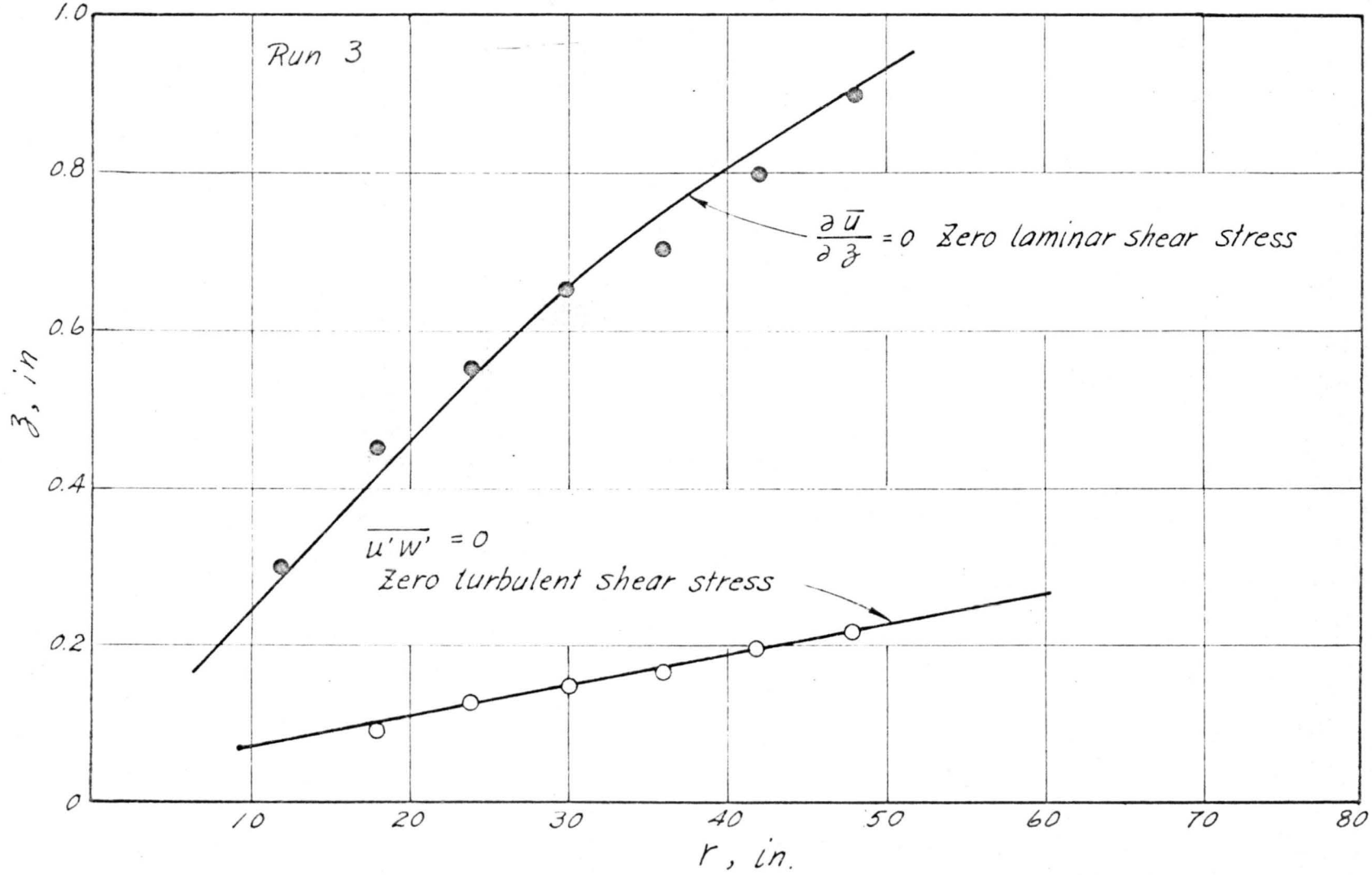

Fig. 11 Location of Zero Shear Stress Planes